51. Sun, C.T. 1998. *Mechanics of Aircraft Structures*. John Wiley & Sons, Inc., New York.
52. Vinson, J.R. 1999. *The Behavior of Sandwich Structures of Isotropic and Composite Materials*. CRC Press, Boca Raton, FL.
53. Steeves, C.A. and Fleck, N.A. 2004. Collapse mechanisms of sandwich beams with composite faces and a foam core, loaded in three-point bending. Part II: Experimental investigation and numerical modeling. *International Journal of Mechanical Sciences*, 46, 585–608.
54. Zenkert, D. 1995. *An Introduction to Sandwich Construction*. Chameleon, London.
55. Steeves, C.A. and Fleck, N.A. 2004. Collapse mechanisms of sandwich beams with composite faces and a foam core, loaded in three-point bending. Part I: analytical models and minimum weight design. *International Journal of Mechanical Sciences*, 46, 561–583.
56. Rehfield, L.W. 1999. A brief history of analysis methodology for grid-stiffened geodesic composite structures. *Proc. 44th International SAMPE Symposium*, CD-ROM.
57. Chen, H.J. and Tsai, S.W. 1996. Analysis and optimum design of composite grid structures. *Journal of Composite Materials*, 30(4), 503–534.
58. Huybrechts, S. and Tsai, S.W. 1996. Analysis and behavior of grid structures. *Composites Science and Technology*, 56(9), 1001–1015.

8

Analysis of Viscoelastic and Dynamic Behavior

8.1 Introduction

In the analyses of chapter 1 to chapter 7, it has been assumed that the applied loads are static in nature and that the composite and its constituents exhibit time-independent linear elastic behavior. However, composite structures are often subjected to dynamic loading caused by vibration or wave propagation. In addition, many composites exhibit time-dependent viscoelastic behavior under load; this is particularly true for composites having polymeric constituents. This chapter contains the basic information needed for the analysis of both viscoelastic and dynamic behavior of composites and their constituents.

The word "viscoelastic" has evolved as a way of describing materials that exhibit characteristics of both viscous fluids and elastic solids. Polymeric materials, which are known to be viscoelastic, may behave like fluids or solids, depending on the time scale or the temperature. For example, polycarbonate, a thermoplastic polymer, is a liquid during molding at processing temperatures, but is a glassy solid at service (ambient) temperatures. It will deform like a rubber at temperatures just above the glass transition temperature, T_g. At temperatures below T_g, however, it will deform just as much, and in the same way if the test time is long enough.

We know that ideal Hookean elastic solids are capable of energy storage under load, but not energy dissipation, whereas ideal Newtonian fluids under nonhydrostatic stresses are capable of energy dissipation, but not energy storage. Viscoelastic materials, however, are capable of both storage and dissipation of energy under load. Another characteristic of viscoelastic materials is memory. Perfectly elastic solids are said to have only "simple memory" because they remember only the unstrained state and the current strains depend only on the current stresses. Viscoelastic materials have what is often referred to as "fading memory" because they remember the past in such a way that the current strains depend more strongly on the recent stress–time history than on the more distant [illegible]

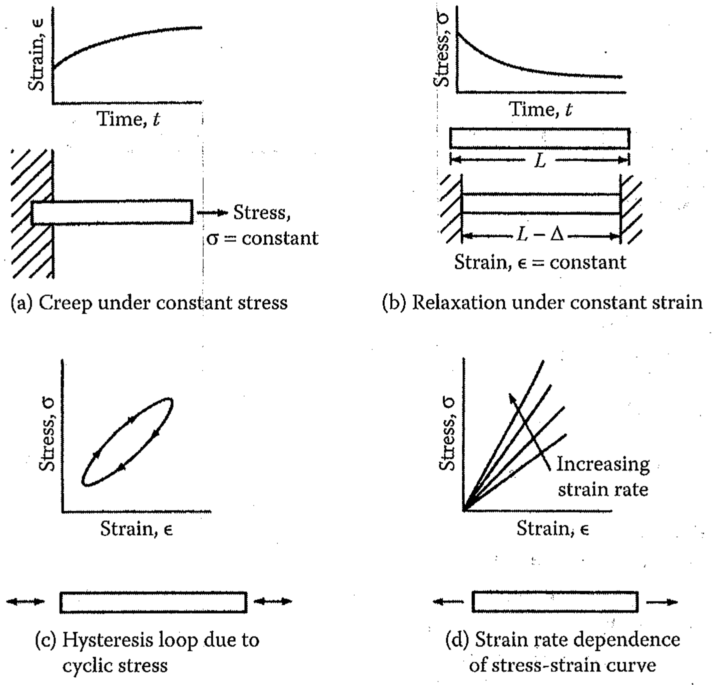

FIGURE 8.1
Physical manifestations of viscoelastic behavior in structural materials, as demonstrated by various types of loading applied to a viscoelastic rod.

There are four important physical manifestations of viscoelastic behavior in structural materials, as illustrated by the various conditions of the uniaxially loaded viscoelastic rod in figure 8.1. First, if the rod is subjected to a constant stress, the resulting strain will exhibit time-dependent "creep," as shown in figure 8.1(a). The time-dependent creep strains are superimposed on the initial elastic strains. Second, if the rod is subjected to a constant strain or displacement, the resulting stress will exhibit time-dependent "relaxation," as shown in figure 8.1(b). That is, the stress relaxes from the initial elastic stress. Third, if the bar is subjected to oscillatory loading, the resulting stress–strain curve will describe a "hysteresis loop," as shown in figure 8.1(c). The area enclosed by the hysteresis loop is a measure of the damping, or dissipation, of energy in the material. Fourth, if the bar is loaded at various strain rates, the stress–strain curves will exhibit a strain–rate dependence, as shown in figure 8.1(d). That is, the stress corresponding to a given strain depends on the rate of straining. An ideal elastic material exhibits none of the above characteristics.

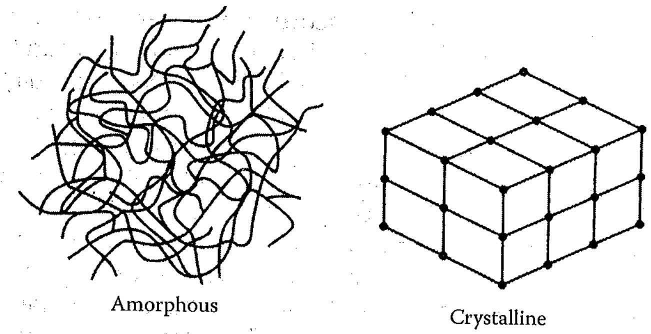

FIGURE 8.2
Amorphous and crystalline microstructures in polymers.

All structural materials exhibit some degree of viscoelasticity, and the extent of such behavior often depends on environmental conditions such as temperature. For example, while a structural steel or aluminum material may be essentially elastic at room temperature, viscoelastic effects become apparent at elevated temperatures approaching half the melting temperature. Polymeric materials are viscoelastic at room temperature, and the viscoelastic effects become stronger as the temperature approaches the glass transition temperature. Recall from chapter 5 that the glass transition region (fig. 5.1) is a region of transition between glassy behavior and rubbery behavior and a region characterized by the onset of pronounced viscoelastic behavior.

Polymers with amorphous microstructures tend to be more viscoelastic than those with crystalline microstructures. As shown in figure 8.2, amorphous microstructures consist of 3-D arrangements of randomly entangled long-chain polymer molecules that are often characterized by analogy to a "bowl of spaghetti." On the other hand, crystalline microstructures consist of regular, ordered crystalline arrays of atoms (fig. 8.2). Some polymers have both amorphous and crystalline components in their microstructures, and some polymers are purely amorphous.

On the basis of the previous discussion, we conclude that viscoelastic behavior of composite materials is more significant for composites having one or more polymeric constituents. Viscoelastic effects in polymer matrix composites are most pronounced in matrix-dominated response to off-axis or shear loading. Viscoelastic deformations and plastic deformations are similar in that both are driven by shear stresses. Indeed, elements of the theory of plasticity are often borrowed for use in the theory of viscoelasticity. For example, it is sometimes assumed in viscoelasticity analysis that the dilatational response to hydrostatic stresses is elastic, but that the distortional response to shear stresses is viscoelastic.

In this chapter we will be concerned with the development of stress–strain relationships for linear viscoelastic materials and their composites. These stress–strain relationships take on special forms for creep, relaxation, and sinusoidal oscillation. Following the use of certain integral transforms, the viscoelastic stress–strain relationships turn out to be analogous to Hookean elastic stress–strain relationships, leading to the so-called Elastic–Viscoelastic Correspondence Principle.

Dynamic loading is usually categorized as being either impulsive or oscillatory. Dynamic response consists of either a propagating wave or a vibration, depending on the elapsed time and the relative magnitudes of the wavelength of the response and the characteristic structural dimension. Both types of excitation usually cause wave propagation initially. Wave propagation will continue if the response wavelength is much shorter than the characteristic structural dimension, otherwise standing waves (i.e., vibrations) will be set up as the waves begin to reflect back from the boundaries. Wave propagation in composites may involve complex reflection and/or refraction effects at fiber/matrix interfaces or ply interfaces, complicating matters further.

The dynamic response of composites may also be complicated by their anisotropic behavior. For example, the speed of a propagating wave in an isotropic material is independent of orientation, whereas the wave speed in an anisotropic composite depends on the direction of propagation. Anisotropic coupling effects often lead to complex waves or modes of vibration. For example, an isotropic beam subjected to an oscillatory bending moment will respond in pure flexural modes of vibration, but a nonsymmetric laminate may respond in a coupled bending–twisting mode or some other complex mode. In this chapter, however, only the analyses for vibrations and wave propagation in specially orthotropic composites or laminates without coupling will be considered.

Damping, which is one of the manifestations of viscoelastic behavior, is obviously important for noise and vibration control. Composites generally have better damping than conventional metallic structural materials, especially if the composite has one or more polymeric constituents. It will be shown that the complex modulus notation and the Elastic–Viscoelastic Correspondence Principle from viscoelasticity theory are particularly useful in the development of analytical models for predicting the damping behavior of composites.

Finally, it will be shown that the effective modulus theory, which was introduced in chapter 2 and chapter 3, is indispensable in both viscoelastic and dynamic analyses of composites. Under certain restrictions, the concept of an effective modulus or effective compliance will be used to extend various viscoelastic analyses and dynamic analyses of homogeneous materials to the corresponding analyses of heterogeneous composites.

8.2 Linear Viscoelastic Behavior of Composites

A linear elastic solid exhibits a linearity between stress and strain, and this linear relationship is independent of time. A linear viscoelastic solid also exhibits a linearity between stress and strain, but the linear relationship depends on the time history of the input. The mathematical criteria for linear viscoelastic behavior are similar to those for linear behavior of any system. Following the notation of Schapery [1], the criteria can be stated as follows:

Let the response R to an input I be written as $R = R\{I\}$, where $R\{I\}$ denotes that the current value of R is a function of the time history of the input I. For linear viscoelastic behavior, the response $R\{I\}$ must satisfy both the following conditions:

1. *Proportionality*: i.e., $R\{cI\} = cR\{I\}$, where c is a constant
2. *Superposition*: i.e., $R\{I_a + I_b\} = R\{I_a\} + R\{I_b\}$, where I_a and I_b may be the same or different time histories

Any response not satisfying these criteria would be a nonlinear response. These criteria form the basis of the stress–strain relationship known as the Boltzmann superposition integral, which is developed in the next section.

Before getting into the analytical modeling of linear viscoelastic behavior, however, it is instructive to briefly discuss a phenomenological approach to verification of linear viscoelastic behavior. Probably the most widely used method of characterizing viscoelastic behavior is the tensile creep test described in figure 8.1(a), which involves the application of a constant tensile stress to a specimen and measurement of the resulting time-dependent strain. The strain versus time curves are known as creep curves. If a number of creep curves are generated at different stress levels as shown schematically in figure 8.3(a), these creep curves can be used to plot stress–strain curves at different times. For example, by taking the ratio of stress to strain at each stress level corresponding to time t_1 in figure 8.3(a), we can plot the so-called isochronous stress–strain curve at time $t = t_1$, as shown in figure 8.3(b). The slope of the isochronous stress–strain curve is the time-dependent Young's modulus, $E(t)$, and typically $E(t)$ decreases with time. The creep compliance for a constant stress σ is

$$S(t) = \frac{\varepsilon(t)}{\sigma} \cong \frac{1}{E(t)} \quad (8.1)$$

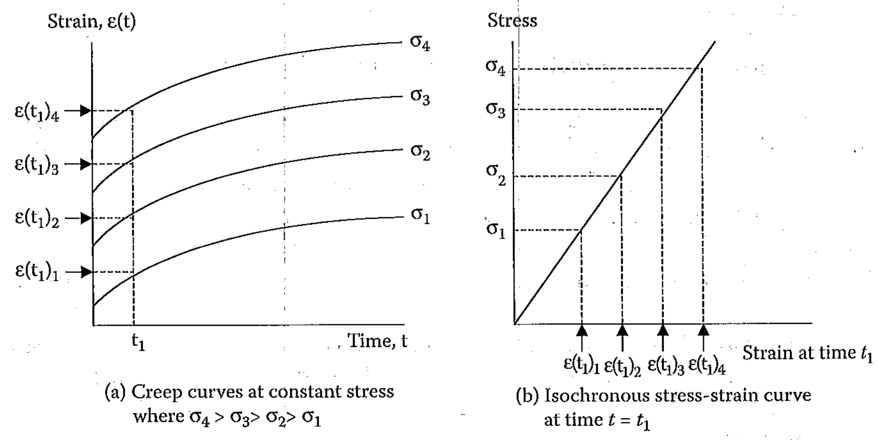

FIGURE 8.3
Illustration of creep curves at constant stress and corresponding isochronous stress-strain curves.

and obviously $S(t)$ increases with time. Phenomenologically speaking, a material is linear viscoelastic within the range of stresses and times for which its isochronous stress–strain curves are linear. There are always limits on the ranges of stress and time within which a material will continue to behave in a linear viscoelastic manner. For example, if the stress level becomes high enough, the isochronous stress–strain curve will become nonlinear, and this means that the material becomes nonlinear viscoelastic. In this book, it is always assumed that the viscoelastic materials being discussed are linear viscoelastic.

Typically, the creep compliance for linear viscoelastic creep curves such as those shown in figure 8.3(a) can be described mathematically using a power law expression of the form

$$S(t) = S_O + S_1 t^n \tag{8.2}$$

where S_O is the initial elastic compliance and S_1 and n are empirically determined parameters. It has been shown experimentally by Beckwith [2] that, for polymer matrix composites, the creep exponent n depends only on the polymer matrix, and indeed that n is the same for the composite and the polymer matrix material. Since creep experiments are generally conducted over several decades, it is often convenient to use log–log scales to plot creep compliance data. A power law plotted on a log–log scale becomes a straight line, and this provides another way to check for linear viscoelastic behavior. For example, moving S_O to the left-hand side

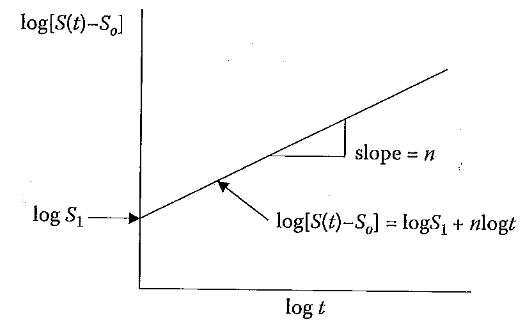

FIGURE 8.4
Illustration of log creep compliance vs log time plot.

of equation (8.2) and taking the log of both sides of the resulting equation yields

$$\log[S(t) - S_O] = \log S_1 + n \log t \tag{8.3}$$

which is the equation for a straight line on a log–log plot of $\log[S(t) - S_O]$ versus $\log t$ with slope n and vertical axis intercept $\log S_1$, as shown in figure 8.4.

8.2.1 Boltzmann Superposition Integrals for Creep and Relaxation

The stress–strain relationships for a linear viscoelastic maternal can be developed by using the Boltzmann Superposition Principle [3]. If the material is at a constant temperature and is "nonaging," then the response at any time t due to an input at time $t = \tau$ is a function of the input and the elapsed time $(t - \tau)$ only. Aging is a time-dependent change in the material, which is different from viscoelastic creep or relaxation. Both temperature and aging effects will be considered in section 8.2.6.

Consider the 1-D isothermal loading of a nonaging, isotropic, homogeneous linear viscoelastic material by the stresses $\Delta\sigma_1$, $\Delta\sigma_2$, and $\Delta\sigma_3$ at times τ_1, τ_2, and τ_3, respectively, as shown in figure 8.5. According to the Boltzmann Superposition Principle, the strain response is linearly proportional to the input stress, but the proportionality factor is a function of the elapsed time since the application of the input stress. Thus, for the stress–time history in figure 8.5, the total strain response at any time $t > \tau_3$ is given by

$$\varepsilon(t) = \Delta\sigma_1 S(t - \tau_1) + \Delta\sigma_2 S(t - \tau_2) + \Delta\sigma_3 S(t - \tau_3) \tag{8.4}$$

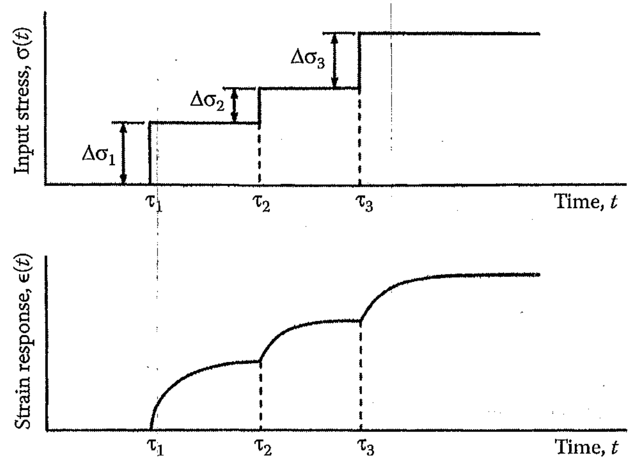

FIGURE 8.5
Input stress and strain response in 1-D loading of a linear viscoelastic material for illustration of the Boltzmann Superposition Principle.

where $S(t)$ is the creep compliance, which is zero for $t < 0$. For input stresses having arbitrary time histories, equation (8.4) can be generalized as the Boltzmann superposition integral, or hereditary law:

$$\varepsilon(t) = \int_{-\infty}^{t} S(t-\tau)\frac{d\sigma(\tau)}{d\tau}d\tau \tag{8.5}$$

Alternatively, the stress resulting from arbitrary strain inputs may be given by

$$\sigma(t) = \int_{-\infty}^{t} C(t-\tau)\frac{d\varepsilon(\tau)}{d\tau}d\tau \tag{8.6}$$

where $C(t)$ is the relaxation modulus, which is zero for $t < 0$.

Equation (8.5) can be extended to the more general case of a homogeneous, anisotropic, linear viscoelastic material with multiaxial inputs and responses by using the contracted notation and writing

$$\varepsilon_i(t) = \int_{-\infty}^{t} S_{ij}(t-\tau)\frac{d\sigma_j(\tau)}{d\tau}d\tau \tag{8.7}$$

where
$i, j = 1, 2, \ldots, 6$
$S_{ij}(t)$ = creep compliances

For the specific case of the homogeneous, linear viscoelastic, specially orthotropic lamina in plane stress, equations (8.7) become

$$\begin{aligned}
\varepsilon_1(t) &= \int_{-\infty}^{t} S_{11}(t-\tau)\frac{d\sigma_1(\tau)}{d\tau}d\tau + \int_{-\infty}^{t} S_{12}(t-\tau)\frac{d\sigma_2(\tau)}{d\tau}d\tau \\
\varepsilon_2(t) &= \int_{-\infty}^{t} S_{12}(t-\tau)\frac{d\sigma_1(\tau)}{d\tau}d\tau + \int_{-\infty}^{t} S_{22}(t-\tau)\frac{d\sigma_2(\tau)}{d\tau}d\tau \\
\gamma_{12}(t) &= \int_{-\infty}^{t} S_{66}(t-\tau)\frac{d\tau_{12}(\tau)}{d\tau}d\tau
\end{aligned} \tag{8.8}$$

Similarly, equation (8.6) can be generalized to the form,

$$\sigma_1(t) = \int_{-\infty}^{t} C_{ij}(t-\tau)\frac{d\varepsilon_j(\tau)}{d\tau}d\tau \tag{8.9}$$

where the $C_{ij}(t)$ are the relaxation moduli. Note that equation (8.7) and equation (8.9) are analogous to the generalized Hooke's law for linear elastic materials given by equation (2.5) and equation (2.3), respectively, and that equations (8.8) are analogous to the Hooke's law for the specially orthotropic lamina given by equations (2.24). Thus, the creep compliances, $S_{ij}(t)$, for the viscoelastic material are analogous to the elastic compliances, S_{ij}, and the viscoelastic relaxation moduli, $C_{ij}(t)$, are analogous to the elastic stiffnesses, C_{ij}.

In order to apply the stress–strain relationships in equation (8.7) to equation (8.9) to *heterogeneous*, anisotropic, linear viscoelastic composites, we again make use of the "effective modulus theory" that was introduced in chapter 2 and chapter 3. Recall that in order to apply the stress–strain relationships at a point in a homogeneous material (i.e., equation [2.3] and equation [2.5]) to the case of a heterogeneous composite, we replaced the stresses and strains at a point with the volume-averaged stresses and strains (eq. [2.7] and eq. [2.8]) and also replaced the elastic moduli of the heterogeneous composite by effective moduli of an equivalent homogeneous material (eq. [2.9] and eq. [2.10]). Recall also that the criterion for the use of the effective modulus theory was that the scale of the inhomogeneity, d, had to be much smaller than the characteristic structural dimension, L, over which the averaging is done. However, since this chapter also deals with dynamic behavior, it is appropriate to add

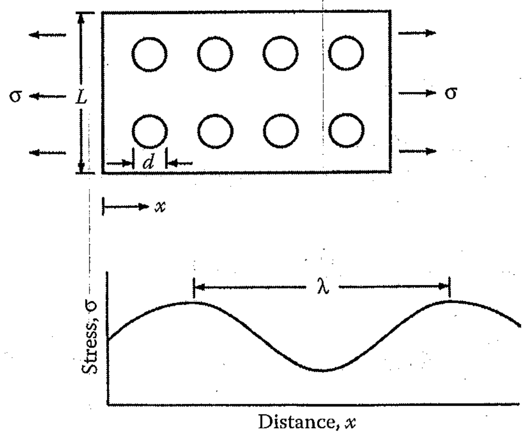

FIGURE 8.6
Critical dimensions which are used in the criteria for the application of the effective modulus theory.

another criterion related to dynamic effects. That is, the scale of the inhomogeneity, d, must also be much smaller than the characteristic wavelength, λ, of the dynamic stress distribution (fig. 8.6). Thus, the criteria for the use of the effective modulus theory in dynamic loading of viscoelastic composites are $d \ll L$ and $d \ll \lambda$. Practically speaking, the second criterion becomes important only when dealing with the propagation of high-frequency waves having very short wavelengths. On the other hand, the wavelengths associated with typical mechanical vibrations will almost always be sufficiently large so as to satisfy $d \ll \lambda$. The book by Christensen [4] gives a more detailed discussion of the effective modulus theory.

Thus, equation (8.7) to equation (8.9) are valid for heterogeneous, anisotropic, linear viscoelastic composites if at an arbitrary time, t, we simply replace the stresses and strains at a point with the volume-averaged stresses and strains, replace the creep compliances with the effective creep compliances, and replace the relaxation moduli with the effective relaxation moduli. Thus, the effective creep compliance matrix for the specially orthotropic lamina in plane stress is given by

$$S_{ij}(t) = \begin{bmatrix} S_{11}(t) & S_{12}(t) & 0 \\ S_{21}(t) & S_{22}(t) & 0 \\ 0 & 0 & S_{66}(t) \end{bmatrix} \tag{8.10}$$

Note the close resemblance of this creep compliance matrix to the corresponding elastic compliance matrix in Equations (2.24). For the generally orthotropic lamina, we have

$$\bar{S}_{ij}(t) = \begin{bmatrix} \bar{S}_{11}(t) & \bar{S}_{12}(t) & \bar{S}_{16}(t) \\ \bar{S}_{21}(t) & \bar{S}_{22}(t) & \bar{S}_{26}(t) \\ \bar{S}_{16}(t) & \bar{S}_{26}(t) & \bar{S}_{66}(t) \end{bmatrix} \tag{8.11}$$

where the $\bar{S}_{ij}(t)$ are the transformed effective creep compliances. Note the close resemblance of this matrix to the corresponding transformed elastic compliance matrix in Equations (2.37). Halpin and Pagano [5] have shown that the $\bar{S}_{ij}(t)$ are related to the $S_{ij}(t)$ by the transformations,

$$\begin{aligned}
\bar{S}_{11}(t) &= S_{11}(t)c^4 + [2S_{12}(t) + S_{66}(t)]c^2s^2 + S_{22}(t)s^4 \\
\bar{S}_{12}(t) &= S_{12}(t)(s^4 + c^4) + [S_{11}(t) - S_{22}(t) - S_{66}(t)]s^2c^2 \\
\bar{S}_{22}(t) &= S_{11}(t)s^4 + [2S_{12}(t) + S_{66}(t)]s^2c^2 + S_{22}(t)c^4 \\
\bar{S}_{66}(t) &= 2[2S_{11}(t) + 2S_{22}(t) - 4S_{12}(t) - S_{66}(t)]c^2s^2 + S_{66}(t)(s^4 + c^4) \\
\bar{S}_{16}(t) &= [2S_{11}(t) - 2S_{12}(t) - S_{66}(t)]sc^3 - [2S_{22}(t) - 2S_{12}(t) - S_{66}(t)]s^3c \\
\bar{S}_{26}(t) &= [2S_{11}(t) - 2S_{12}(t) - S_{66}(t)]s^3c - [2S_{22}(t) - 2S_{12}(t) - S_{66}(t)]sc^3
\end{aligned} \tag{8.12}$$

where $s = \sin\theta$, $c = \cos\theta$, and the angle θ has been defined in figure 2.8. Note that these equations are entirely analogous to the corresponding elastic compliance transformation equations. Further justification for such direct correspondence between elastic and viscoelastic equations is provided by the Elastic–Viscoelastic Correspondence Principle, which is discussed later.

Recall that for the elastic case, strain energy considerations led to the symmetry conditions $S_{ij} = S_{ji}$ and $C_{ij} = C_{ji}$. For the viscoelastic case, Schapery [1] has used thermodynamic arguments to show that if $S_{ij}(t) = S_{ji}(t)$ for the constituent materials, then the same is true for the composite. Halpin and Pagano [5] and others have presented experimental evidence that for transversely isotropic composites under plane stress, $S_{12}(t) = S_{21}(t)$. In both elastic and viscoelastic cases, further reductions in the number of independent moduli or compliances depend on material property symmetry and the coordinate system used.

EXAMPLE 8.1

A specially orthotropic, linear viscoelastic composite lamina is subjected to the shear stress–time history shown in figure 8.7. If the effective shear creep compliance is given by

$$S_{66}(t) = A + Bt, \quad t \geq 0; \qquad S_{66}(t) = 0, \quad t < 0$$

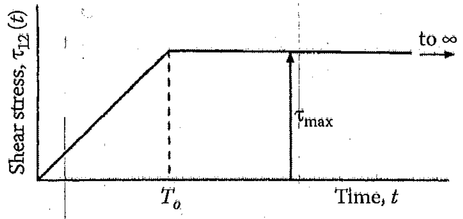

FIGURE 8.7
Shear stress time history for example 8.1.

where A and B are material constants and t is time. Find the expressions for the creep strain at $t < T_0$ and $t > T_0$.

Solution. The creep strain is given by equation (8.7):

$$\varepsilon_i(t) = \int_{-\infty}^{t} S_{ij}(t-\tau)\frac{d\sigma_j(\tau)}{d\tau}d\tau$$

which, for the case of $t < T_0$, reduces to

$$\varepsilon_6(t) = \gamma_{12}(t) = \int_0^t [A + B(t-\tau)]\frac{\tau_{max}}{T_0}d\tau = \frac{A\tau_{max}}{T_0}t + \frac{B\tau_{max}}{2T_0}t^2$$

For $t > T_0$, we have

$$\varepsilon_6(t) = \gamma_{12}(t) = \int_0^{T_0} [A + B(t-\tau)]\frac{\tau_{max}}{T_0}d\tau + \int_{T_0}^{t}(0)d\tau = A\tau_{max} + B\tau_{max}t - \frac{B\tau_{max}T_0}{2}$$

8.2.2 Differential Equations and Spring–Dashpot Models

Although the Boltzmann superposition integral is a valid mathematical expression of the stress–strain relationship for a linear viscoelastic material, it does not lend itself easily to the use of physical models that help us to understand viscoelastic behavior better. In this section, Laplace transforms will be used to convert the Boltzmann superposition integral to an ordinary differential equation involving time derivatives of stress and strain. Physical models for viscoelastic behavior can be easily interpreted by using differential equations.

The Laplace transform, $\mathscr{L}[f(t)]$ or $\bar{f}(s)$, of a function $f(t)$ is defined by

$$\mathscr{L}[f(t)] = \bar{f}(s) = \int_0^{\infty} f(t)e^{-st}dt \tag{8.13}$$

where s is the Laplace parameter. For purposes of illustration, we now take the Laplace transform of the 1-D Boltzmann superposition integral given by equation (8.6). The Laplace transform of both sides of the equation is given by

$$\mathscr{L}[\sigma(t)] = \bar{\sigma}(s) = \mathscr{L}\left[\int_{-\infty}^{t} C(t-\tau)\frac{d\varepsilon(\tau)}{d\tau}d\tau\right] \tag{8.14}$$

Noting that the right-hand side of equation (8.14) is in the form of a convolution integral [6], we can also write

$$\bar{C}(s)\frac{d\bar{\varepsilon}(s)}{d\tau} = \mathscr{L}\left[\int_{-\infty}^{t} C(t-\tau)\frac{d\varepsilon(\tau)}{d\tau}d\tau\right] \tag{8.15}$$

Taking the inverse Laplace transform of equation (8.15), we find that

$$\mathscr{L}^{-1}\left[\bar{C}(s)\frac{d\bar{\varepsilon}(s)}{d\tau}\right] = \int_{-\infty}^{t} C(t-\tau)\frac{d\varepsilon(\tau)}{d\tau}d\tau \tag{8.16}$$

Thus, equation (8.14) can be written as

$$\bar{\sigma}(s) = \mathscr{L}\left[\mathscr{L}^{-1}\left(\bar{C}(s)\frac{d\bar{\varepsilon}(s)}{d\tau}\right)\right] = \bar{C}(s)\frac{d\bar{\varepsilon}(s)}{d\tau} \tag{8.17}$$

But from the properties of Laplace transforms of derivatives [6],

$$\mathscr{L}\left[\frac{d\varepsilon(\tau)}{d\tau}\right] = \frac{d\bar{\varepsilon}(s)}{d\tau} = s\bar{\varepsilon}(s) - \varepsilon(0) \tag{8.18}$$

where $\varepsilon(0)$ is the initial strain. If we neglect the initial conditions, equation (8.17) becomes

$$\bar{\sigma}(s) = s\bar{C}(s)\bar{\varepsilon}(s) \tag{8.19}$$

If we perform similar operations on equation (8.5), we find that

$$\bar{\varepsilon}(s) = s\bar{S}(s)\bar{\sigma}(s) \tag{8.20}$$

Note that equation (8.19) and equation (8.20) are now of the same form as Hooke's law for linear elastic materials, except that the Laplace transforms of the stresses and strains are linearly related, and the proportionality constants are the Laplace transform of the creep compliance and the Laplace transform of the relaxation modulus. This is another example of the correspondence between the equations for elastic and viscoelastic materials and is another building block in the Elastic–Viscoelastic Correspondence Principle, which will be discussed later. Note also that according to equation (8.19) and equation (8.20), the Laplace transform of the creep compliance and the Laplace transform of the relaxation modulus must be related by

$$\bar{S}(s) = \frac{1}{s^2\bar{C}(s)} \tag{8.21}$$

However, the corresponding time domain properties are not mathematically related by a simple inverse relationship. That is, in general,

$$S(t) \neq \frac{1}{C(t)} \tag{8.22}$$

However, a usually good approximation is

$$S(t) \approx \frac{1}{C(t)} \tag{8.23}$$

and it can be shown by using the Initial Value Theorem and the Final Value Theorem of Laplace transforms (see Problem 8.2) that for short times when $t \to 0$ and for long times when $t \to \infty$, the mathematically exact relationship is

$$S(t) = \frac{1}{C(t)} \tag{8.24}$$

The coefficient term in equation (8.20) can also be written as a ratio of two polynomials in the Laplace parameter s as follows:

$$\bar{\varepsilon}(s) = s\bar{S}(s)\bar{\sigma}(s) = \frac{Q(s)}{P(s)}\bar{\sigma}(s) \tag{8.25}$$

where

$$P(s) = a_0 + a_1 s + a_2 s^2 + \cdots + a_n s^n$$

$$Q(s) = b_0 + b_1 s + b_2 s^2 + \cdots + b_n s^n$$

Thus, we can write

$$P(s)\bar{\varepsilon}(s) = Q(s)\bar{\sigma}(s) \tag{8.26}$$

But if we neglect the initial conditions, the Laplace transform of the nth derivative of a function $f(t)$ is

$$\mathscr{L}\left[\frac{d^n f(t)}{dt^n}\right] = s^n \bar{f}(s) \tag{8.27}$$

Making use of equation (8.27) and taking the inverse Laplace transform of equation (8.26), we find that

$$a_n \frac{d^n\varepsilon}{dt^n} + \cdots + a_2 \frac{d^2\varepsilon}{dt^2} + a_1 \frac{d\varepsilon}{dt} + a_0\varepsilon = b_0\sigma + b_1 \frac{d\sigma}{dt} + b_2 \frac{d^2\sigma}{dt^2} + \cdots + b_n \frac{d^n\sigma}{dt^n} \tag{8.28}$$

Thus, linear viscoelastic behavior may also be described by an ordinary differential equation as well as by the Boltzmann superposition integral. Note that the linear elastic material described by Hooke's law is a special case of equation (8.28) when all time derivatives of stress and strain vanish (i.e., $a_0\varepsilon = b_0\sigma$). Recall that one of the physical manifestations of viscoelastic behavior is the dependence of stress on strain rate; such strain rate effects can be modeled with equation (8.28). We now consider several simple physical models of linear viscoelastic behavior that include various time derivatives of stress and strain.

As shown in figure 8.8 to figure 8.10, useful physical models can be constructed from simple elements such as the elastic spring and the viscous dashpot, where the spring of modulus k is assumed to follow Hooke's law and the dashpot is assumed to be filled with a Newtonian fluid of viscosity μ. Thus, the stress–strain relationship for the elastic spring element is of the form $\varepsilon = \sigma/k$, whereas the corresponding equation for the viscous dashpot is $d\varepsilon/dt = \sigma/\mu$.

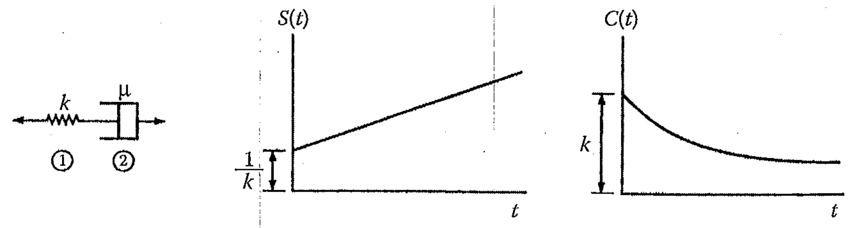

(a) Spring-dashpot arrangement (b) Creep compliance vs. time (c) Relaxation modulus vs. time

FIGURE 8.8
Maxwell model, with corresponding creep and relaxation curves.

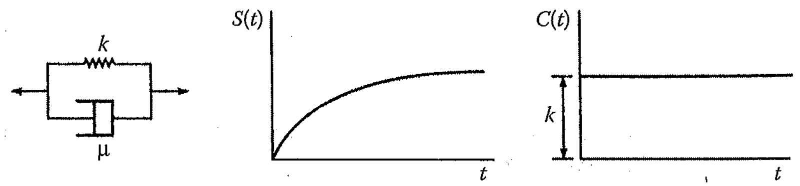

(a) Spring-dashpot arrangement (b) Creep compliance vs. time (c) Relaxation modulus vs. time

FIGURE 8.9
Kelvin–Voigt model, with corresponding creep and relaxation curves.

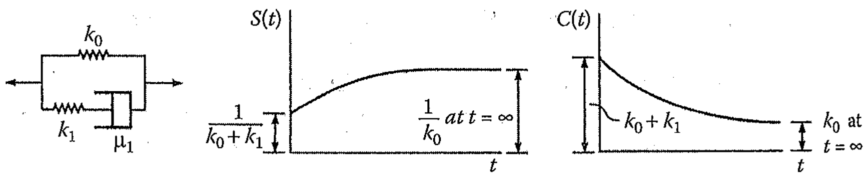

(a) Spring-dashpot arrangement (b) Creep compliance vs. time (c) Relaxation modulus vs. time

FIGURE 8.10
Standard linear solid or Zener model, with corresponding creep and relaxation curves.

The Maxwell model consists of a spring and a dashpot in series, as shown in figure 8.8(a). The total strain across a model of unit length must equal the sum of the strains in the spring and the dashpot, so that

$$\varepsilon = \varepsilon_1 + \varepsilon_2 \tag{8.29}$$

and the strain rate across the model is then

$$\frac{d\varepsilon}{dt} = \frac{d\varepsilon_1}{dt} + \frac{d\varepsilon_2}{dt} = \frac{1}{k}\frac{d\sigma}{dt} + \frac{\sigma}{\mu} \tag{8.30}$$

Note that equation (8.30) is just a special case of equation (8.28), with only first derivatives of stress and strain. For creep at constant stress $\sigma = \sigma_0$, equation (8.30) reduces to

$$\frac{d\varepsilon}{dt} = \frac{\sigma_0}{\mu} \tag{8.31}$$

Integrating equation (8.31) once, we find that

$$\varepsilon(t) = \frac{\sigma_0}{\mu}t + C_1 \tag{8.32}$$

where the constant of integration, C_1, is found from the initial condition $\varepsilon(0) = C_1\ \sigma = \sigma_0/k$. Thus, the creep strain for the Maxwell model is given by

$$\varepsilon(t) = \frac{\sigma_0}{\mu}t + \frac{\sigma_0}{k} \tag{8.33}$$

and the corresponding creep compliance is given by

$$S(t) = \frac{\varepsilon(t)}{\sigma_0} = \frac{t}{\mu} + \frac{1}{k} \tag{8.34}$$

A plot of the creep compliance versus time according to equation (8.34) is shown in figure 8.8(b). The type of creep behavior that is actually observed in experiments is more like that shown in figure 8.5, however. Thus, the Maxwell model does not adequately describe creep.

For relaxation at constant strain $\varepsilon = \varepsilon_0$, the Maxwell model of stress–strain relationship in equation (8.30) becomes

$$0 = \frac{1}{k}\frac{d\sigma}{dt} + \frac{\sigma}{\mu} \tag{8.35}$$

Integrating equation (8.35) once, we find

$$\ln\sigma = -\frac{k}{\mu}t + C_2 \tag{8.36}$$

where the constant of integration, C_2, is found from the initial condition $\sigma(0) = \sigma_0$. The resulting stress relaxation function is

$$\sigma(t) = \sigma_0 e^{-kt/\mu} = \sigma_0 e^{-t/\lambda} \tag{8.37}$$

where $\lambda = \mu/k$ is the relaxation time, or the time required for the stress to relax to $1/e$, or 37% of its initial value. The relaxation time is therefore a measure of the internal time scale of the material. The corresponding relaxation modulus is

$$C(t) = \frac{\sigma(t)}{\varepsilon_0} = \frac{\sigma_0}{\varepsilon_0} e^{-t/\lambda} = k e^{-t/\lambda} \tag{8.38}$$

Figure 8.8(c) shows the relaxation modulus versus time from equation (8.38), which is in general agreement with the type of relaxation observed experimentally. Thus, the Maxwell model appears to describe adequately the relaxation phenomenon, but not the creep response.

Figure 8.9(a) shows the Kelvin–Voigt model, which consists of a spring and a dashpot in parallel. Using the appropriate equations for a parallel arrangement and following a procedure similar to the one just outlined, it can be shown that the differential equation describing the behavior of the Kelvin–Voigt model is given by

$$\sigma = k\varepsilon + \mu\frac{d\varepsilon}{dt} \tag{8.39}$$

Equation (8.39) is seen to be another special case of equation (8.28), with only first derivatives of strain. It can also be shown that the creep compliance for the Kelvin–Voigt model is given by

$$S(t) = \frac{1}{k}[1 - e^{-t/\rho}] \tag{8.40}$$

where $\rho = \mu/k$ is now referred to as the retardation time. Similarly, the relaxation modulus is given by

$$C(t) = k \tag{8.41}$$

Equation (8.40) and equation (8.41) are plotted in figure 8.9(b) and figure 8.9(c), respectively. The creep compliance curve agrees with experimental observation, except that the initial elastic response is missing. On the other hand, the relaxation modulus has not been observed to be constant, as shown in figure 8.9(c). Thus, like the Maxwell model, the Kelvin–Voigt model does not adequately describe all features of experimentally observed creep and relaxation.

One obvious way to improve the spring–dashpot model is to add more elements. One such improved model, shown in figure 8.10(a), is referred to as the standard linear solid or Zener model. It can be shown that the differential equation for the Zener model is given by

$$\sigma + \frac{\mu_1}{k_1}\frac{d\sigma}{dt} = k_0\varepsilon + \frac{\mu_1}{k_1}(k_0 + k_1)\frac{d\varepsilon}{dt} \tag{8.42}$$

where the parameters k_0, k_1, and μ_1 are defined in figure 8.10(a). Equation (8.42) is obviously another special case of the general differential equation (8.28). It is also interesting to note that the Zener model shown in figure 8.10(a) is just a Maxwell model in parallel with a spring. The creep compliance for the Zener model is given by

$$S(t) = \frac{1}{k_0}\left[1 - \frac{k_1}{k_0 + k_1} e^{-t/\rho_1}\right] \tag{8.43}$$

where $\rho_1 = (\mu_1/k_0k_1)(k_0 + k_1)$ is the retardation time.

As shown in figure 8.10(b), the shape of the creep compliance curve from equation (8.43) matches the expected shape based on experimental observations. The relaxation modulus for the Zener model is given by

$$C(t) = k_0 + k_1 e^{-t/\lambda_1} \tag{8.44}$$

where $\lambda_1 = \mu_1/k_1$ is the relaxation time. Note that λ_1 is just the relaxation time for the Maxwell model consisting of μ_1 and k_1. Figure 8.10(c) shows the predicted relaxation modulus curve from equation (8.44), and, again, the general shape of the curve appears to be similar to what is experimentally observed.

Although the Zener model is the simplest spring–dashpot model that correctly describes all expected features of experimentally observed creep and relaxation behavior in linear viscoelastic materials, it still is not completely adequate. This remaining inadequacy is best described by plotting the relaxation modulus versus the logarithm of time, as shown in figure 8.11. Practically speaking, complete relaxation for the Zener model occurs in less

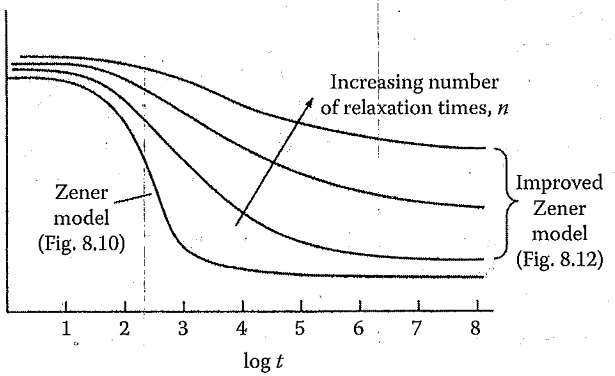

FIGURE 8.11
Effect of increasing number of relaxation times on relaxation curve of Zener model.

than a decade in time, but relaxation for real polymers happens over a much longer time scale. For example, the glass-to-rubber transition, which is only one region of polymer viscoelastic behavior, takes about six to eight decades in time to complete [7]. This extended relaxation period for polymers is due to the existence of a distribution of relaxation times. By using an improved Zener model such as the parallel arrangement shown in figure 8.12, we can introduce such a distribution of relaxation times, λ_i, that makes it possible to extend the range of relaxation to more realistic values. This form of the improved Zener model consists of n Maxwell elements in parallel with the elastic spring, k_0. It can be easily shown that the relaxation modulus for this improved Zener model is given by

$$C(t) = k_0 + \sum_{i=1}^{n} k_i e^{-t/\lambda_i} \tag{8.45}$$

where $\lambda_i = \mu_i / k_i$ is the relaxation time for the ith Maxwell element.

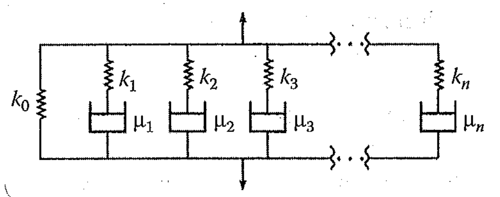

FIGURE 8.12
Improved Zener model, parallel arrangement.

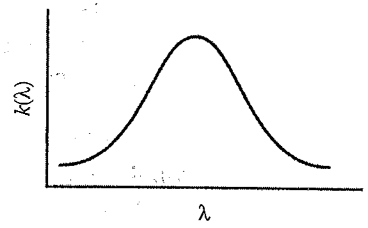

FIGURE 8.13
Continuous distribution of relaxation times, or relaxation spectrum $k(\lambda)$, for improved Zener model of figure 8.12, with an infinite number of elements.

As shown in figure 8.11, the effect of increasing n and the corresponding number of relaxation times is to broaden the range of relaxation. The number of relaxation times needed to describe adequately the viscoelastic behavior of a particular material must be determined experimentally. For an infinite number of elements in the improved Zener model of figure 8.12 and a continuous distribution of relaxation times, the relaxation modulus can be expressed as [8]

$$C(t) = k_0 + \int_0^{\infty} k(\lambda) e^{-t/\lambda} d\lambda \tag{8.46}$$

where $k(\lambda)$ is the distribution of relaxation times, or the relaxation spectrum, which is shown schematically in figure 8.13.

By considering an alternative form of an improved Zener model consisting of a spring in series with n Kelvin–Voigt elements, as shown in figure 8.14, it can be shown that the corresponding creep compliance expression is

$$S(t) = \frac{1}{k_0} + \sum_{i=1}^{n} \frac{1}{k_i}[1 - e^{-t/\rho_i}] \tag{8.47}$$

where $\rho_i = \mu_i / k_i$ is the retardation time for the ith Kelvin–Voigt element.

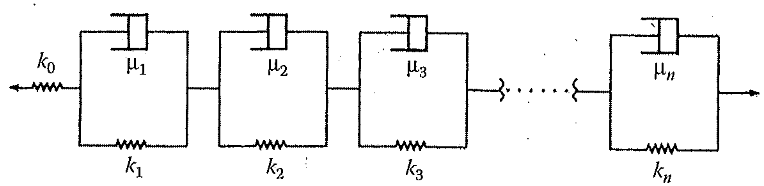

FIGURE 8.14
Improved Zener model, series arrangement.

Although the above equations have been derived on the basis of simple spring–dashpot models, the generalized relaxation modulus and creep compliance expressions for anisotropic linear viscoelastic composites have the same forms as equation (8.45) and equation (8.47), respectively. According to Schapery [1], if the elastic moduli are positive definite (i.e., always either positive or equal to zero), it can be shown using thermodynamic theory that the generalized expressions corresponding to equation (8.45) and equation (8.47) are, respectively,

$$C_{ij}(t)=\sum_{m=1}^{n} C_{ij}^{(m)} e^{-t/\lambda_m}+C_{ij} \tag{8.48}$$

and

$$S_{ij}(t)=\sum_{m=1}^{n} S_{ij}^{(m)}[1-e^{-t/\rho_m}]+S_{ij} \tag{8.49}$$

where

$i, j = 1, 2, \ldots, 6$

C_{ij}, S_{ij} = elastic moduli and compliances, respectively

λ_m, ρ_m = relaxation times and retardation times, respectively

$C_{ij}^{(m)}$, $S_{ij}^{(m)}$ = coefficients corresponding to λ_m and ρ_m, respectively

As with the simple spring–dashpot models, the numerical values of the parameters on the right-hand side of equation (8.48) and equation (8.49) must be determined experimentally.

The relaxation times and retardation times are strongly dependent on temperature, and such temperature dependence is the basis of the time–temperature superposition (TTS) method, which will be discussed later. It is assumed here that the materials are "thermorheologically simple." That is, all the relaxation times, λ_i, and the retardation times, ρ_i, are assumed to have the same temperature dependence. A similar argument holds for the effect of aging, which will also be discussed later.

EXAMPLE 8.2

For the problem in example 8.1, the effective shear compliance is to be approximated by a Kelvin–Voigt model of the form

$$S_{66}(t)=\frac{1}{k}(1-e^{-t/\lambda}), \quad \text{when } t \geq 0$$

$$S_{66}(t)=0, \quad \text{when } t<0$$

Determine the creep strain at $t < T_0$ *and* $t > T_0$.

Solution. For the case of $t < T_0$, equation (8.7) reduces to

$$\gamma_{12}(t)=\int_0^t \frac{1}{k}[1-e^{-(t-\tau)/\lambda}]\frac{\tau_{\max}}{T_0}d\tau=\frac{\tau_{\max}}{kT_0}[t-\lambda(1-e^{-t/\lambda})]$$

and for $t > T_0$, we have

$$\gamma_{12}(t)=\int_0^{T_0} \frac{1}{k}[1-e^{-(t-\tau)/\lambda}]\frac{\tau_{\max}}{T_0}d\tau+(0)=\frac{\tau_{\max}}{kT_0}\left[T_0-\lambda e^{-t/\lambda}(e^{T_0/\lambda}-1)\right]$$

8.2.3 Quasi-Elastic Analysis

From the previous section, it should be clear that the generalized Boltzmann superposition integrals in equation (8.7) and equation (8.9) can be Laplace transformed to yield equations of the form

$$\bar{\varepsilon}_i(s)=s\bar{S}_{ij}(s)\bar{\sigma}_j(s) \tag{8.50}$$

and

$$\bar{\sigma}_i(s)=s\bar{C}_{ij}(s)\bar{\varepsilon}_j(s) \tag{8.51}$$

These equations are of the same form as the corresponding elastic stress–strain relationships and are presumably easier to work with than the integral equations. In a practical analysis or design problem involving the use of these equations, however, the problem solution in the Laplace domain would then have to be inverse transformed to get the desired time-domain result, and this can present difficulties. Schapery [1] has presented several approximate methods for performing such inversions. If the input stresses or strains are constant, however, there is no need for inverse transforms and the time-domain equations turn out to be very simple. Schapery refers to this as a "quasi-elastic analysis," and the equations used in such an analysis will be developed in the remainder of this section.

Consider a generalized creep problem with time-varying stresses $\sigma_j(t)$ given by

$$\sigma_j(t)=\sigma_j' H(t) \tag{8.52}$$

where $j = 1, 2, \ldots, 6$, the σ_j' are constant stresses, and $H(t)$ is the unit step function, or Heaviside function, shown in figure 8.15(a) and defined as

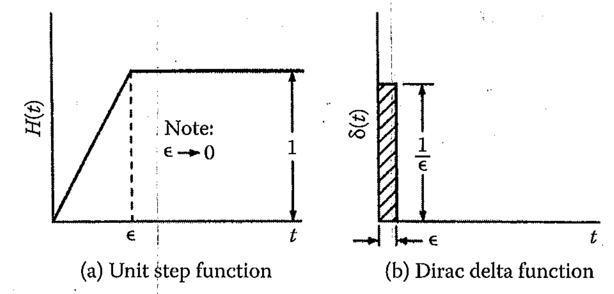

FIGURE 8.15
Unit step function and Dirac delta function.

follows [3]:

$$\lim_{\varepsilon \to 0} H(t) = \begin{cases} 0 & \text{for } t \le 0 \\ t/\varepsilon & \text{for } 0 \le t \le \varepsilon \\ 1 & \text{for } t \ge \varepsilon \end{cases} \tag{8.53}$$

The unit step function can be easily shifted along the time axis by an amount ξ by writing the function as $H(t-\xi)$. Substituting the stresses from equation (8.52) in the Boltzmann superposition integral, equation (8.7), we find that the resulting strains are given by

$$\varepsilon_i(t) = \int_{-\infty}^{t} S_{ij}(t-\tau)\sigma_j' \frac{dH(\tau)}{d\tau} d\tau \tag{8.54}$$

but according to equations (8.53), the derivative of the step function must be

$$\frac{dH(t)}{dt} = \delta(t) = \begin{cases} 0 & \text{for } t \le 0 \\ 1/\varepsilon & \text{for } 0 \le t \le \varepsilon \\ 0 & \text{for } t \ge 0 \end{cases} \tag{8.55}$$

where the parameter ε can be made arbitrarily small, the derivative in equation (8.55) is taken before $\varepsilon \to 0$, and $\delta(t)$ is the Dirac delta function shown in figure 8.15(b). Thus, the integral in equation (8.54) can be written as

$$\varepsilon_i(t) = \left\{ \int_{-\infty}^{t} S_{ij}(t-\tau)\delta(\tau)d\tau \right\} \sigma_j' \tag{8.56}$$

where the constants σ_j' have been moved outside the integral. According to the properties of convolution integrals [6], we can also write

$$\varepsilon_i(t) = \left\{ \int_{-\infty}^{t} S_{ij}(\tau)\delta(t-\tau)d\tau \right\} \sigma_j' \tag{8.57}$$

This integral can be broken down and rewritten as follows:

$$\varepsilon_i(t) = \left\{ \int_{-\infty}^{t-\varepsilon} (0)d\tau + \int_{t-\varepsilon}^{t} S_{ij}(t)\delta(t-\tau)d\tau \right\} \sigma_j' \tag{8.58}$$

where the $S_{ij}(\tau)$ evaluated over the interval $t-\varepsilon \le \tau \le t$ can be approximated as $S_{ij}(t)$ since ε is very small. The $S_{ij}(t)$ can now be moved outside the integral, leaving the integral of the Dirac delta function, which is defined as [6]

$$\int_{t-\varepsilon}^{t} \delta(t-\tau)d\tau = 1 \tag{8.59}$$

Thus, the final result is

$$\varepsilon_i(t) = S_{ij}(t)\sigma_j' \tag{8.60}$$

The form of this equation suggests that we can solve for creep strains under constant stresses, σ_j', by simply replacing the elastic compliances, S_{ij}, in Hooke's law (eq. [2.5]) with the corresponding viscoelastic creep compliances, $S_{ij}(t)$. Similarly, it can be shown that if the constant strain inputs

$$\varepsilon_j(t) = \varepsilon_j' H(t) \tag{8.61}$$

are substituted in equations (8.9), the resulting stresses must be

$$\sigma_i(t) = C_{ij}(t)\varepsilon_j' \tag{8.62}$$

Thus, the stress relaxation under constant strains can be found by replacing the elastic moduli, C_{ij}, in Hooke's law (eq. [2.3]) with the corresponding viscoelastic relaxation moduli, $C_{ij}(t)$. Equation (8.60) and equation (8.62) form the basis of the so-called "quasi-elastic analysis" and obviously eliminate the need for Laplace transform analysis in the stress–strain relationships. It should be emphasized again, however, that equation (8.60) and equation (8.62) are only valid for constant or near-constant inputs. Such equations give additional hints of a direct correspondence between the equations for linear elastic systems and those for linear viscoelastic systems, and this correspondence will be discussed in more detail later.

The quasi-elastic approach has been successfully used in a number of practical applications such as micromechanical modeling of creep in polymer composites [9], prediction of creep in rotating viscoelastic disks [10], analysis of creep in prestressed composite connectors [11], and modeling of creep in prestressed polymer composite lubricators [12]. Many of these applications involve finite element implementations of the quasi-elastic approach, where finite element models are employed to solve a series of elastic problems, and the time dependence is accounted for by using different elastic moduli at each time step.

EXAMPLE 8.3

The filament wound pressure vessel described in example 2.3 is constructed of a viscoelastic composite having creep compliances that can be modeled by using one-term series representations of the form shown in equations (8.49). Assuming that the internal pressure, p, is constant, determine the creep strains along the principal material directions in the wall of the vessel.

Solution. Since the internal pressure, p, is constant, the stresses in the wall of the vessel are all constant, and we can use a quasi-elastic analysis to predict the creep strains. From equations (8.60), we find that the creep strains along the principal material directions are given by

$$\varepsilon_1(t) = S_{11}(t)\sigma_1 + S_{12}(t)\sigma_2$$

$$\varepsilon_2(t) = S_{12}(t)\sigma_1 + S_{22}(t)\sigma_2$$

and

$$\epsilon_6(t) = \gamma_{12}(t)\sigma_1 + S_{66}(t)\tau_2$$

From example 2.3, stresses along the principal material directions were found to be

$$\sigma_1 = 20.5p \text{ MPa}$$
$$\sigma_2 = 17.0p \text{ MPa}$$
$$\sigma_6 = \sigma_{12} = \tau_{12} = 6.0p \text{ MPa}$$

Substituting these stresses and the creep compliances from equations (8.49) in the above expressions for the strains, we find that

$$\varepsilon_1(t) = \left(S_{11}^{(1)}[1-e^{-t/\rho_1}] + S_{11}\right)(20.5p) + \left(S_{12}^{(1)}[1-e^{-t/\rho_1}] + S_{12}\right)(17.0p)$$

$$\varepsilon_2(t) = \left(S_{12}^{(1)}[1-e^{-t/\rho_1}] + S_{12}\right)(20.5p) + \left(S_{22}^{(1)}[1-e^{-t/\rho_1}] + S_{22}\right)(17.0p)$$

$$\gamma_{12}(t) = \left(S_{66}^{(1)}[1-e^{-t/\rho_1}] + S_{66}\right)(6.0p)$$

8.2.4 Sinusoidal Oscillations and Complex Modulus Notation

In the previous section, it was shown that when the inputs are constant, the Boltzmann superposition integrals are reduced to simple algebraic equations that resemble the linear elastic Hooke's law. In this section, an analogous simplification will be demonstrated for the case of stresses or strains that vary sinusoidally with time. The results will make it much easier to analyze sinusoidal vibrations of viscoelastic composites. The general procedure here follows that presented by Fung [3].

Consider the case where the stresses vary sinusoidally with frequency ω. Using the contracted notation and complex exponentials, such stresses can be written as

$$\tilde{\sigma}_n(t) = A_n e^{i\omega t} \tag{8.63}$$

where
$n = 1, 2, \ldots, 6$
i = imaginary operator, is $(-1)^{1/2}$
A_n = complex stress amplitudes
~ = superscript denoting a sinusoidally varying quantity

Substituting equation (8.63) in equation (8.7), we find that the resulting sinusoidally varying strains are given by

$$\tilde{\varepsilon}_m(t) = \int_{-\infty}^{t} S_{mn}(t-\tau) i\omega A_n e^{i\omega\tau} d\tau \tag{8.64}$$

where $m, n = 1, 2, \ldots, 6$.

It is now convenient to define a new variable $\xi = t - \tau$, so that

$$\tilde{\varepsilon}_m(t) = \int_{0}^{\infty} S_{mn}(\xi) e^{-i\omega\xi} i\omega A_n e^{i\omega t} d\xi \tag{8.65}$$

The terms not involving functions of ξ may be moved outside the integral, and since $S_{mn}(t) = 0$ for $t < 0$, the lower limit on the integral can be changed to $-\infty$, so that

$$\tilde{\varepsilon}_m(t) = i\omega A_n e^{i\omega t} \int_{-\infty}^{\infty} S_{mn}(\xi) e^{-i\omega\xi} d\xi \tag{8.66}$$

The integral in equation (8.66) is just the Fourier transform of the creep compliances, $\mathscr{F}[S_{mn}(\xi)]$, or $S_{mn}(\omega)$, which is written as

$$\mathscr{F}[S_{mn}(\xi)] = S_{mn}(\omega) = \int_{-\infty}^{\infty} S_{mn}(\xi) e^{-i\omega\xi} d\xi \tag{8.67}$$

Thus, the stress–strain relationship reduces to

$$\tilde{\varepsilon}_m(t) = i\omega S_{mn}(\omega) A_n e^{i\omega t} = i\omega S_{mn}(\omega)\tilde{\sigma}_n(t) \tag{8.68}$$

In order to get this equation to resemble Hooke's law more closely, we simply define the frequency-domain complex compliances as follows:

$$S^*_{mn}(\omega) = i\omega S_{mn}(\omega) \tag{8.69}$$

so that equation (8.68) becomes

$$\tilde{\varepsilon}_m(t) = S^*_{mn}(\omega)\tilde{\sigma}_n(t) \tag{8.70}$$

Thus, in linear viscoelastic materials, the sinusoidally varying stresses are related to the sinusoidally varying strains by complex compliances in the same way that static stresses and strains are related by elastic compliances in the linear elastic material. In addition, the time-domain creep compliances are related to frequency-domain complex compliances by Fourier transforms. It is important to note, however, that the complex compliance is not simply equal to the Fourier transform of the corresponding creep compliance. According to equation (8.69), the complex compliance, $S^*_{mn}(\omega)$, is equal to a factor of $i\omega$ times $S_{mn}(\omega)$, and $S_{mn}(\omega)$ is the Fourier transform of the creep compliance $S_{mn}(t)$.

Alternatively, if we substitute sinusoidally varying strains in equation (8.9), we find that the sinusoidally varying stresses are

$$\tilde{\sigma}_m(t) = C^*_{mn}(\omega)\tilde{\varepsilon}_n(t) \tag{8.71}$$

where the complex moduli are defined by

$$C^*_{mn}(\omega) = i\omega C_{mn}(\omega) \tag{8.72}$$

and the $C_{mn}(\omega)$ are the Fourier transforms of the corresponding relaxation moduli, $C_{mn}(t)$. Alternatively, equation (8.70) and equation (8.71) may be written in matrix form as

$$\{\tilde{\varepsilon}(t)\} = [S^*(\omega)]\{\tilde{\sigma}(t)\} \tag{8.73}$$

and

$$\{\tilde{\sigma}(t)\} = [C^*(\omega)]\{\tilde{\varepsilon}(t)\} \tag{8.74}$$

respectively, where the complex compliance matrix and the complex modulus matrix must be related by $[S^*(\omega)] = [C^*(\omega)]^{-1}$.

The complex modulus notation not only has a mathematical basis in viscoelasticity theory, but it also has a straightforward physical interpretation. Since the complex modulus is a complex variable, we can write it in terms of its real and imaginary parts as follows:

$$C^*_{mn}(\omega) = C'_{mn}(\omega) + iC''_{mn}(\omega) = C'_{mn}(\omega)[1 + i\eta_{mn}(\omega)] = |C^*_{mn}(\omega)|\, e^{-i\delta_{mn}(\omega)} \tag{8.75}$$

(no summation on m and n in eq. [8.75]), where

$C'_{mn}(\omega)$ = storage modulus
$C''_{mn}(\omega)$ = loss modulus
$\eta_{mn}(\omega)$ = loss factor = $\tan[\delta_{mn}(\omega)] = (C''_{mn}(\omega)/C'_{mn}(\omega))$
$\delta_{mn}(\omega)$ = phase lag between $\tilde{\sigma}_m(t)$ and $\tilde{\varepsilon}_n(t)$

Thus, the real part of the complex modulus is associated with elastic energy storage, whereas the imaginary part is associated with energy dissipation, or damping. A physical interpretation of the 1-D forms of these equations may be given with the aid of the rotating vector diagram in figure 8.16. The stress and strain vectors are both assumed to be rotating with angular velocity ω, and the physical oscillation is generated by either the horizontal or the vertical projection of the vectors. The complex exponential representations of the rotating stress and strain vectors in the diagram are

$$\tilde{\sigma}(t) = \sigma e^{i(\omega t + \delta)} \quad \text{and} \quad \tilde{\varepsilon}(t) = \varepsilon e^{i\omega t} \tag{8.76}$$

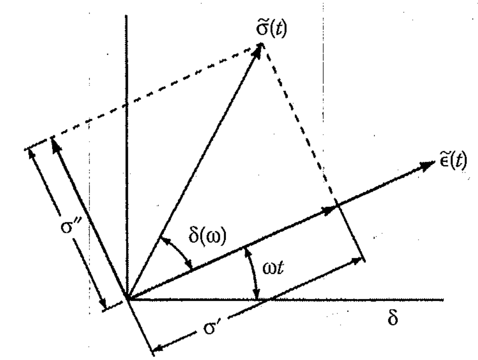

FIGURE 8.16
Rotating vector diagram for physical interpretation of the complex modulus.

so that the 1-D complex modulus is defined as

$$C^*(\omega) = \frac{\tilde{\sigma}(t)}{\tilde{\varepsilon}(t)} = \frac{\sigma e^{i\delta}}{\varepsilon} = \frac{\sigma}{\varepsilon}(\cos\delta + i\sin\delta) = \frac{\sigma'}{\varepsilon} + i\frac{\sigma''}{\varepsilon}$$
$$= C'(\omega) + iC''(\omega) = C'(\omega)[1 + i\eta(\omega)] \tag{8.77}$$

It is seen that the strain lags the stress by the phase angle δ; the storage modulus, $C'(\omega)$, is the in-phase component of the stress, σ', divided by the strain, ε; the loss modulus, $C''(\omega)$, is the out-of-phase component of stress, σ'', divided by the strain, ε; and the loss factor, $\eta(\omega)$, is the tangent of the phase angle δ. Experimental determination of the complex modulus involves the measurement of the storage modulus, $C'(\omega)$, and the loss factor, $\eta(\omega)$, as a function of frequency, ω; several techniques for doing this will be described in chapter 10.

The inverse Fourier transform of the parameter $S_{mn}(\omega)$ is the creep compliance $S_{mn}(t)$, as given by

$$\mathscr{F}^{-1}[S_{mn}(\omega)] = S_{mn}(t) = \frac{1}{2\pi}\int_{-\infty}^{\infty} S(\omega)e^{i\omega t}d\omega \tag{8.78}$$

where $\mathscr{F}^{-1}$ is the inverse Fourier transform operator. Equation (8.67) and equation (8.78) form the so-called Fourier transform pair, which makes it possible to transform back and forth between the time domain and the frequency domain [13]. Since experimental frequency data are usually expressed in units of cycles per second, or Hz, it is convenient to define

the frequency as $f = \omega/2\pi$ (Hz), so that the Fourier transform pair now becomes symmetric in form:

$$\mathscr{F}[S_{mn}(t)] = S_{mn}(f) = \int_{-\infty}^{\infty} S_{mn}(t)e^{-i2\pi ft}dt \tag{8.79}$$

and

$$\mathscr{F}^{-1}[S_{mn}(f)] = S_{mn}(t) = \int_{-\infty}^{\infty} S_{mn}(f)e^{i2\pi ft}df \tag{8.80}$$

It can be shown that the time-domain relaxation modulus and the corresponding frequency-domain complex modulus are related by a similar Fourier transform pair. As a further indication of the usefulness of such equations, inverse Fourier transforms have been used to estimate time-domain creep behavior of composites from frequency-domain complex modulus data obtained from vibration tests of the same materials [14].

EXAMPLE 8.4

The composite pressure vessel described in example 2.3 and example 8.3 has an internal pressure p that varies sinusoidally with time, as shown in figure 8.17. If the complex compliances of the composite material are given by

$$S^*_{mn}(\omega) = S'_{mn}(\omega) + iS''_{mn}(\omega)$$

determine all the time-dependent strains associated with the principal material axes.

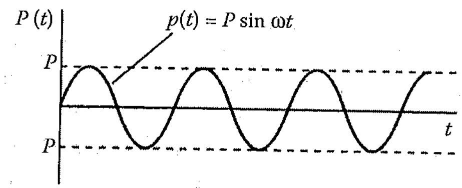

FIGURE 8.17
Sinusoidally varying pressure for example 8.4.

Solution. From example 2.3 and figure 8.17, the stresses along the 12 directions are

$$\tilde{\sigma}_1(t) = 20.5p = 20.5P\sin\omega t(\text{MPa})$$

$$\tilde{\sigma}_2(t) = 17.0p = 17.0P\sin\omega t(\text{MPa})$$

$$\tilde{\sigma}_6(t) = \tilde{\tau}_{12}(t) = 6.0p = 6.0P\sin\omega t(\text{MPa})$$

The corresponding strains from equations (8.70) are

$$\tilde{\varepsilon}_1(t) = S_{11}^*(\omega)\tilde{\sigma}_1(t) + S_{12}^*(\omega)\tilde{\sigma}_2(t) + (0)\tilde{\sigma}_6(t)$$

$$= [S'_{11}(\omega) + iS''_{11}(\omega)]20.5P\sin\omega t + [S'_{12}(\omega) + iS''_{12}(\omega)]17.0P\sin\omega t$$

$$\tilde{\varepsilon}_2(t) = S_{12}^*(\omega)\tilde{\sigma}_1(t) + S_{22}^*(\omega)\tilde{\sigma}_2(t) + (0)\tilde{\sigma}_6(t)$$

$$= [S'_{12}(\omega) + iS''_{12}(\omega)]20.5P\sin\omega t + [S'_{22}(\omega) + iS''_{22}(\omega)]17.0P\sin\omega t$$

$$\tilde{\varepsilon}_6(t) = \tilde{\gamma}_{12}(t) = S_{66}^*(\omega)\tilde{\sigma}_6(t) = S_{66}^*(\omega)\tilde{\tau}_{12}(t)$$

$$= [S'_{66}(\omega) + iS''_{66}(\omega)]6.0P\sin\omega t$$

8.2.5 Elastic–Viscoelastic Correspondence Principle

In the previous sections, we have seen a number of examples where the form of the stress–strain relationships for linear viscoelastic materials is the same as that for linear elastic materials. Such analogies between the equations for elastic and viscoelastic analysis have led to the formal recognition of an "Elastic–Viscoelastic Correspondence Principle." The correspondence principle for isotropic materials was apparently introduced by Lee [15], whereas the application to anisotropic materials was proposed by Biot [16]. The specific application of the correspondence principle to the viscoelastic analysis of anisotropic composites has been discussed in detail by Schapery [1,17] and Christensen [6].

A summary of the correspondences between elastic and viscoelastic stress–strain relationships is given in table 8.1. The implication of this table is that if we have the necessary equations for a linear elastic solution to a problem, we simply make the corresponding substitutions in the equations to get the corresponding linear viscoelastic solution. Although table 8.1 is only concerned with the correspondences in the stress–strain relationships, there are obviously other equations involved in a complete solution to an elasticity problem. The correspondences in the equilibrium equations, the strain–displacement relations, the boundary conditions, and the variational methods of elastic analysis are beyond the scope of

TABLE 8.1

Elastic–Viscoelastic Correspondence in Stress–Strain Relationships

Material and Input	Stresses	Strains	Properties	Equation
Linear Elastic				
Input stresses	σ_j	ε_i	S_{ij}	(2.5)
Input strains	σ_i	ε_j	C_{ij}	(2.3)
Linear Viscoelastic				
Generalized creep	$\bar{\sigma}_j(s)$	$\bar{\varepsilon}_i(s)$	$s\bar{S}_{ij}(s)$	(8.50)
Constant stress creep	$\bar{\sigma}'_j$	$\varepsilon_i(t)$	$S_{ij}(t)$	(8.60)
Generalized relaxation	$\bar{\sigma}_i(s)$	$\bar{\varepsilon}_j(s)$	$s\bar{C}_{ij}(s)$	(8.51)
Constant strain relaxation	$\sigma_i(t)$	ε'_j	$C_{ij}(t)$	(8.62)
Sinusoidal stress input	$\tilde{\sigma}_j(t)$	$\tilde{\varepsilon}_i(t)$	$S_{ij}^*(\omega)$	(8.70)
Sinusoidal strain input	$\tilde{\sigma}_i(t)$	$\tilde{\varepsilon}_j(t)$	$C_{ij}^*(\omega)$	(8.71)

Note: $i, j = 1, 2, \ldots, 6$.

this book, but detailed discussions of these are given by Schapery [1,17] and Christensen [4,6].

One of the most important implications of the correspondence principle is that analytical models for predicting elastic properties of composites at both the micromechanical and the macromechanical levels can be easily converted for prediction of the corresponding viscoelastic properties. For example, the rule of mixtures for predicting the longitudinal modulus of a unidirectional composite can now be converted for viscoelastic relaxation problems by rewriting equation (3.23) as

$$E_1(t) = E_{f1}(t)\upsilon_f + E_m(t)\upsilon_m \tag{8.81}$$

where

$E_1(t)$ = longitudinal relaxation modulus of composite
$E_{f1}(t)$ = longitudinal relaxation modulus of fiber
$E_m(t)$ = relaxation modulus of isotropic matrix
υ_f = fiber volume fraction
υ_m = matrix volume fraction

The relative viscoelasticity of fiber and matrix materials may make further simplification possible. In most polymer matrix composites, the time dependency of the matrix material would be much more significant than that of the fiber, so the fiber modulus could be assumed to be elastic, and the time dependency of $E_1(t)$ would be governed by $E_m(t)$ alone. The results of a similar analysis of the creep compliances $S_{22}(t)$ and $S_{66}(t)$ for a glass/epoxy composite are shown in figure 8.18 from ref. [18]. From these results

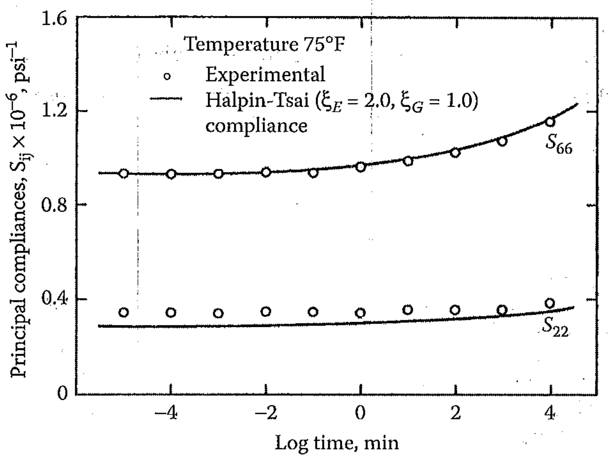

FIGURE 8.18
Measured and predicted creep compliances for glass/epoxy composite. (From Beckwith, S.W. 1974. Viscoelastic characterization of a nonlinear glass/epoxy composite including the effects of damage. Ph.D. Dissertation, Texas A&M University, College Station, TX. With permission.)

it appears that the compliances can be accurately predicted by using the viscoelastic properties of the epoxy matrix in the corresponding viscoelastic forms of the Halpin–Tsai equations (eq. [3.59] and eq. [3.60]).

And as mentioned earlier, Beckwith [2] showed experimentally that the creep exponent n, which governs the time dependency in the power law expression (eq. [8.2]), depends only on the polymer matrix.

At the macromechanical level, equations such as laminate force–deformation relationships can be converted to viscoelastic form using the correspondence principle. For example, the creep strains in a symmetric laminate under constant in-plane loading can be analyzed by employing the correspondence principle and a quasi-elastic analysis to rewrite equations (7.58) as

$$\begin{Bmatrix} \varepsilon_x^0(t) \\ \varepsilon_y^0(t) \\ \gamma_{xy}^0(t) \end{Bmatrix} = \begin{bmatrix} A'_{11}(t) & A'_{12}(t) & A'_{16}(t) \\ A'_{12}(t) & A'_{22}(t) & A'_{26}(t) \\ A'_{16}(t) & A'_{26}(t) & A'_{66}(t) \end{bmatrix} \begin{Bmatrix} N_x \\ N_y \\ N_{xy} \end{Bmatrix} \tag{8.82}$$

where

$A'_{ij}(t)$ = laminate creep compliances
N_x, N_y, N_{xy} = constant loads

Sims and Halpin [19] have used these equations, along with uniaxial creep tests, to determine the creep compliances of glass/epoxy laminates for comparison with predictions. For example, the compliance $A'_{11}(t)$ was determined by applying a constant load N_x and by measuring the creep strain, $\varepsilon_x^0(t)$, and then using the equation

$$A'_{11}(t) = \frac{\varepsilon_x^0(t)}{N_x} \tag{8.83}$$

These measured values were compared with predicted values from a combined micromechanics–macromechanics analysis that was based on the use of the correspondence principle, the Halpin–Tsai equations, and classical lamination theory. The agreement between measurements and predictions was excellent, as shown in figure 8.19.

When the correspondence principle is used for problems involving sinusoidally varying stresses and strains in viscoelastic composites, we must be particularly careful to make sure that the criteria for using the effective modulus theory are met. These restrictions are discussed in more detail, and applications of the correspondence principle to the prediction of complex moduli of particle and fiber composites are given in papers by Hashin [20,21]. For example, assuming that these criteria have been

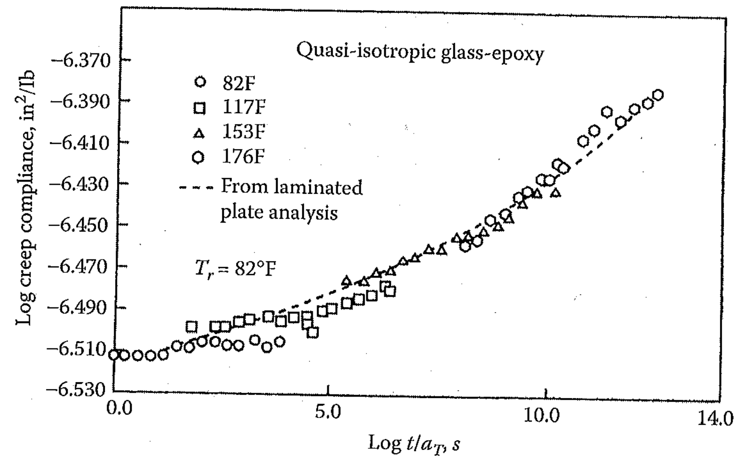

FIGURE 8.19
Predicted and measured creep compliance for a quasi-isotropic glass/epoxy laminate. (From Sims, D.F. and Halpin, J.C. 1974. *Composite Materials: Testing and Design [Third Conference]*, ASTM STP 546, pp. 46–66. American Society for Testing and Materials, Philadelphia, PA. Copyright ASTM. Reprinted with permission.)

met, micromechanics equations such as equation (3.23) can be modified for the case of sinusoidal oscillations as

$$E_1^*(\omega) = E_{f1}^*(\omega)\upsilon_f + E_m^*(\omega)\upsilon_m \tag{8.84}$$

where
$E_1^*(\omega)$ = longitudinal complex modulus of composite
$E_{f1}^*(\omega)$ = longitudinal complex modulus of fiber
$E_m^*(\omega)$ = complex modulus of isotropic matrix

By setting the real parts of both sides of equation (8.84) equal, we find the composite longitudinal storage modulus to be

$$E_1'(\omega) = E_{f1}'(\omega)\upsilon_f + E_m'(\omega)\upsilon_m \tag{8.85}$$

where
$E_1'(\omega)$ = longitudinal storage modulus of composite
$E_{f1}'(\omega)$ = longitudinal storage modulus of fiber
$E_m'(\omega)$ = storage modulus of isotropic matrix

Similarly, by setting the imaginary parts of both sides of equation (8.84) equal, we find that the composite longitudinal loss modulus is

$$E_1''(\omega) = E_{f1}''(\omega)\upsilon_f + E_m''(\omega)\upsilon_m \tag{8.86}$$

where
$E_1''(\omega)$ = longitudinal loss modulus of composite
$E_{f1}''(\omega)$ = longitudinal loss modulus of fiber
$E_m''(\omega)$ = loss modulus of isotropic matrix

The composite longitudinal loss factor is found by dividing equation (8.86) by equation (8.85):

$$\eta_1(\omega) = \frac{E_1''(\omega)}{E_1'(\omega)} = \frac{E_{f1}''(\omega)\upsilon_f + E_m''(\omega)\upsilon_m}{E_{f1}'(\omega)\upsilon_f + E_m'(\omega)\upsilon_m} \tag{8.87}$$

The complex forms of the other lamina properties can be determined in a similar fashion. In studies of the complex moduli of aligned discontinuous fiber composites, Suarez et al. [22] used the complex forms of equation (6.24), equation (3.41), and equation (3.59) to determine $E_1^*(\omega)$, $\nu_{12}^*(\omega)$, $E_2^*(\omega)$, and $G_{12}^*(\omega)$. These properties were then substituted into the complex form of equation (2.39) to obtain the off-axis complex modulus,

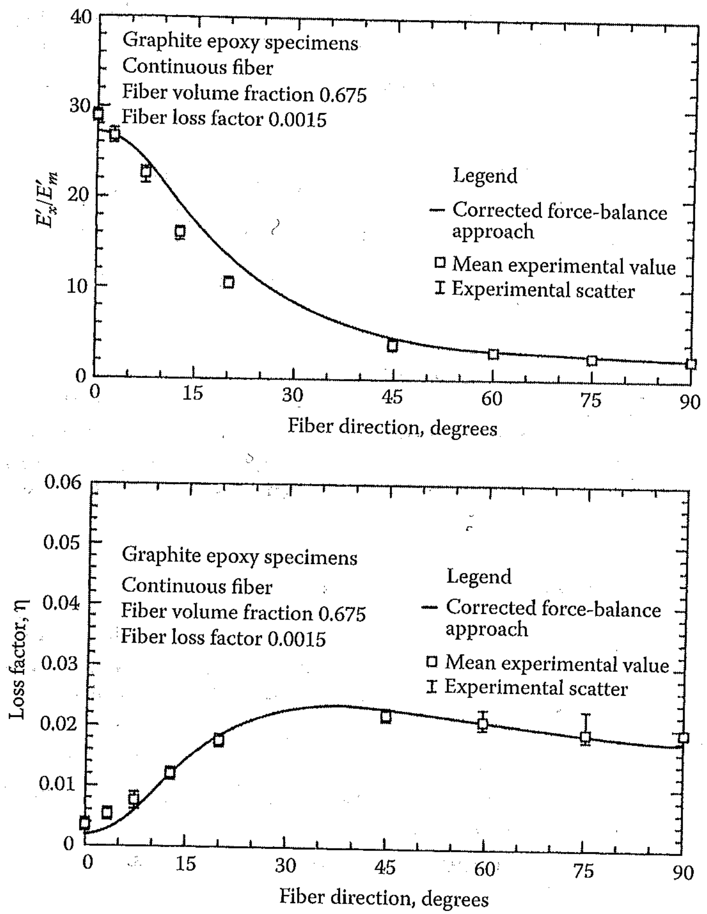

FIGURE 8.20
Predicted and measured off-axis storage modulus ratio, E_x'/E_m' and loss factor, η, of graphite/epoxy for various fiber orientations. (Suarez, S.A., Gibson, R.F., Sun, C.T., and Chaturvedi, S.K. 1986. *Experimental Mechanics*, 26(2), 175–184. With permission.)

$E_x^*(\omega)$. The predicted off-axis storage moduli and loss factors for various fiber orientations are compared with experimental data for a continuous fiber graphite/epoxy composite in figure 8.20, and the agreement is seen to be quite reasonable. Similar results were obtained for discontinuous fiber composites, but the fiber length effect is dominated by the fiber orientation effect, except for fiber orientations of $\theta \simeq 0°$. It is also interesting to note that there is an optimum fiber orientation for maximizing the loss factor. Thus damping is another design variable in composite structures.

For oscillatory loading of symmetric viscoelastic laminates, equations (7.58) can be rewritten, so that the sinusoidally varying strains are related to the sinusoidally varying loads by

$$\begin{Bmatrix} \tilde{\varepsilon}_x^0(t) \\ \tilde{\varepsilon}_y^0(t) \\ \tilde{\gamma}_{xy}^0(t) \end{Bmatrix} = \begin{bmatrix} A'_{11}{}^*(\omega) & A'_{12}{}^*(\omega) & A'_{16}{}^*(\omega) \\ A'_{12}{}^*(\omega) & A'_{22}{}^*(\omega) & A'_{26}{}^*(\omega) \\ A'_{16}{}^*(\omega) & A'_{26}{}^*(\omega) & A'_{66}{}^*(\omega) \end{bmatrix} \begin{Bmatrix} \tilde{N}_x(t) \\ \tilde{N}_y(t) \\ \tilde{N}_{xy}(t) \end{Bmatrix} \tag{8.88}$$

where the $A'_{ij}{}^*(\omega)$ are the laminate complex extensional compliances. The laminate stiffnesses can also be written in complex form (i.e., the $A^*_{ij}(\omega)$, $B^*_{ij}(\omega)$, and $D^*_{ij}(\omega)$), and the resulting equations have been used by Sun et al. [23] and others in studies of damping in laminates. Damping in composites will be discussed in more detail later in this chapter.

8.2.6 Temperature and Aging Effects

In the previous sections of this chapter the effects of temperature and aging on viscoelastic behavior have not been taken into account. We now consider these effects, as well as the corresponding methods of analysis. It is convenient to discuss first the effects of temperature. In section 8.2.2, a thermorheologically simple material was defined as having relaxation times, λ_i, and retardation times, ρ_i, which all have the same temperature dependence. Considering only the temperature dependence, the relaxation times at different temperatures can then be related by the equation

$$\lambda_i(T) = a_T \lambda_i(T_r) \tag{8.89}$$

where
$\lambda_i(T)$ = ith relaxation time at temperature T
$\lambda_i(T_r)$ = ith relaxation time at reference temperature, T_r
a_T = temperature-dependent shift factor

A similar equation can be used to express the temperature dependence of the retardation times. The effect of increasing temperature is to reduce the relaxation and retardation times and to speed up the relaxation and creep processes. This "speeding up" of the viscoelastic response can also be thought of as a process operating in "reduced time" [24]. For the purpose of illustration, we now consider the effect of the temperature-dependent relaxation times on the relaxation modulus by using the Zener

single-relaxation model in figure 8.10. The relaxation modulus at time t and temperature T is determined by modifying equation (8.44) as

$$C(t,T) = k_0 + k_1 e^{-t/\lambda_1(T)} \tag{8.90}$$

whereas the relaxation modulus at time t and reference temperature T_r is

$$C(t,T_r) = k_0 + k_1 e^{-t/\lambda_1(T_r)} \tag{8.91}$$

If we let the time at the reference temperature T_r be the "reduced time,"

$$\xi = t/a_T \tag{8.92}$$

then equation (8.91) becomes

$$C(\xi,T_r) = k_0 + k_1 e^{-t/a_T\lambda_1(T_r)} = k_0 + k_1 e^{-t/\lambda_1(T)} = C(t,T) \tag{8.93}$$

Thus, the effect of changing temperature on the relaxation modulus is the same as the effect of a corresponding change in the time scale, and this is the basis of the well-known Time-Temperature Superposition (TTS) principle, or the method of reduced variables [25].

One of the most useful applications of TTS is to extend the time range of short-term creep or relaxation test data by taking such data at various temperatures and then shifting the data along the time axis to form a "master curve" at a reference temperature, as shown in figure 8.21. However, the

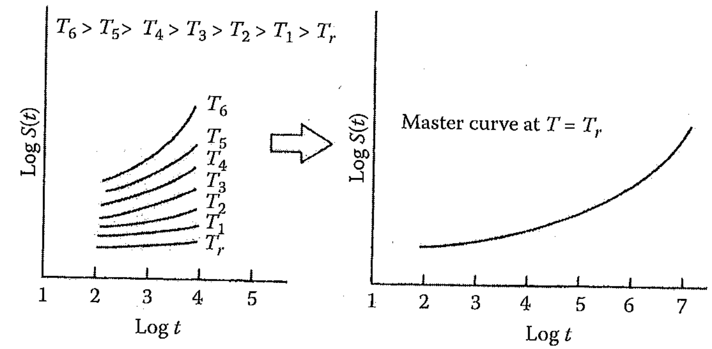

FIGURE 8.21
Shifting of creep data at various temperatures to generate a master curve at a reference temperature.

usefulness of the method depends on the ability to determine the shift factor, a_T. When the temperature, T, is greater than the glass transition temperature, T_g, the shift factor can be determined empirically with the well-known Williams–Landel–Ferry (WLF) equation [25]:

$$\log a_T = \frac{-c_1(T - T_r)}{-c_2(T - T_r)} \tag{8.94}$$

where c_1 and c_2 are material constants that must be determined from the experimental data. It has been found that when T_r is approximately 50°C above T_g, the values $c_1 = 8.86$ and $c_2 = 101.6$ are valid for a variety of polymers.

TTS has been successfully applied to many polymers at temperatures above T_g, but it is a different matter below the glass transition. Although TTS has been shown to be suitable for short-term creep or relaxation data at those temperatures, it does not produce valid results when applied to long-term test data. The reason is that a process called "physical aging" occurs in a polymer below T_g, and this aging process changes the viscoelastic response of the material during a long-term creep test. In a short-term test, because the test duration is much less than the aging time, no significant aging occurs during the test. Physical aging in polymers is associated with a slow loss of free volume that has been trapped in the polymer microstructure after quenching below T_g [26]. As shown in figure 8.22, as

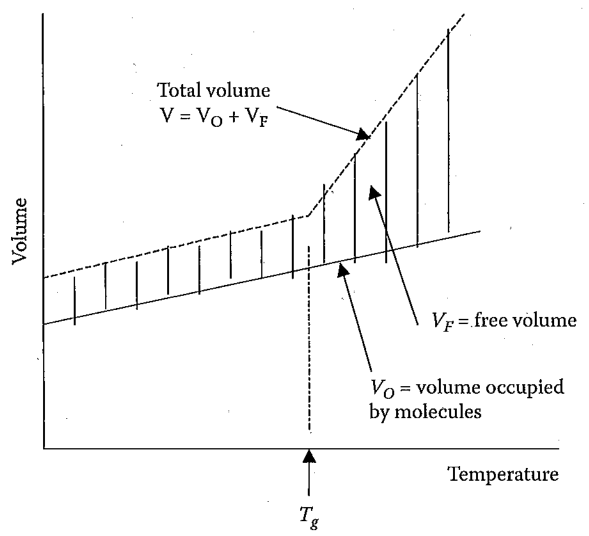

FIGURE 8.22
Polymer volume expansion with increasing temperature, showing how free volume increases sharply above the glass transition temperature.

the temperature of a polymer increases, its total volume consists of V_0, the volume occupied by the polymer molecules, and V_F, the so-called free volume between the molecules.

Below the glass transition temperature T_g, most of the total volume is occupied by the molecules, but as the temperature increases above T_g, V_F increases much faster than V_0. The polymer is usually processed in its molten form at temperatures above T_g; then when it is cooled or quenched to room temperature after molding, a significant amount of free volume is "locked in." This is a thermodynamically unstable condition, and as a result, the polymer will slowly give up free volume with time, to approach a more stable thermodynamic condition. As the polymer gives up free volume, the polymer chain mobility decreases and the relaxation times increase, thus reducing the speed of the relaxation or creep [7]. Pioneering work on aging of polymers has been done by Struik [26,27], and more recent work has been reported by Janas and McCullough [28] and Ogale and McCullough [29]. Still more recently, Sullivan [30] has shown that physical aging significantly affects the creep behavior of polymer matrix composites.

Since aging time, t_a, and temperature, T, both affect the relaxation times, Sullivan [30] has suggested that a new shift factor, $a(T,t_a)$, be defined by modifying equation (8.89) as

$$a = a(T, t_a) = \frac{\lambda_i(T, t_a)}{\lambda_i(T_r, t_{ar})} \tag{8.95}$$

where
$\lambda_i(T,t_a)$ = ith relaxation time at temperature T and aging time t_a
$\lambda_i(T_r,t_{ar})$ = ith relaxation time at reference temperature T_r and reference aging time t_{ar}

Struik [26] proposes that the TTS relationship for creep compliance be modified to include aging time effects by writing

$$S(t, T, t_a) = B(T)S(at, T_r, t_{ar}) \tag{8.96}$$

where
$B(t)$ = temperature-dependent vertical shift factor
$S(t,T,t_a)$ = creep compliance at time t, temperature T, and aging time t_a
$S(at,T_r,t_{ar})$ = creep compliance at shifted time at, reference temperature T_r, and reference aging time t_{ar}

Note that equation (8.96) is analogous to the TTS relationship for relaxation in equation (8.93)

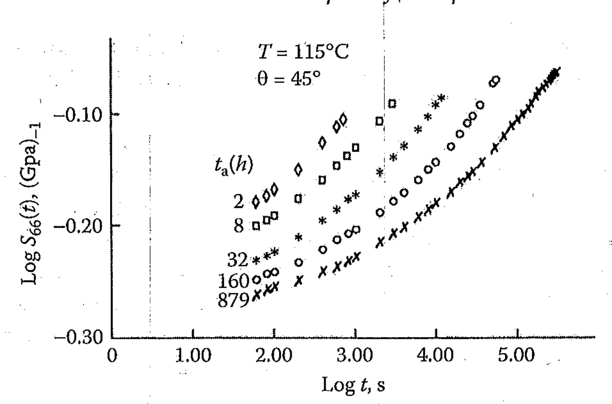

FIGURE 8.23
Effect of aging time, t_a, on shear creep compliance of 45° off-axis glass/vinyl ester composite at a test temperature of 115°C. (From Sullivan, J.L. 1990. *Composites Science and Technology*, 39, 207–232. Reprinted by permission of Elsevier Science Publishers, Ltd.)

can be written for relaxation. This new shift factor may be related to $\bar{a}_T$, the temperature shift factor below T_g, and a_{ta}, the shift factor for aging time, by the equation [30]

$$\log a = \log \bar{a}_r + \log a_{ta} \tag{8.97}$$

Figure 8.23 shows Sullivan's data on the effect of aging time on the shear creep compliance $S_{66}(t)$ of a glass/vinyl ester composite [30]. Clearly, the creep rate decreases with increased aging time, indicating an increase in the relaxation times and a slowing of the creep process. Support for the conclusion that TTS works well for short-term creep at constant age is provided by additional data from Sullivan [30] in figure 8.24 and figure 8.25. Figure 8.24 shows the short-term (or momentary) creep at various temperatures and "constant age," where the creep testing time is limited to no more than 10% of the aging time used in preconditioning the specimens. Figure 8.25 shows the corresponding momentary master curve at a reference temperature of 60°C. Both horizontal and vertical shifting of the momentary creep data were necessary to obtain the master curve [30]. The difference between long-term creep curves and the master curve from momentary creep data is shown in figure 8.26. Again, the conclusion is that aging slows down the creep process and that TTS does not work for long-term creep. Also shown in figure 8.26 are predicted long-term creep curves based on effective time theory [30], which is not discussed here.

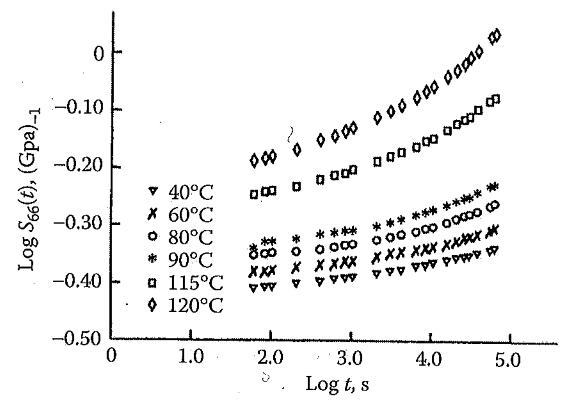

FIGURE 8.24
Momentary shear creep compliance data for glass/vinyl ester composite at various temperatures and constant aging time, t_a = 166 h. (From Sullivan, J.L. 1990. *Composites Science and Technology*, 39, 207–232. Reprinted by permission of Elsevier Science Publishers, Ltd.)

In conclusion, the reader is encouraged to refer to journal review articles for more information on various aspects of viscoelastic behavior of composites. For example, Schapery [1] has summarized the theoretical approaches to modeling of viscoelastic behavior of composites, and Scott et al. [31] have published a useful review of the technical literature on creep of fiber-reinforced composites.

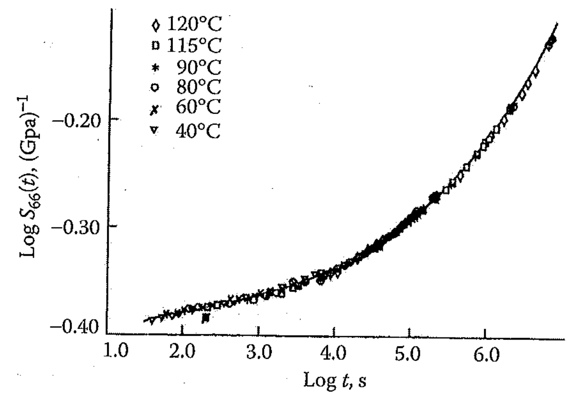

FIGURE 8.25
Momentary master curve for glass/vinyl ester composite at t_a = 166 h, T_r = 60°C, based on the test data from figure 8.24. (From Sullivan, J.L. 1990. *Composites Science and Technology*, 39, 207–232. Reprinted by permission of Elsevier Science Publishers, Ltd.)

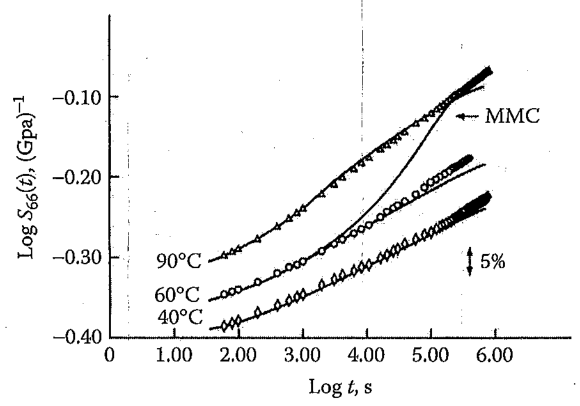

FIGURE 8.26
Long-term shear creep compliance and a momentary master curve for glass/vinyl ester composite, $t_a = 1$ h. Also shown are predicted curves from the effective time theory, which is not discussed here. (From Sullivan, J.L. 1990. *Composites Science and Technology*, 39, 207–232. Reprinted by permission of Elsevier Science Publishers, Ltd.)

EXAMPLE 8.5

The momentary master curve for the shear creep compliance, $S_{66}(t)$, of a unidirectional glass/vinyl ester composite at a reference temperature of 60°C and a reference aging time of 166 h is shown on a log–log scale in figure 8.25. (a) Neglecting aging effects, determine the time required to reach compliance of 0.63 (GPa)$^{-1}$ at a temperature of 60°C, and (b) neglecting vertical shifting, estimate the time required to reach the same compliance of 0.63 (GPa)$^{-1}$ at a temperature of 100°C. From experimental data, it is known that for this material, the WLF parameters are $c_1 = -1.01$ and $c_2 = -89.2$.

Solution. (a) From figure 8.25, at a value of log $S_{66}(t)$ = log(0.63) = 0.2, the corresponding value from the curve is log $t = 6$, and so $t = 10^6$ s at $T = 60$°C.

(b) From equation (8.96), we have

$$S_{66}(t, T, t_a) = B(T)S_{66}(at, T_r, t_{ar})$$

Since we are neglecting vertical shifting, $B(t) = 1$. Since the data are for a constant aging time, we have $a = a_T$ and equation (8.96) becomes

$$S_{66}(t, T) = S_{66}(at, T_r) = S_{66}(a_T t, T_r)$$

where the shift factor, a_T, is found from the WLF equation

$$\log a_T = \frac{-c_1(T - T_r)}{c_2 + (T - T_r)} = \frac{-(-1.01)(100 - 60)}{-89.2 + (100 - 60)} = -0.8211$$

or $a_T = 0.151$, which means that $a_T t = 0.151(10^6) = 1.51 \times 10^5$ s. Thus, the creep compliance curve at 100°C is shifted to the left of the curve at the reference temperature of 60°C, and it takes only 15% as much time to reach the compliance of 0.63 (GPa)$^{-1}$ at 100°C as it does at 60°C.

8.3 Dynamic Behavior of Composites

In this section, the basic concepts of dynamic behavior of composites will be introduced by discussing wave propagation, vibration, and damping of specially orthotropic composites without coupling. Only 1-D wave propagation without dispersion, reflection, or refraction will be considered, as 3-D wave propagation, wave dispersion, and reflection/refraction effects are beyond the scope of this book. For detailed discussions of these topics, the reader is referred to publications by Christensen [4], Hearmon [32], Achenbach [33], Ross and Sierakowski [34], and Moon [35]. Longitudinal vibrations of composite bars and flexural vibrations of composite beams and plates without coupling will also be considered. Vibrations of laminates with coupling and laminated plate boundary conditions other than the simply supported ones will not be considered. These topics are discussed in detail in books by Whitney [36], Vinson and Sierakowski [37], and Sierakowski and Chaturvedi [38]. The use of the Elastic–Viscoelastic Correspondence Principle and a strain energy method to analyze damping in composites will also be discussed.

The basic premise of all analyses presented in this section is that the criteria for valid use of the effective modulus theory have been met. That is, the scale of the inhomogeneity, d, is assumed to be much smaller than the characteristic structural dimension, L, and the characteristic wavelength of the dynamic stress distribution, λ ($d \ll L$ and $d \ll \lambda$ in figure 8.6). Thus, all heterogeneous composite material properties are assumed to be effective properties of equivalent homogeneous materials. If the wavelength is not long in comparison with the scale of the inhomogeneity in the material, the wave shape is distorted as it travels through the material, and this is referred to as dispersion. Dispersion in composites has been discussed in several previous publications [4,33,35,38].

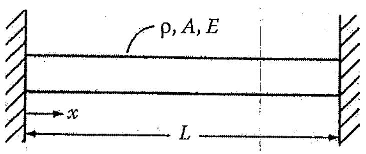

FIGURE 8.27
Bar of density ρ, cross-sectional area A, and length L, fixed on both ends.

8.3.1 Longitudinal Wave Propagation and Vibrations in Specially Orthotropic Composite Bars

As will be shown in any book on vibrations [39], longitudinal wave propagation and vibration in a homogeneous, isotropic, linear elastic bar (fig. 8.27) are governed by the 1-D wave equation

$$\frac{\partial}{\partial x}\left(AE\frac{\partial u}{\partial x}\right)=\rho A\frac{\partial^2 u}{\partial t^2} \tag{8.98}$$

where
- x = distance from end of bar
- t = time
- $u = u(x,t)$ is the longitudinal displacement of a cross-section in the bar at a distance x and time t
- $A = A(x)$ is the cross-sectional area of bar
- ρ = mass density of bar
- $E = E(x)$ is the modulus of elasticity of bar

It is assumed that the displacement $u(x,t)$ is uniform across a given cross-section. Using effective modulus theory for a heterogeneous, specially orthotropic, linear elastic composite bar, we simply replace the properties ρ and E with the corresponding effective properties of an equivalent homogeneous material. The effective modulus E then depends on the orientation of fibers relative to the axis of the bar. For fibers oriented along the x direction, $E = E_1$; for fibers oriented along the transverse direction, $E = E_2$; and for a specially orthotropic laminate, we use the effective laminate engineering constant $E = E_x$. For laminates with coupling, the analysis is much more difficult, as shown in Section 8.3.3. If the area and the modulus are not functions of position, equation (8.98) reduces to

$$c_2\frac{\partial^2 u}{\partial x^2}=\frac{\partial^2 u}{\partial t^2} \tag{8.99}$$

where $c = (E/\rho)^{1/2}$ is the wave speed.

The most common solutions to the 1-D wave equation are of the d'Alembert type or the separation of variables type. The d'Alembert solution is of the form

$$u(x,t)=p(x+ct)+q(x-ct) \tag{8.100}$$

The function $p(x+ct)$ represents a wave traveling to the left with velocity c. That is, a point located at $\xi = x + ct$ moves to the left with velocity c if ξ is a constant, since $x = \xi - ct$. Similarly, $q(x - ct)$ represents a wave traveling to the right with velocity c. For a sine wave, we have

$$u(x,t)=A\sin\frac{2\pi}{\lambda}(x+ct)+A\sin\frac{2\pi}{\lambda}(x-ct) \tag{8.101}$$

where λ is the wavelength. Note that this is the wavelength that must be greater than the scale of the inhomogeneity, d, in order for the effective modulus theory to be valid. Alternatively, we can write equation (8.101) as

$$u(x,t)=A\sin(2\pi kx+\omega t)+A\sin(2\pi kx-\omega t) \tag{8.102}$$

where
- $k = 1/\lambda$ is the number of waves per unit distance
- $\omega = 2\pi c/\lambda$ is the frequency of wave

Using trigonometric identities, we find that

$$u(x,t)=2A\sin 2\pi kx\cos\omega t \tag{8.103}$$

which represents a standing wave of profile $2A \sin 2\pi kx$, which oscillates with frequency ω. Generally, the combined wave motion in opposite directions is caused by reflections from the boundaries. Thus, wave propagation without reflection will not lead to a standing wave (or vibration).

A separation of variables solution is found by letting

$$u(x,t)=U(x)F(t) \tag{8.104}$$

where $U(x)$ is a function of x alone and $F(t)$ is a function of t alone. Substituting this solution in equation (8.99) and separating variables, we obtain

$$c^2\frac{1}{U}\frac{d^2U}{dx^2}=\frac{1}{F}\frac{d^2F}{dt^2} \tag{8.105}$$

The left-hand side of equation (8.105) is a function of x alone and the right-hand side is a function of t alone; therefore, each side must be equal to a constant. If we let this constant be, say, $-\omega^2$, then equation (8.105) gives the two ordinary differential equations,

$$\frac{d^2F}{dt^2}+\omega^2 F=0 \tag{8.106a}$$

$$\frac{d^2U}{dx^2}+\left(\frac{\omega}{c}\right)^2 U=0 \tag{8.106b}$$

and the solutions to these equations are of the form,

$$F(t)=A_1\sin\omega t+B_1\cos\omega t \tag{8.107}$$

$$U(x)=A_2\sin\left(\frac{\omega}{c}\right)x+B_2\cos\left(\frac{\omega}{c}\right)x \tag{8.108}$$

where A_1 and B_1 depend on the initial conditions, and A_2 and B_2 depend on the boundary conditions. For a bar that is fixed at both ends (fig. 8.27), the substitution of the boundary conditions $u(0,t)=u(L,t)=0$ leads to the conclusion that $B_2=0$ and

$$\sin\left(\frac{\omega}{c}\right)L=0 \tag{8.109}$$

Equation (8.109) is the eigenvalue equation, which has an infinite number of solutions, ω_n, such that

$$\frac{\omega_n L}{c}=n\pi \tag{8.110}$$

where

n = mode number = 1,2,3, …, ∞
ω_n = eigenvalues, or natural frequencies (rad/s) = $2\pi f_n$
f_n = natural frequencies (Hz)

Thus,

$$f_n=\frac{nc}{2L}=\frac{n}{2L}\left(\frac{E}{\rho}\right)^{1/2} \tag{8.111}$$

For the nth mode of vibration, the displacements are then

$$u_n(x,t)=(A'\sin\omega_n t+B'\cos\omega_n t)\sin\left(\frac{n\pi x}{L}\right) \tag{8.112}$$

where $A'=A_1A_2$ and $B'=B_1A_2$. The mode shape for the nth mode is given by the eigenfunction

$$U_n(x)=\sin\left(\frac{n\pi x}{L}\right) \tag{8.113}$$

and the general solution is the superposition of all modal responses

$$u(x,t)=\sum_{n=1}^{\infty}(A'\sin\omega_n t+B'\cos\omega_n t)\sin\left(\frac{n\pi x}{L}\right) \tag{8.114}$$

Mode shapes, natural frequencies, and wavelengths for the first three modes of the fixed-fixed bar are shown in figure 8.28. The most important

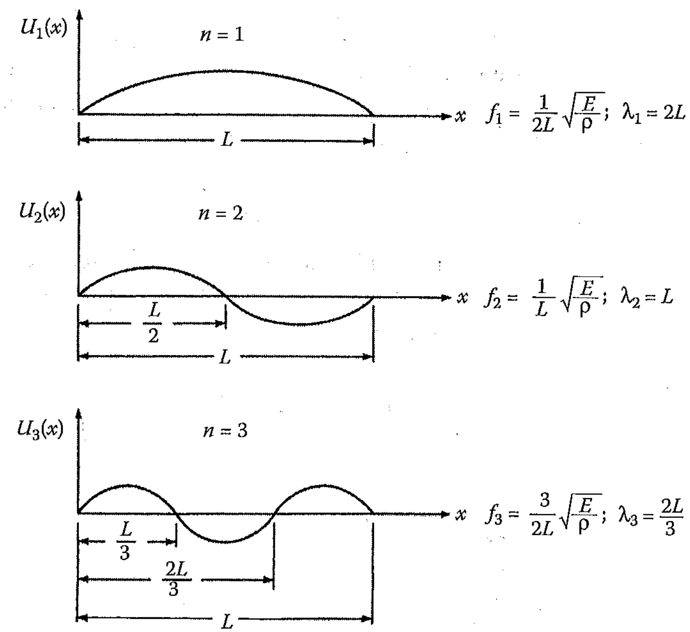

FIGURE 8.28
Mode shapes, natural frequencies, and wavelengths for the first three modes of longitudinal vibration of a bar with both ends fixed (fig. 8.27).

point here is that as the mode number increases, the wavelength decreases and the use of effective modulus theory becomes more questionable. In general, the wavelengths associated with typical mechanical vibration frequencies of structures in the audio frequency range will satisfy the criteria $d \ll \lambda$. The wavelengths associated with ultrasonic wave propagation may be short enough to cause concern about the use of effective modulus theory, however.

The equations developed in this section are instructive not only from the point of view of the limitations of effective modulus theory, but for material characterization as well. The two basic approaches to measurement of dynamic mechanical properties of materials involve the use of either wave propagation experiments or vibration experiments. Assuming that the criteria for the use of effective modulus theory have been met, the effective modulus of a specially orthotropic composite can be determined by measuring the longitudinal wave speed, c, in a specimen of density, ρ, and then solving for $E = c^2\rho$. Alternatively, the nth mode natural frequency, f_n, can be measured in a vibration experiment, and the effective modulus can be found from an equation such as equation (8.111). Dynamic mechanical testing of composites will be discussed in more detail in chapter 10.

Finally, the equations presented here can be modified for linear viscoelastic composites in sinusoidal vibration by using the Elastic Viscoelastic Correspondence Principle. This means that the effective modulus E will be replaced by the complex modulus $E^*(\omega)$. Alternatively, the stress–strain relationship used in deriving the equation of motion could be an equation of the form shown in equation (8.28) or a special case of that equation.

8.3.2 Flexural Vibration of Composite Beams

Transverse, or flexural, motion of a homogeneous, isotropic, linear elastic beam (fig. 8.29) without shear or rotary inertia effects is described by the well-known Bernoulli–Euler equation

$$-\frac{\partial^2}{\partial x^2}\left(EI\frac{\partial^2 w}{\partial x^2}\right) = \rho A\frac{\partial^2 w}{\partial t^2} \tag{8.115}$$

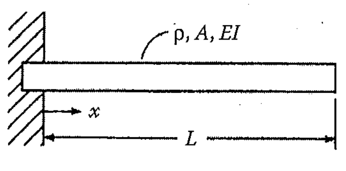

FIGURE 8.29
Cantilever beam for the Bernoulli–Euler beam theory.

where

I = area moment of inertia of cross-section about the centroidal axis of beam
$w = w(x,t)$ is the transverse displacement of the centroidal axis of beam
x, t, ρ, A, and E are as defined in equation (8.98)

If the beam is such that EI is constant along the length, equation (8.115) reduces to

$$EI\left(\frac{\partial^4 w}{\partial x^4}\right) + \rho A\frac{\partial^2 w}{\partial t^2} = 0 \tag{8.116}$$

Assuming that the criteria for the use of effective modulus theory have been met, these equations can be used for specially orthotropic composites or laminates without coupling if the modulus E is replaced by the effective flexural modulus E_f. Recall that, depending on the laminate configuration, E_f may be found from equations such as equation (7.8), equation (7.9), equation (7.68), or equation (7.69). For laminates with coupling, the equations of motion based on the Classical Lamination Theory will be developed in the next section.

As an example of a solution of the Bernoulli–Euler equation, consider a separation of variables solution for harmonic free vibration:

$$w(x,t) = W(x)e^{i\omega t} \tag{8.117}$$

where ω is the frequency and $W(x)$ the mode shape function. Substituting this solution in equation (8.116) yields

$$\frac{d^4W(x)}{dx^4} - k^4 W(x) = 0 \tag{8.118}$$

where $k = (\omega^2\rho A/EI)^{1/4}$. The solution for equation (8.118) is of the form

$$W(x) = C_1\sin kx + C_2\cos kx + C_3\sinh kx + C_4\cosh kx \tag{8.119}$$

where the constants C_1, C_2, C_3, and C_4 depend on the boundary conditions. For example, for a cantilever beam (fig. 8.29), the four boundary conditions yield the following relationships:

$W(x) = 0$ when $x = 0$; therefore, $C_2 = -C_4$

$\frac{dW(x)}{dx} = 0$ when $w = 0$; therefore, $C_1 = -C_3$

$\frac{d^2W(x)}{dx^2} = 0$ when $x = L$

Therefore, $C_1(\sin kL + \sinh kL) + C_2(\cos kL + \cosh kL) = 0$.

$$\frac{d^3W(x)}{dx^3} = 0 \quad \text{when } x = L$$

Therefore, $C_1(\cos kL + \cosh kL) + c_2(\sin kL - \sinh kL) = 0$.

For nontrivial solutions C_1 and C_2 in the last two equations, the determinant of the coefficients must be equal to zero and

$$\cos kL \cosh kL + 1 = 0 \tag{8.120}$$

This is the eigenvalue equation for the cantilever beam, which has an infinite number of solutions, k_nL. The subscript n refers to the mode number. The eigenvalues for the first three modes are

$$k_1L = 1.875, \qquad k_2L = 4.694, \qquad k_3L = 7.855 \tag{8.121}$$

Substituting the eigenvalues in the definition of k (see eq. [8.118] rearranging), and using the relationship $\omega = 2\pi f$, we have the frequency equation

$$f_n = \frac{(k_nL)^2}{2\pi L^2}\left(\frac{EI}{\rho A}\right)^{1/2} \tag{8.122}$$

The mode shape function for the nth mode is then

$$W_n(x) = C_2[\cos k_nx - \cosh k_nx + \sigma_n(\sin k_nx - \sinh k_nx)] \tag{8.123}$$

where

$$\sigma_n = \frac{\sin k_nL - \sinh k_nL}{\cos k_nL + \cosh k_nL}$$

The mode shapes and frequencies for the first three modes of the cantilever beam are shown in figure 8.30. The effect of increasing the mode number and the corresponding reduction in wavelength is again apparent.

If transverse shear and rotary inertia effects are included in the derivation of the equation of motion for transverse vibration of a beam, the result is the well-known Timoshenko beam equation [40]:

$$EI\left(\frac{\partial^4 w}{\partial x^4}\right) + \rho A\frac{\partial^2 w}{\partial t^2} + \frac{J\rho}{FG}\frac{\partial^4 w}{\partial t^4} - \left(J + \frac{EI\rho}{FG}\right)\frac{\partial^4 w}{\partial x^2 \partial t^2} = 0 \tag{8.124}$$

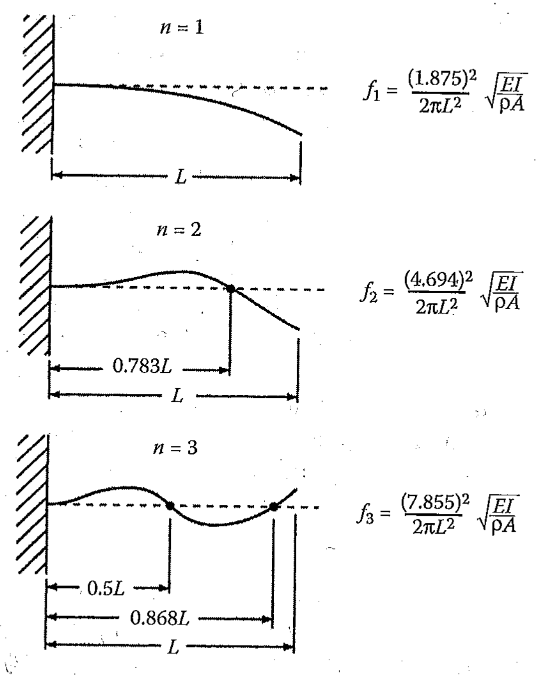

FIGURE 8.30
Mode shapes and natural frequencies for the first three modes of flexural vibration of the cantilever beam in figure 8.29.

where

J = rotary inertia per unit length
F = shape factor for cross-section
G = shear modulus

This equation can also be used for specially orthotropic composites and laminates without coupling by replacing E and G with the effective flexural modulus, E_f, and the effective through-the-thickness shear modulus, respectively, for the composite. For example, for a unidirectional, transversely isotropic composite with the fibers along the beam axis, the appropriate shear modulus to use is $G = G_{13} = G_{12}$. If the fibers are oriented in the transverse direction, $G = G_{23}$. Both shear and rotary inertia effects become more important as the mode number increases, and both effects reduce the natural frequencies below the Bernoulli–Euler values. The beam length-to-thickness ratio, L/h, is an important factor in the determination of the shear effect, with decreasing L/h generating increased shear effects. It appears that for highly anisotropic composite beams, shear effects may be significant unless L/h is greater than about 100 [41].

The transverse shear effect is also strongly dependent on the ratio E/G, which is much greater for composite beams than for isotropic beams. For a typical isotropic metal $E/G \simeq 2.6$, but for composites such as unidirectional carbon/epoxy, $E_1/G_{12} \simeq 20$ or higher. Sandwich beams with foam or honeycomb cores have even higher E/G ratios due to the low shear stiffness of the core and are very susceptible to transverse shear effects.

As in the previous section, the equations developed here can be used in dynamic mechanical testing to determine the effective moduli of a composite specimen. The equations can also be converted to linear viscoelastic form by replacing the elastic moduli with the corresponding complex moduli, or by deriving the equation of motion from a viscoelastic stress–strain relationship. More sophisticated analytical models for vibrating composite beams, including various effects such as viscoelastic behavior, transverse shear, and bending-twisting coupling, have been developed [36–38,42–44], but these are beyond the scope of this book.

EXAMPLE 8.6

For a symmetric laminated beam having a rectangular cross-section of width b and thickness h, determine (a) the equation of motion for free vibration and (b) the natural frequencies. Assume that the criteria for use of the effective modulus theory have been met.

Solution. (a) Substituting the flexural modulus, E_{fx}, from equation (7.68) in the expression for EI, we find that

$$EI = E_{fx}I = \frac{12}{h^3 D'_{11}}\frac{bh^3}{12} = \frac{b}{D'_{11}}$$

(Note that h is used to denote thickness here since t is used for time.) Thus, the Bernoulli–Euler beam equation (eq. [8.111]) becomes

$$\frac{b}{D'_{11}}\frac{\partial^4 w}{\partial x^4} + \rho A\frac{\partial^2 w}{\partial x^2} = 0$$

(b) The natural frequencies are then found from equation (8.122):

$$f_n = \frac{(k_n L)^2}{2\pi L^2}\left(\frac{b}{D'_{11}\rho A}\right)^{1/2}$$

where the eigenvalues, k_n, depend on the boundary conditions.

8.3.3 Transverse Vibration of Laminated Plates

Although the equations for vibration of composite beams in the previous section are useful, they are limited to laminates without coupling. The more general equations of motion for transverse vibration of a laminated plate can be derived by modifying the static equilibrium equations that were developed for the analysis of static deflections of laminated plates in section 7.9. For example, according to Newton's second law, equation (7.119) must now be modified, so that the summation of forces along the x direction in figure 7.40 is given by

$$N_x dy + \frac{\partial N_x}{\partial x}dx dy + N_{xy}dx + \frac{\partial N_{xy}}{\partial y}dx dy - N_x dy - N_{xy}dx = \rho_0 dx dy\frac{\partial^2 u^0}{\partial t^2} \tag{8.125}$$

where

ρ_0 = mass per unit area of laminate (equal to ρh)
ρ = mass density of laminate is the mass per unit volume
h = thickness of laminate (since t is used for time here)
$u^0 = u^0(x,y,t)$ is the middle surface displacement in the x direction

Equation (8.125) may be simplified as

$$\frac{\partial N_x}{\partial x} + \frac{\partial N_{xy}}{\partial y} = \rho_0\frac{\partial^2 u^0}{\partial t^2} \tag{8.126}$$

Similarly, the summation of forces along the y direction yields

$$N_x dx + \frac{\partial N_x}{\partial y}dx\,dy + N_{xy}dy + \frac{\partial N_{xy}}{\partial x}dx\,dy - N_y dx - N_{xy}dy = \rho_0 dx\,dy\frac{\partial^2 \upsilon^0}{\partial t^2} \tag{8.127}$$

or

$$\frac{\partial N_y}{\partial y} + \frac{\partial N_{xy}}{\partial x} = \rho_0\frac{\partial^2 \upsilon^0}{\partial t^2} \tag{8.128}$$

where $\upsilon^0 = \upsilon^0(x,y,t)$ is the middle surface displacement in the y direction. The summation of forces along the z direction gives

$$Q_x dy + \frac{\partial Q_x}{\partial x}dx\,dy + Q_y\,dx + \frac{\partial Q_y}{\partial_y}dx\,dy - Q_x\,dy - Q_y\,dx + q(x,y) = \rho_0\frac{\partial^2 w}{\partial t^2}$$

(8.129)

or

$$\frac{\partial Q_x}{\partial x}+\frac{\partial Q_y}{\partial y}+q(x,y)=\rho_0\frac{\partial^2 w}{\partial t^2} \tag{8.130}$$

where $w = w(x,y,t)$ is the displacement in the z direction.

For moment equilibrium we consider the moments about the x-axis and the y-axis while neglecting rotary inertia. Thus, the summation of moments about the x-axis gives

$$\begin{aligned}&-M_y dx-\frac{\partial M_y}{\partial y}dy\,dx-M_{xy}dy-\frac{\partial M_{xy}}{\partial x}dx\,dy+Q_y dx\,dy\\&+\frac{\partial Q_y}{\partial y}dy\,dx\,dy+q(x,y)dx\,dy\,dy/2+Q_x\,dy\,dy/2\\&+\frac{\partial Q_x}{\partial x}dx\,dy\,dy/2+M_y dx+M_{xy}dy-Q_x dy\,dy/2=0\end{aligned} \tag{8.131}$$

Simplifying and neglecting products of differentials, we get

$$\frac{\partial M_y}{\partial y}+\frac{\partial M_{xy}}{\partial x}=Q_y \tag{8.132}$$

A similar summation of moments about the y-axis gives

$$\frac{\partial M_x}{\partial x}+\frac{\partial M_{xy}}{\partial y}=Q_x \tag{8.133}$$

Substitution of equation (8.132) and equation (8.133) in equation (8.130) yields

$$\frac{\partial^2 M_x}{\partial x^2}+2\frac{\partial^2 M_{xy}}{\partial x\,\partial y}+\frac{\partial^2 M_y}{\partial y^2}+q(x,y)=\rho_0\frac{\partial^2 w_x}{\partial t^2} \tag{8.134}$$

Equation (8.126), equation (8.128), and equation (8.134) are differential equations of motion of the plate in terms of stress and moment resultants. The corresponding equations of motion in terms of displacements can be derived by substituting the laminate force–deformation equations (7.41), the strain–displacement relations (7.29), and the curvature–displacement

equations (7.30) in equation (8.126), equation (8.130), and equation (8.134). The resulting equations are

$$\begin{aligned}&A_{11}\frac{\partial^2 u^0}{\partial x^2}+2A_{16}\frac{\partial^2 u^0}{\partial x\,\partial y}+A_{66}\frac{\partial^2 u^0}{\partial y^2}+\frac{\partial^2 \upsilon^0}{\partial x^2}+(A_{12}+A_{66})\frac{\partial^2 \upsilon^0}{\partial x\,\partial y}+A_{26}\frac{\partial^2 \upsilon^0}{\partial y^2}\\&-B_{11}\frac{\partial^3 w}{\partial x^3}-3B_{16}\frac{\partial^3 w}{\partial x^2\partial y}-(B_{12}+2B_{66})\frac{\partial^3 w}{\partial x\,\partial y^2}-B_{26}\frac{\partial^3 w}{\partial y^3}=\rho_0\frac{\partial^2 u^0}{\partial t^2}\end{aligned} \tag{8.135}$$

$$\begin{aligned}&A_{16}\frac{\partial^2 u^0}{\partial x^2}+(A_{12}+A_{66})\frac{\partial^2 u^0}{\partial x\,\partial y}+A_{26}\frac{\partial^2 u^0}{\partial y^2}+A_{66}\frac{\partial^2 \upsilon^0}{\partial x^2}+2A_{26}\frac{\partial^2 \upsilon^0}{\partial x\,\partial y}+A_{22}\frac{\partial^2 \upsilon^0}{\partial y^2}\\&-B_{16}\frac{\partial^3 w}{\partial x^3}-(B_{12}+2B_{66})\frac{\partial^3 w}{\partial x^2\partial y}-3B_{26}\frac{\partial^3 w}{\partial x\,\partial y^2}-B_{22}\frac{\partial^3 w}{\partial y^3}=\rho_0\frac{\partial^3 \upsilon^0}{\partial t^2}\end{aligned} \tag{8.136}$$

$$\begin{aligned}&D_{11}\frac{\partial^4 w}{\partial x^4}+4D_{16}\frac{\partial^4 w}{\partial x^3\,\partial y}+2(D_{12}+2D_{66})\frac{\partial^4 w}{\partial x^2\,\partial y^2}+4D_{26}\frac{\partial^4 w}{\partial x\,\partial y^3}+D_{22}\frac{\partial^4 w}{\partial y^4}\\&-B_{11}\frac{\partial^3 u^0}{\partial x^3}-3B_{16}\frac{\partial^3 u^0}{\partial x^2\,\partial y}-(B_{12}+2B_{66})\frac{\partial^3 u^0}{\partial x\,\partial y^2}-B_{26}\frac{\partial^3 u^0}{\partial y^3}-B_{16}\frac{\partial^3 \upsilon^0}{\partial x^3}\\&+(B_{12}+2B_{66})\frac{\partial^3 \upsilon^0}{\partial x^2\,\partial y}-3B_{26}\frac{\partial^3 \upsilon^0}{\partial x\,\partial y^2}-B_{22}\frac{\partial^3 \upsilon^0}{\partial y^3}+\rho_0\frac{\partial^2 w}{\partial t^2}=q(x,y)\end{aligned} \tag{8.137}$$

As with the static case in section 7.9, the in-plane displacements u^0 and υ^0 are coupled with the transverse displacements w when the B_{ij} are present. For symmetric laminates with $B_{ij} = 0$, equation (8.137) alone becomes the governing equation for transverse displacements. These governing partial differential equations must be solved subject to the appropriate boundary conditions. As in the static case, when the in-plane displacements are coupled with the transverse displacements, the boundary conditions must be a combination of boundary conditions for a planar theory of elasticity problem and boundary conditions for a plate-bending problem. In this section we will only discuss transverse vibrations according to equation (8.137) with all $B_{ij} = 0$ and the transverse distributed load $q(x,y) = 0$. An example of coupling effects will be given in example 8.8.

Let us now consider the case of free transverse vibration of the rectangular, specially orthotropic plate that is simply supported on all edges, as

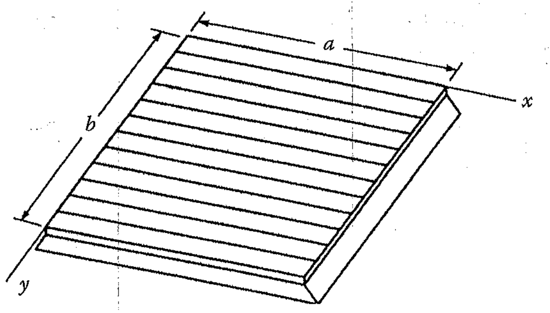

FIGURE 8.31
Simply supported, specially orthotropic plate for free transverse vibration analysis.

shown in figure 8.31. The discussion here follows the analysis of Whitney [36]. For a specially orthotropic plate, all $B_{ij} = 0$, $A_{16} = A_{26} = D_{16} = D_{26} = 0$ and equation (8.137) becomes

$$D_{11}\frac{\partial^4 w}{\partial x^4} + 2(D_{12} + 2D_{66})\frac{\partial^4 w}{\partial x^2 \partial y^2} + D_{22}\frac{\partial^4 w}{\partial y^4} + \rho_0 \frac{\partial^2 w}{\partial t^2} = 0 \qquad (8.138)$$

For free harmonic vibration at frequency ω, we can assume that

$$w(x, y, t) = W(x, y)e^{i\omega t} \qquad (8.139)$$

where $W(x,y)$ is a mode shape function. Substituting equation (8.139) in equation (8.138), we have

$$D_{11}\frac{\partial^4 W}{\partial x^4} + 2(D_{12} + 2D_{66})\frac{\partial^4 W}{\partial x^2 \partial y^2} + D_{22}\frac{\partial^4 W}{\partial y^4} - \rho_0\omega^2 W = 0 \qquad (8.140)$$

For the simply supported boundary condition, the transverse displacements and bending moments must vanish at the edges as in the static case. Thus, from equation (7.135) and equation (7.136), we have, again, along $x = 0$ and $x = a$,

$$W(x, y) = 0$$

and

$$M_x = -D_{11}\frac{\partial^2 W}{\partial x^2} - D_{12}\frac{\partial^2 W}{\partial y^2} = 0 \qquad (8.141)$$

and along $y = 0$ and $y = b$,

$$W(x, y) = 0$$

and

$$M_y = -D_{12}\frac{\partial^2 W}{\partial x^2} - D_{22}\frac{\partial^2 W}{\partial y^2} = 0 \qquad (8.142)$$

It can be shown that the equation of motion and the boundary conditions are satisfied by solutions of the form

$$W(x, y) = A_{mn}\sin\left(\frac{m\pi x}{a}\right)\sin\left(\frac{n\pi y}{b}\right) \qquad (8.143)$$

where m and n are mode indices that refer to the number of half wavelengths along the x and y directions, respectively, for mode mn, and a and b are the plate dimensions along the x and y directions, respectively. Substitution of equation (8.143) in equation (8.140) yields the frequency equation:

$$\omega_{mn}^2 = \frac{\pi^4}{\rho_0 a^4}\left[D_{11}m^4 + 2(D_{12} + 2D_{66})(mnR)^2 + D_{22}(nR)^4\right] \qquad (8.144)$$

where the plate aspect ratio $R = a/b$, and ω_{mn} is the natural frequency for mode mn [36]. For the fundamental mode, where $m = n = 1$, the natural frequency is given by

$$\omega_{11}^2 = \frac{\pi^4}{\rho_0}\left[\frac{D_{11}}{a^4} + \frac{(2D_{12} + 2D_{66})}{a^2 b^2} + \frac{D_{22}}{b^4}\right] \qquad (8.145)$$

and the mode shape function is given by

$$W(x, y) = \sin\left(\frac{\pi x}{a}\right)\sin\left(\frac{\pi y}{b}\right) \qquad (8.146)$$

We now consider numerical results given by Whitney [36] for frequencies and mode shapes of two square plates. One plate is orthotropic with

TABLE 8.2

Predicted Natural Frequencies for the First Four Modes of Simply Supported Plates Made of Specially Orthotropic and Isotropic Materials

	Orthotropic, $\omega = k\pi^2/b^2\sqrt{D_{22}/\rho_0}$			Isotropic, $\omega = k\pi^2/b^2\sqrt{D/\rho_0}$		
Mode	m	n	k	m	n	k
1st	1	1	3.62	1	1	2.0
2nd	1	2	5.68	1	2	5.0
3rd	1	3	10.45	2	1	5.0
4th	2	1	13.0	2	2	8.0

Source: From Whitney, J.M. 1987. *Structural Analysis of Laminated Anisotropic Plates.* Technomic Publishing Co., Lancaster, PA. With permission.

$D_{11}/D_{22} = 10$ and $(D_{12} + 2D_{66})/D_{22} = 1$; the other is isotropic with $D_{11}/D_{22} = 1$ and $(D_{12} + 2D_{66})/D_{22} = 1$. The four lowest natural frequencies for the two plates are compared in table 8.2 and the corresponding mode shapes are compared in figure 8.32. The dotted lines in figure 8.32 denote the nodal lines of zero displacement for a particular mode. It is interesting to

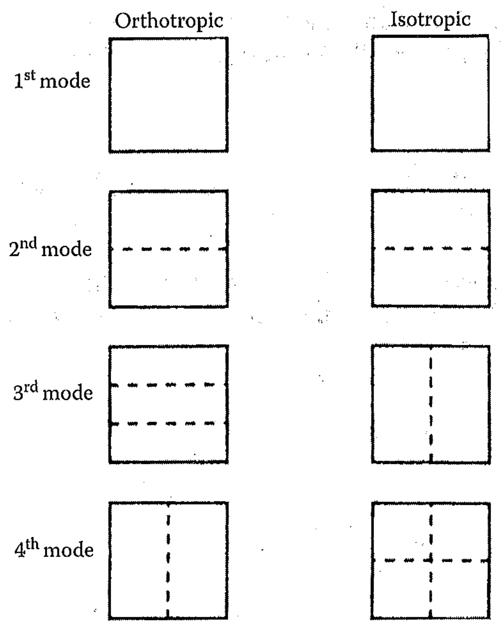

FIGURE 8.32
Mode shapes for the first four modes of simply supported plates mode of specially orthotropic and isotropic materials. (From Whitney, J.M. 1987. *Structural Analysis of Laminated Anisotropic Plates.* Technomic Publishing Co., Lancaster, PA. With permission.)

note that, in order of increasing frequency, the sequence of mode numbers is different for the isotropic and orthotropic plates. Due to the high stiffness of the orthotropic plate along the x direction, its frequencies are higher than the corresponding isotropic plate frequencies. It is also interesting to note that for the isotropic plate $\omega_{12} = \omega_{21}$, but for the orthotropic plate $\omega_{21} > \omega_{12}$.

As with the static case, it is generally not possible to find exact mode shape functions similar to those given by equation (8.143) for boundary conditions such as clamped edges or free edges. For such cases, approximate solutions must be derived using approaches such as the Rayleigh–Ritz method or the Galerkin method. For more detailed discussions of these methods, the reader is referred to books by Whitney [36] and Vinson and Sierakowski [37].

The equation of motion for a specially orthotropic, laminated beam is found by reducing equation (8.138) to the 1-D form

$$D_{11}\frac{\partial^4 w}{\partial x^4} + \rho_o\frac{\partial^2 w}{\partial t^2} = 0 \tag{8.147}$$

If we substitute $\rho_o = \rho h$, and if we multiply equation (8.147) by the beam width, b, we have

$$bD_{11}\frac{\partial^4 w}{\partial x^4} + \rho bh\frac{\partial^2 w}{\partial t^2} = 0 \tag{8.148}$$

For the 1-D case, $D_{11} = 1/D'_{11}$, and since $bh = A$, we have

$$\frac{b}{D'_{11}}\frac{\partial^4 w}{\partial x^4} + \rho A\frac{\partial^2 w}{\partial t^2} = 0 \tag{8.149}$$

which is the same as the equation that was derived from the beam theory earlier in example 8.6.

EXAMPLE 8.7

A unidirectional AS/3501 carbon/epoxy plate is simply supported on all four edges. The plate is 300 mm × 300 mm square, 2 mm thick, and has a mass density of 1.6 mg/mm³. Determine the frequency of the fundamental mode of the plate.

Solution. Using the lamina stiffnesses, Q_{ij}, from example 7.3 and the thickness of 2 mm in equations (7.40) for a laminate consisting of a single orthotropic lamina, we find the laminate bending stiffnesses to be

$D_{11} = 92.53$ GPa-mm³, $D_{12} = 1.813$ GPa-mm³
$D_{22} = 6.03$ GPa-mm³, $D_{66} = 4.6$ GPa-mm³

The mass per unit area is

$$\rho_0 = \rho h = (1.6\ \text{mg/mm}^3)(2\ \text{mm}) = 3.2\ \text{mg/mm}^2 = 0.0032\ \text{g/mm}^2$$

The fundamental frequency is then found from equation (8.145) as

$$\omega_{11}^2 = \frac{\pi^4}{(0.0032)(300)^4}[92.53 + 2(1.813 + 2(4.6)) + 6.03](10^9) = 4.53(10^5)\text{rad}^2/\text{s}^2$$

or

$$\omega_{11} = 673\ \text{rad/s}$$

(*Note:* GPa-mm³ = 10⁹ g-mm²/s² in the above equation.)

EXAMPLE 8.8

Investigate the effects of coupling on the flexural vibration frequencies of a nonsymmetrically laminated [0/90] crossply composite beam that is simply supported on each end. The beam has length L and the x-axis is parallel to the longitudinal axis of the beam.

Solution. Since the plies are all oriented at either 0° or 90°, there is no shear coupling, and $A_{16} = A_{26} = B_{16} = B_{26} = D_{16} = D_{26} = 0$. In addition, for a 1-D beam oriented along the x direction, all terms in the equations of motion (eq. [8.135], eq. [8.136], and eq. [8.137]) involving v^0 and y, and derivatives in y may be neglected. Finally, we will neglect the longitudinal inertia term on the right-hand side of equation (8.135), and the transverse loading term $q(x,y)$ on the right-hand side of equation (8.137). With these simplifications, equation (8.136) becomes identically zero on both sides, while equation (8.135) and equation (8.137) reduce to the coupled partial differential equations, respectively,

$$A_{11}\frac{\partial^2 u^0}{\partial x^2} - B_{11}\frac{\partial^3 w}{\partial x^3} = 0$$

and

$$D_{11}\frac{\partial^4 w}{\partial x^4} - B_{11}\frac{\partial^3 u^0}{\partial x^3} = -\rho_0\frac{\partial^2 w}{\partial t^2}$$

For free harmonic vibration at frequency, ω, we can assume separation of variables solutions of the form

$$u^0(x,t) = U(x)e^{i\omega t}$$

and

$$w(x,t) = W(x)e^{i\omega t}$$

where $U(x)$, $W(x)$ are mode shape functions. Substitution of these assumed shape functions in the two equations of motion above yields the ordinary differential equations

$$A_{11}\frac{d^2U}{dx^2} - B_{11}\frac{d^3W}{dx^3} = 0$$

and

$$D_{11}\frac{d^4W}{dx^4} - B_{11}\frac{d^3U}{dx^3} = \rho_0\omega^2 W$$

For the simple supports at $x = 0$ and $x = L$, the boundary conditions are given by specifying that the transverse displacement $W(x)$ and the bending moment per unit length $M_x(x)$ must both vanish at $x = 0$ and $x = L$. Therefore

$$W(0) = 0$$

$$W(L) = 0$$

$$M_x(0) = B_{11}\frac{dU}{dx}(0) - D_{11}\frac{d^2W}{dx^2}(0) = 0$$

$$M_x(L) = B_{11}\frac{dU}{dx}(L) - D_{11}\frac{d^2W}{dx^2}(L) = 0$$

where the equations for the bending moment per unit length, $M_x(x)$, are found by substituting the simplifications listed above in equation (7.29), equation (7.30), and equation (7.41), and evaluating the resulting expressions at $x = 0$ and $x = L$. It can be shown by substitution that the boundary conditions are all satisfied by mode shape functions of the form

$$U(x) = U_0\cos\left(\frac{n\pi x}{L}\right)$$

$$W(x) = W_0\sin\left(\frac{n\pi x}{L}\right)$$

where $n = 1, 2, 3, \ldots$, is the mode number. It can also be shown that these functions satisfy the in-plane boundary conditions $N_x(0) = N_x(L) = N_{xy}(0) = N_{xy}(L) = 0$.

Substitution of these mode shape functions in the two differential equations yields the algebraic equations,

$$\begin{bmatrix} A_{11}\left(\frac{n\pi}{L}\right)^2 & -B_{11}\left(\frac{n\pi}{L}\right)^3 \\ -B_{11}\left(\frac{n\pi}{L}\right)^3 & D_{11}\left(\frac{n\pi}{L}\right)^4 - \rho_0\omega_n^2 \end{bmatrix} \begin{Bmatrix} U_0 \\ W_0 \end{Bmatrix} = \begin{Bmatrix} 0 \\ 0 \end{Bmatrix}$$

where $\omega = \omega_n$ for vibration in mode n. For nontrivial solutions of the displacements, the determinant of the coefficient matrix must be equal to zero, and this yields the frequency equation for mode n:

$$\omega_n^2 = \frac{1}{\rho_0}\left(\frac{n\pi}{L}\right)^4\left(D_{11} - \frac{B_{11}^2}{A_{11}}\right)$$

It is easily shown from the definitions of the laminate stiffnesses that for this [0/90] laminate, A_{11}, B_{11}^2, and D_{11} are all positive, and that as a result, the bending–extension coupling term B_{11}^2/A_{11} causes the frequencies to be reduced below those of a symmetrically laminated beam that has the nth mode frequency,

$$\omega_n^2 = \left(\frac{n\pi}{L}\right)^4 \frac{D_{11}}{\rho_0}$$

Similarly, Jones [45] has shown that, for antisymmetric crossply laminated plates of various aspect ratios and various numbers of plies, bending–extension coupling always reduces the frequencies. However, it was found that the frequency reduction is greatest for the case of only two plies (i.e., [0/90]), and that the coupling effect was reduced as the number of plies was increased. Similar results have been found for antisymmetric angle-ply laminates.

8.3.4 Analysis of Damping in Composites

Damping is simply the dissipation of energy during dynamic deformation. As structures and machines are pushed to higher and higher levels of precision and performance, and as the control of noise and vibration becomes more of a societal concern, it is becoming essential to take damping into account in the design process. In conventional metallic structures, it is commonly accepted that much of the damping comes from friction in structural joints or from add-on surface damping treatments because the damping in the metal itself is typically very low. On the other hand, polymer composites have generated increased interest in the development of highly damped, lightweight, structural composites because of their

good damping characteristics and the inherent design flexibility, which allows trade-offs between such properties as damping and stiffness. The purpose of this section is to give a brief overview of the analysis of linear viscoelastic damping in composites. Dynamic mechanical testing of composites, which includes experimental determination of damping, will be discussed in chapter 10. More detailed treatments of damping in composites are given in publications by Gibson [46–48], Bert [49], Adams [50], Chaturvedi [51], Kinra and Wolfenden [52], and Sun and Lu [53].

As described in section 8.1, damping is one of the important physical manifestations of viscoelastic behavior in dynamically loaded structural materials, and the stress–strain hysteresis loop in figure 8.1(c) is typical of damped response under cyclic loading. Viscoelastic behavior of fiber and/or matrix materials is not the only mechanism for structural damping in composite materials although it does appear to be the dominant mechanism in undamaged polymer composites vibrating at small amplitudes. Other damping mechanisms include thermoelastic damping due to cyclic heat flow, coulomb friction due to slip in unbonded regions of the fiber/matrix interface, and energy dissipation at sites of cracks and/or delaminations [46]. Thermoelastic damping is generally more important for metal composites than for polymer composites. Damping due to poor interface bonding, cracks, and/or delaminations cannot be relied upon in the design of structures, but the measurement of such damping may be the basis of a valuable nondestructive evaluation methodology [47].

In order to understand linear viscoelastic damping better, it is important to recognize the relationship between the time scale of the applied deformation and the internal time scale of the material. The time scale for cyclic deformation is determined by the oscillation frequency, ω. Recall that the relaxation times, λ_i, or retardation times, ρ_i, are measures of the internal time scale of the material. We will now use the Zener single relaxation model to illustrate how damping depends on the relationship between these two time scales.

For sinusoidal oscillation of the Zener single relaxation model (fig. 8.10[a]), we can write

$$\sigma = \sigma_0 e^{i\omega t} = (E' + iE'')\varepsilon \tag{8.150}$$

where
σ = stress
σ_0 = stress amplitude
ε = strain
ω = frequency
E' = storage modulus is $E'(\omega)$
E'' = loss modulus is $E''(\omega)$
i = imaginary operator, which is $(-1)^{1/2}$

Substituting equation (8.150) in the stress–strain relationship for the Zener model (eq. [8.42]) and separating into real and imaginary parts, we find that

$$E' = E'(\omega) = \frac{k_0 + (k_0 + k_1)\omega^2\lambda_1^2}{1+\omega^2\lambda_1^2} \tag{8.151}$$

$$E'' = E''(\omega) = \frac{\omega\lambda_1 k_1}{1+\omega^2\lambda_1^2} \tag{8.152}$$

and

$$\eta = \eta(\omega) = \frac{E''(\omega)}{E'(\omega)} = \frac{\omega\lambda_1 k_1}{k_0 + (k_0 + k_1)\omega^2\lambda_1^2} \tag{8.153}$$

where

$\lambda_1 = \mu_1/k_1$ is the relaxation time from equation (8.44)

$\eta = (\omega)$ is the loss factor

The variations of E' and E'' with frequency ω are shown schematically in figure 8.33. Note that when the frequency is the reciprocal of the relaxation time, $\omega = 1/\lambda_1$, the loss modulus peaks and the storage modulus passes through a transition region. Such damping peaks in the frequency domain are often referred to as "relaxation peaks." The loss factor has a

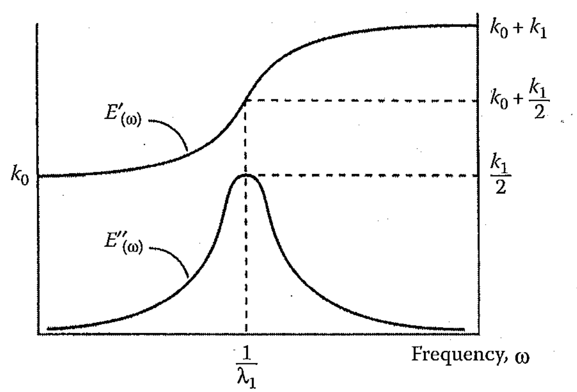

FIGURE 8.33
Variation of storage modulus, $E'(\omega)$, and loss modulus, $E''(\omega)$, with frequency for the Zener single relaxation model.

peak at a different frequency, not shown in figure 8.33 because the relative position of that peak depends on the numerical values of the parameters. But the important point is that the dissipation of energy, whether characterized by the loss modulus or the loss factor, is maximized when the time scale of the deformation is the same as the internal time scale of the material. If the two time scales are substantially different, the energy dissipation is reduced. For example, notice in figure 8.33 that $E'' \to 0$ as $\omega \to 0$ and as $\omega \to \infty$. This behavior is typical for viscoelastic materials, but, as mentioned earlier, the actual transitions occur over a wider range (in this case a wider frequency range) than the single relaxation model produces. Thus, as before, an improved Zener model (fig. 8.12 or fig. 8.14) with a distribution of relaxation times makes it possible to extend the range of the relaxation to approximate the actual behavior better.

Analytical models have been developed for predicting damping in composites at both the micromechanical and macromechanical levels. Only in certain special cases, such as thermoelastic damping [54] or dislocation damping [55] in metals, can the damping be predicted from first principles without knowledge of constituent material damping properties. (These damping mechanisms will not be discussed here.) If the damping mechanism is of the linear viscoelastic type, there are two basic approaches to the development of analytical models, both of which are based on the existence of experimental damping data for constituent materials. The two approaches are as follows:

The use of the Elastic–Viscoelastic Correspondence Principle in combination with elastic solutions from the mechanics of materials or the elasticity theory

The use of a strain energy formulation that relates the total damping in the structure to the damping of each element and the fraction of the total strain energy stored in that element

The basis of the first approach is that linear elastostatic analyses can be converted to vibratory linear viscoelastic analyses by replacing static stresses and strains with the corresponding vibratory stresses and strains, and by replacing the elastic moduli or compliances with the corresponding complex moduli or compliances, respectively. According to this procedure, the elastostatic stress–strain relationships in equations (2.5) would be converted to the viscoelastic vibratory equations (8.70), and equations (2.3) would be converted to equations (8.71), as described in section 8.2.5. The use of this approach to derive the micromechanics equation for the longitudinal loss factor of a unidirectional composite (eq. [8.87]) has already been demonstrated. The same approach has been used to derive micromechanics equations for the prediction of damping in aligned discontinuous fiber composites having various fiber aspect ratios and fiber orientations [22,56] in randomly oriented short fiber composites [57], in metal matrix and ceramic matrix composites at elevated temperatures [58], in hybrid composites with coated fibers [59], and in woven fiber-reinforced composites [60].

The correspondence principle has also been used in combination with the Classical Lamination Theory to develop equations for the laminate loss factors [23]. For example, the extensional loss factors for a laminate can be expressed in terms of the real and imaginary parts of the corresponding laminate extensional stiffnesses:

$$\eta_{ij}^{(A)} = \frac{A''_{ij}}{A'_{ij}} \tag{8.154}$$

Similar equations can be used to describe laminate coupling and flexural loss factors [23]. The major limitation of such analyses is that the Classical Lamination Theory neglects interlaminar stresses, so that interlaminar damping is not included. As shown later in this section, a more general 3-D analysis including interlaminar damping may be developed by using a strain energy method.

Although sinusoidally varying stresses and strains were assumed in the development of the complex modulus notation in section 8.2.4, it has been shown that as long as the stiffness and damping show some frequency dependence, the complex modulus notation is also valid for the more general nonsinusoidal case [61]. Anomalous analytical results such as noncausal response can occur if the components of the complex modulus are independent of frequency. Composite materials (particularly polymer composites) generally have frequency-dependent complex moduli, however.

The second approach involves the use of a strain–energy relationship that was first presented in 1962 by Ungar and Kerwin [62]. Ungar and Kerwin found that for an arbitrary system of linear viscoelastic elements, the system loss factor can be expressed as a summation of the products of the individual element loss factors and the fraction of the total strain energy stored in each element:

$$\eta = \frac{\sum_{i=1}^{n} \eta_i W_i}{\sum_{i=1}^{n} W_i} \tag{8.155}$$

where

η_i = loss factor for the ith element in system
W_i = strain energy stored in the ith element at maximum vibratory displacement
n = total number of elements in system

When applying this equation to composite damping analysis, the composite becomes the "system," and the nature of the elements depends on whether the analysis is micromechanical or macromechanical. For example, this equation has been used in combination with mechanics of materials solutions for the strain energy of aligned discontinuous fiber composites [63]. In this analysis, the damping in the fiber was neglected (i.e., the fiber loss factor $\eta_f = 0$), so that the longitudinal loss factor of the aligned discontinuous fiber composite was approximated by the following form of equation (8.155):

$$\eta_1 = \frac{\eta_m W_m}{w_f + W_m} \tag{8.156}$$

where

η_m = matrix loss factor
W_m = strain energy in matrix at maximum vibratory displacement
W_f = strain energy in fiber at maximum vibratory displacement

The strain energy terms W_f and W_m were determined from mechanics of materials by using the stress distributions from the Cox model (eq. [6.21] and eq. [6.26]). The longitudinal storage modulus, E'_1, was also determined from the Cox model (eq. [6.24]), and the loss modulus was found from $E''_1/E'_1\eta_1$. Figure 8.34 shows the variation of the predicted ratio E''_1/E''_m

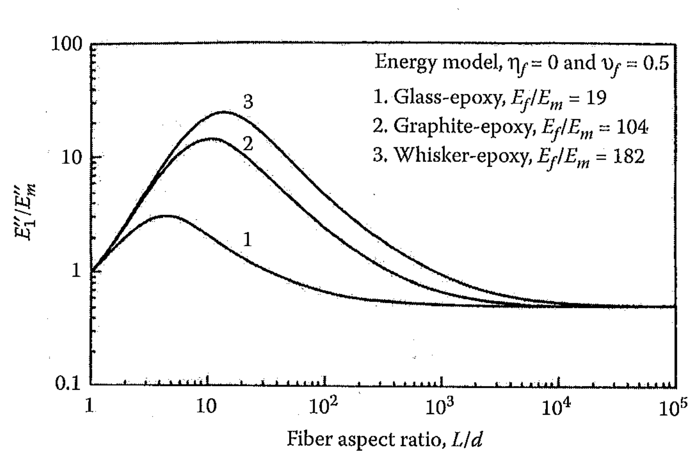

FIGURE 8.34
Variation of loss modulus ratio, E''_1/E''_m, with fiber aspect ratio, L/d, for several aligned discontinuous fiber composite systems. (From Gibson, R.F., Chaturvedi, S.K., and Sun, C.T. 1982. *Journal of Materials Science*, 17, 3499–3509. Reprinted by permission of Chapman & Hall.)

with fiber length-to-diameter ratio, L/d, for several fiber/matrix combinations [63]. It is seen that each composite has an optimum L/d where the ratio E_1''/E_m'' is maximized, and that both the peak value of E_1''/E_m'' and the optimum L/d shift to higher values as the modulus ratio E_f/E_m increases. This means that the damping, which is primarily due to interfacial shear deformation, is increased when the mismatch between the fiber and the matrix stiffnesses (as determined by E_f/E_m) is increased.

The Ungar–Kerwin equation is ideally suited for finite element implementation in the analysis of complex structures. In the finite element implementation, the element index "i" in equation (8.155) refers to the element number, n refers to the total number of finite elements, and the strain energy terms, W_i, are determined from the finite element analysis. It appears that the equation was first implemented in finite element form in the so-called "modal strain energy" approach for the analysis of modal damping in complex structures [64]. The strain energy/finite element approach has also been used in numerous composite analysis applications at both the micromechanical level [59,60,65,66] and the laminate level [67–69]. For example, in studies of the fiber/matrix interphase, the finite element models shown in figure 8.35 were used in conjunction with the equation

$$\eta = \frac{\eta_f W_f + \eta_m W_m + \eta_i W_i}{W_f + W_m + W_i} \tag{8.157}$$

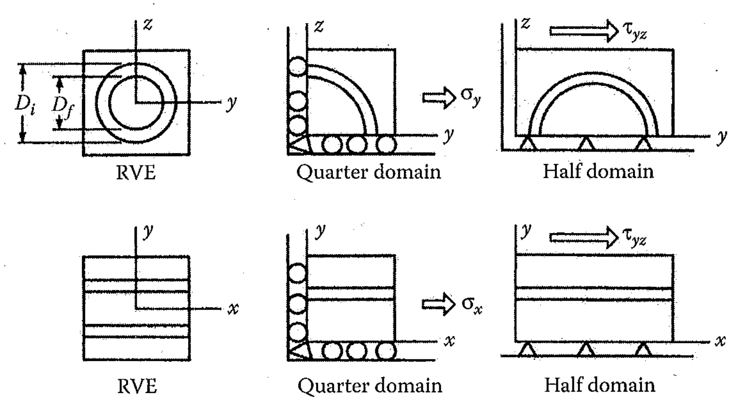

FIGURE 8.35
Models used for strain energy/finite element analysis of effect of interphase on damping or unidirectional graphite/epoxy under different loading conditions. (From Gibson, R.F., Hwang, S.J., and Kwak, H. 1991. *How Concept Becomes Reality — Proceedings of 36th International SAMPE Symposium*, vol. 1, pp. 592–606. Reprinted by permission of the Society for the Advancement of Material and Process Engineering, Covina, CA.)

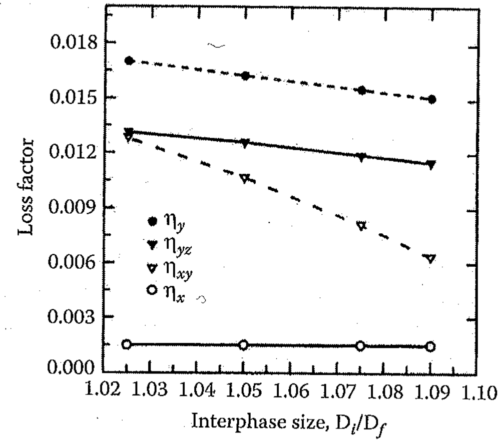

FIGURE 8.36
Predicted effect of interphase size on loss factor for material and loading conditions described in figure 8.35 (From Gibson, R.F., Hwang, S.J., and Kwak, H. 1991. *How Concept Becomes Reality — Proceedings of 36th International SAMPE Symposium*, vol. 1, pp. 592–606. Reprinted by permission of the Society for the Advancement of Material and Process Engineering, Covina, CA.)

where
η_f = fiber loss factor
η_i = interphase loss factor
W_i = strain energy in interphase region at maximum vibratory displacement

Typical results for four different loading conditions are shown in figure 8.36. It appears that the in-plane shear loss factor, η_{xy}, is the most sensitive of the four loss factors to the size of the interphase region.

Three-dimensional finite element analysis has been used in conjunction with the Ungar–Kerwin equation to study interlaminar damping and the effects of coupling on damping in laminates [67–69]. In these studies, the laminate loss factor was modeled using the equation

$$\eta = \sum_{k=1}^{N} \left[\eta_x^{(k)} W_x^{(k)} + \eta_y^{(k)} W_y^{(k)} + \eta_{xy}^{(k)} W_{xy}^{(k)} + \eta_z^{(k)} W_z^{(k)} + \eta_{yz}^{(k)} W_{yz}^{(k)} + \eta_{xz}^{(k)} W_{xz}^{(k)} \right] / W_t \tag{8.158}$$

where
k = lamina number
N = total number of laminae

W_t = total strain energy stored in laminate at maximum vibratory displacement:

$$W_t = \sum_{k=1}^{N} \left[W_x^{(k)} + W_y^{(k)} + W_{xy}^{(k)} + W_z^{(k)} + W_{yz}^{(k)} + W_{xz}^{(k)} \right]$$

x, y, z = global laminate coordinates
$\eta_x^{(k)}, \eta_y^{(k)}, \eta_{xy}^{(k)}$ = in-plane loss factors for the kth lamina
$\eta_z^{(k)}, \eta_{yz}^{(k)}, \eta_{xz}^{(k)}$ = out-of-plane loss factors for the kth lamina
$W_x^{(k)}, W_y^{(k)}, W_{xy}^{(k)}$ = in-plane strain energy terms for the kth lamina
$W_z^{(k)}, W_{yz}^{(k)}, W_{xz}^{(k)}$ = out-of-plane strain energy terms for the kth lamina

Thus, the decomposition of the total damping into contributions associated with each stress component is a relatively simple task with the strain energy approach. For example, figure 8.37 shows the contribution of the different components of interlaminar damping as a function of fiber orientation for angle-ply graphite laminates under uniaxial extension [67]. The finite element model for this work was shown in figure 7.26. It is seen that the interlaminar damping is maximized at a particular fiber orientation, and that the interlaminar shear stress, τ_{yz}, is the most significant contributor to interlaminar damping in this case. A similar approach was used to study damping in composite beams with constrained viscoelastic layer damping treatments, and figure 8.38 shows the effect of constrained viscoelastic layer (damping tape) length on damping for a glass/epoxy beam [70]. In this case, damping is seen to be strongly dependent on the ratio of damping tape length to beam length and the tape end fixity condition.

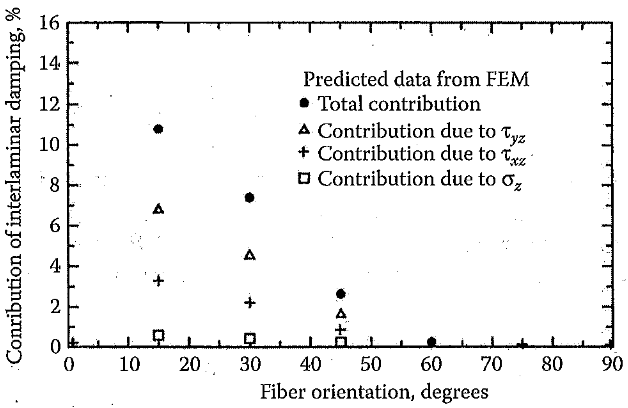

FIGURE 8.37
Contribution of different components of interlaminar damping for various fiber orientations for $[\pm\theta]_s$ graphite/epoxy laminates (with laminate width/thickness = 4 and length/thickness = 6) under uniaxial loading. (From Hwang, S.J. and Gibson, R.F. 1991. *Composites Science and Technology*, 41, 379–393. Reprinted by permission of Elsevier Science Publishers, Ltd.)

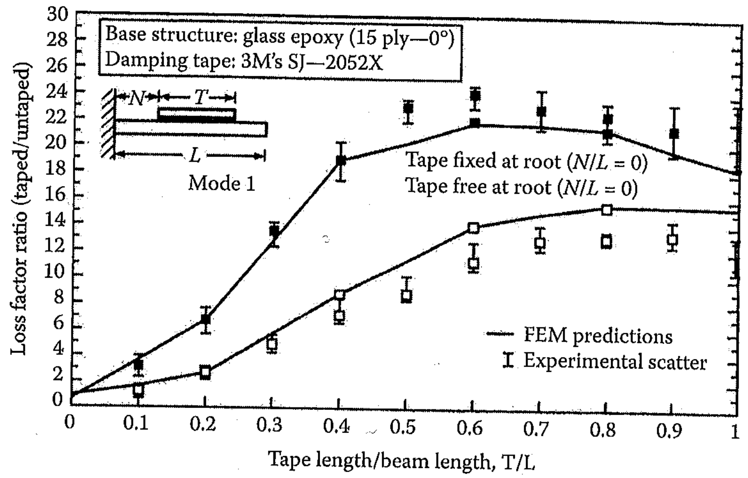

FIGURE 8.38
Measured and predicted damping for unidirectional glass/epoxy beam with constrained viscoelastic layer damping tapes of different lengths and tape end fixity conditions. (From Mantena, P.R., Gibson, R.F., and Hwang, S.J. 1991. *AIAA Journal*, 29(10), 1678–1685. Copyright AIAA, 1990. With permission.)

A review of the applications of the strain energy method for studying various aspects of damping in composite materials and structures has been published by Hwang and Gibson [71]. At the structural level, this method has been used to predict damping in composite grid structures [72], curvilinear laminates and composite shell structures [73], and composite sandwich structures [74]. For example, Chen and Gibson [72] used a finite element implementation of the strain energy approach to study integral passive damping in composite isogrid structures. Figure 8.39 shows a typical 3-D finite element model for the composite isogrid structure, which has an integral layer of polymeric damping material at the rib/skin interface. Figure 8.40 shows that the predicted and measured damping can be increased significantly by using the integral damping layer. Further discussion of the experimental aspects of this work can be found in chapter 10.

Although the loss factor is a convenient measure of damping because of its connection with the complex modulus notation, it is not the only parameter used to describe damping. For materials with small damping

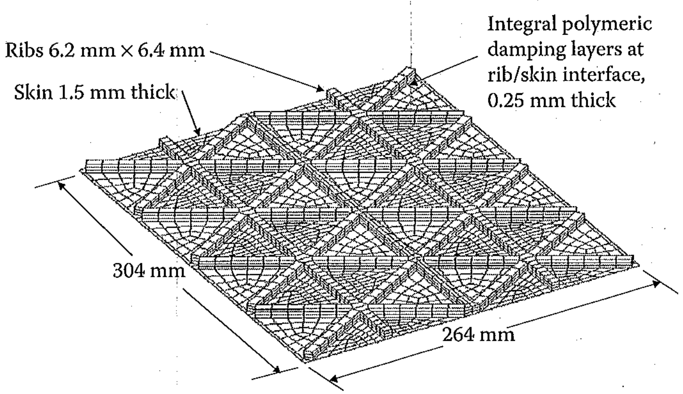

FIGURE 8.39
Finite element model for analysis of vibration and damping in composite isogrid structure with integral passive damping. From Chen, Y., and Gibson, R.F. 2003. *Mechanics of Advanced Materials and Structures*, 10(2), 127–143.

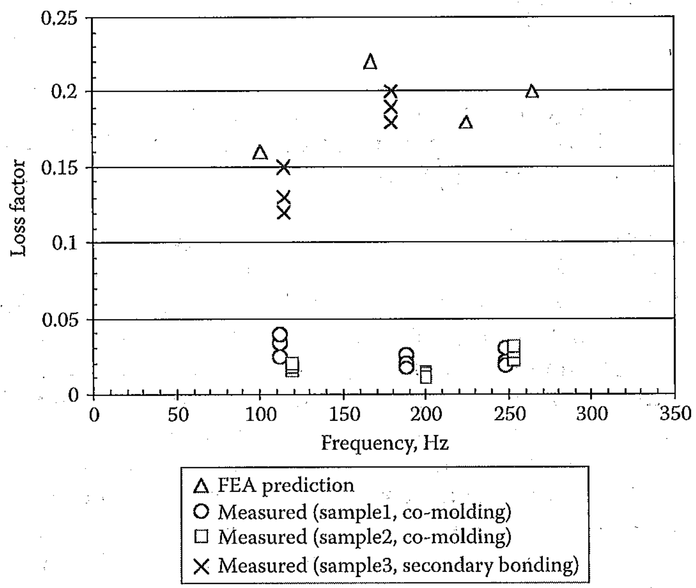

FIGURE 8.40
Comparison of predicted and measured damping loss factors in composite isogrid structures with and without integral passive damping. From Chen, Y., and Gibson, R.F. 2003. *Mechanics of Advanced Materials and Structures*, 10(2), 127–143.

($\eta \ll 1$), other measures of damping that appear in the literature are related to the loss factor as follows [49]:

$$\eta = \frac{\psi}{2\pi} = \frac{\Delta}{\pi} = 2\zeta = \frac{1}{Q} \tag{8.159}$$

where

Ψ = specific damping capacity
Δ = logarithmic decrement
ζ = damping ratio, or damping factor
Q = quality factor

Most of these parameters are associated with the damping of a single degree of freedom vibration model and are used to obtain damping from vibration test data. Such tests will be discussed in more detail in chapter 10.

Finally, as part of the nanotechnology revolution, the study of vibration and damping in nanocomposites has been the subject of numerous investigations in recent years, with many investigators reporting on improvement of damping in composites when nanotubes or nanoparticles are added to the polymer matrix materials. A review of the literature on vibrations of carbon nanotubes and their composites has been published by Gibson et al. [75]. Most of the studies of damping in nanocomposites so far have been of an experimental nature, and there is a need for more analytical work. Experimental work on vibration and damping of nanocomposites will be discussed in more detail in chapter 10.

In summary, damping has become an important consideration in the design of dynamically loaded composite materials and structures. As a result, there is increased interest in the prediction of damping in composites. Several analytical methods for making such predictions have been reviewed, and sample results have been presented. Because of the design flexibility that is inherent in composite materials, the potential for improvement and optimization of damping appears to be much greater than that for conventional structural materials.

EXAMPLE 8.9
The constituent materials in a unidirectional graphite/epoxy material have the following dynamic mechanical properties at a certain frequency, :

$$E'_{f1} = 220 \text{ GPa } (32\times10^6 \text{ psi}); \quad \eta_{f1} = 0.002; \quad \upsilon_f = 0.6$$

$$E'_m = 3.45 \text{ GPa } (0.5\times10^6 \text{ psi}); \quad \eta_m = 0.02; \quad \upsilon_f = 0.4$$

Determine the composite longitudinal loss factor and the percentage of the total longitudinal damping due to each constituent.

Solution. Substituting the above data in equation (8.87) from the Elastic Viscoelastic Correspondence Principle, or using the strain energy approach and equation (8.155), we find that the composite longitudinal loss factor is

$$\eta_1 = \frac{E''_{f1}\upsilon_f + E''_m\upsilon_m}{E'_{f1}\upsilon_f + E'_m\upsilon_m} = \frac{\eta_{f1}E'_{f1}\upsilon_f + \eta_m E'_m\upsilon_m}{E'_{f1}\upsilon_f + E'_m\upsilon_m} = \frac{0.002(220)(0.6)+0.02(3.45)(0.4)}{220(0.6)+3.45(0.4)}$$

$$= 0.001979 + 0.000207 = 0.002186$$

Thus, the fiber contributes $(0.001979/0.002186) \times 100 = 90.5\%$ of the damping and the matrix contributes the remaining 9.5%. Even though the matrix has a greater loss factor than the fiber, most of the strain energy is stored in the fiber, and this is why the fiber contributes more to the total composite damping. This is not true for the off-axis case, however, as the strain energy in the matrix becomes more significant. For example, the composite transverse loss factor is dominated by the matrix contribution.

8.4 Problems

1. For a linear viscoelastic material, the creep response under a constant stress is followed by a "recovery response" after the stress is removed at some time, t_0. Using the Boltzmann Superposition Principle, find an expression for the uniaxial recovery compliance, $R(t)$, for times $t > t_0$ in terms of the creep compliance, $S(t)$, the time of stress removal, t_0, and the time, t.
2. In general, the creep compliances, $S_{ij}(t)$, and the relaxation moduli, $C_{ij}(t)$, are not related by a simple inverse relationship. Show that only when $t \to 0$ and when $t \to \infty$, can we say that

$$[C_{ij}(t)] = [S_{ij}(t)]^{-1}$$

3. The shear creep compliance, $S_{66}(t)$, for a unidirectional viscoelastic composite is given by $S_{66}(t) = \gamma_{12}(t)/\tau_{12}$, where $\gamma_{12}(t)$ is the time-dependent shear creep strain and τ_{12} is the constant shear stress. If $S_{66}(t)$ can be approximated by a power law as $S_{66}(t) = at^b$, where a and b are material constants and t is time, determine the "constant loading rate compliance" $U_{66}(t) = \gamma_{12}(t)/\tau_{12}(t)$, where the

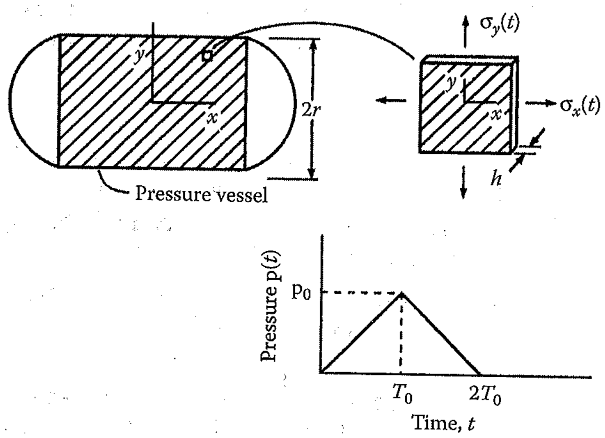

FIGURE 8.41
State of stress in composite pressure vessel and variation of internal pressure with time for problem 8.4.

shear stress is due to a constant loading rate, so that $\tau_{12}(t) = Kt$, where K is a constant.

4. The time-dependent axial stress, $\sigma_x(t)$, and the time-dependent circumferential stress, $\sigma_y(t)$, in the wall of the filament-wound, thin-walled composite pressure vessel shown in figure 8.41 are caused by the internal pressure $p(t)$, where t is time. The required dimensions of the vessel are the wall thickness h and the mean radius r. Note that x and y are not the principal material axes, but, rather, are the longitudinal and transverse axes for the vessel. The variation of $p(t)$ with time is also shown in figure 8.41. If the creep compliances associated with the x and y axes are given in contracted notation by

$$\bar{S}_{ij}(t) = \bar{E}_{ij} + \bar{F}_{ij}t, \quad i,j = 1,2,\ldots,6$$

where the $\bar{E}_{ij}$ and the $\bar{F}_{ij}$ are material constants, determine all the time-dependent strains along the x and y axes for $t > 2T_0$. Answers should be given in terms of p_0, r, h, T_0, t, and the individual $\bar{E}_{ij}$ and $\bar{F}_{ij}$.

5. A linear viscoelastic, orthotropic lamina has principal creep compliances given in contracted notation by

$$S_{ij}(t) = E_{ij} + F_{ij}t, \quad i,j = 1,2,\ldots,6$$

where the E_{ij} and the F_{ij} are material constants and t is time. The lamina is subjected to plane stress with constant stresses

$$\sigma_i(t) = \sigma_i' H(t), \quad i,j = 1,2,\ldots,6$$

where σ_i' are constants and $H(t)$ is the unit step function. If the failure strains for pure longitudinal, transverse, and shear loading of the lamina are e_L, e_T, and e_{LT}, respectively, find the expressions for the time to failure for each of the three strains.

6. Derive the equations for the stress–strain relationship, the creep compliance, and the relaxation modulus for the Kelvin–Voigt model.
7. Derive the equations for the stress–strain relationship, the creep compliance, and the relaxation modulus for the Zener model.
8. Derive equation (8.45).
9. Derive equation (8.47).
10. The shear relaxation modulus, $G_{12}(t)$, and orthotropic lamina is idealized, as shown in figure 8.42. Find the corresponding equations for the shear storage modulus, $G_{12}'(\omega)$, and the shear loss modulus, $G_{12}''(\omega)$, and draw sketches of both parts of the complex modulus in the frequency domain.
11. For the Maxwell model in figure 8.8, express the storage modulus, $E'(\omega)$, the loss modulus, $E''(\omega)$, and the loss factor, $\eta(\omega)$, in terms of the parameters μ and k and the frequency ω. Sketch the variation of $E'(\omega)$, $E''(\omega)$, and $\eta(\omega)$ in the frequency domain. It is not necessary to use Fourier transforms here.
12. Derive equation (8.151) and equation (8.152).
13. The composite pressure vessel in problem 8.4 is subjected to an internal pressure that varies sinusoidally with time according to

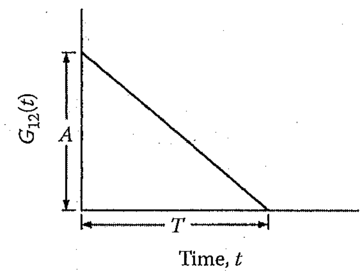

FIGURE 8.42
Variation of shear relaxation modulus, $G_{12}(t)$, with time for problem 8.10.

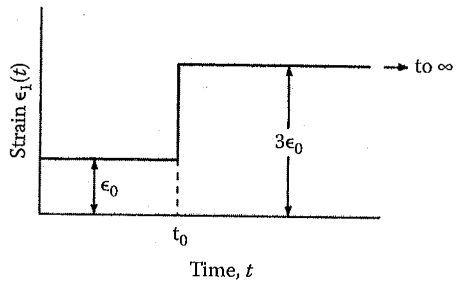

FIGURE 8.43
Composite longitudinal strain–time history for problem 8.14.

the relationship $p(t) = P_0 \sin t$, and the principal complex compliances are given by

$$S_{mn}^*(\omega) = S_{mn}'(\omega) + iS_{mn}''(\omega), \quad m,n = 1,2,\ldots,6$$

where ω is the frequency. Determine all the time-dependent strains associated with the x and y axes in terms of P_0, r, h, w, and the individual $S_{mn}'(\omega)$ and $S_{mn}''(\omega)$.

14. The polymer matrix material in a linear viscoelastic, unidirectional composite material has a relaxation modulus that can be characterized by the Maxwell model in figure 8.8. The fibers are assumed to be linear elastic. If the composite longitudinal strain–time history is as shown in figure 8.43, express the composite longitudinal stress as a function of time.
15. The matrix material in a linear viscoelastic, unidirectional composite material is to be modeled by using a Maxwell model having parameters k_m and μ_m, while the fiber is to be modeled by using a Kelvin–Voigt model having parameters k_f and μ_f.
    (a) Determine the complex extensional moduli of fiber and matrix materials in terms of the Maxwell and Kelvin–Voigt parameters and the frequency, ω.
    (b) Determine the complex longitudinal modulus of the unidirectional composite. Assume that the fiber and matrix materials are isotropic. It is not necessary to use the Fourier transforms.
16. The dynamic mechanical behavior of an isotropic polymer matrix material may be characterized by two independent complex moduli such as the complex extensional modulus, $E^*(\omega)$, and the complex shear modulus, $G^*(\omega)$. Based on experimental evidence

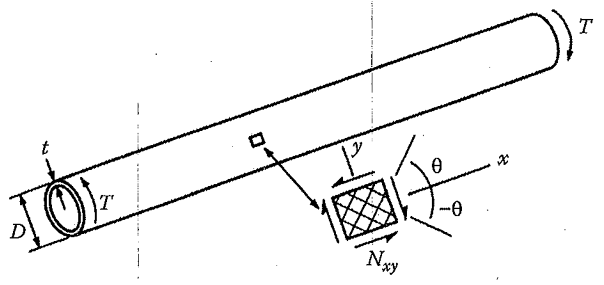

FIGURE 8.44
Composite drive under applied torque for problem 8.17.

however, the imaginary parts of $E^*(\omega)$ and $G^*(\omega)$ are not independent, because the material can be assumed to be viscoelastic in shear but elastic in dilatation (i.e., the shear modulus, $G^*(\omega)$, is complex and frequency dependent, but the bulk modulus, k, is real and frequency independent). Use this simplifying assumption to develop an expression for the shear loss factor, $\eta_G(\omega)$, in terms of the extensional loss factor, $\eta_E(\omega)$, the extensional storage modulus, $E'(\omega)$, and the bulk modulus, k. Assume all loss factors $<< 1$.

17. A drive shaft in the shape of a hollow tube and made of a linear viscoelastic angle-ply laminate is subjected to a torque, T, as shown in figure 8.44. Develop an analytical model for predicting the vibratory shear deformation in the shaft from the vibratory shear force, $\bar{N}_{xy}(t)$, when the torque T varies sinusoidally with time. The input to the model should include the properties and volume fractions of fiber and matrix materials, lamina orientations, and lamina-stacking sequences. That is, the model should include both micromechanical and macromechanical components. No calculations are necessary, but the key equations should be described, all parameters should be defined, and key assumptions should be delineated.
18. Longitudinal vibration of an isotropic, particle-reinforced composite bar may be modeled by using the 1-D wave equation (eq. [8.99]) if the material is linear elastic. Derive the equation of motion for longitudinal vibration of the bar if it can be assumed to be a Kelvin–Voigt linear viscoelastic material having the stress–strain relationship given by equation (8.39).
19. Find the separation of variables solution for the longitudinal displacement, $u(x,t)$, of the equation derived in problem 8.18. Leave the answer in terms of constants, which must be determined from the boundary conditions.

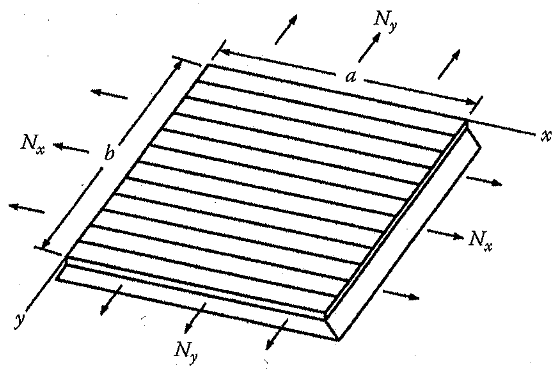

FIGURE 8.45
Simply supported, specially orthotropic plate under in-plane loads for problem 8.20.

20. Derive the equation of motion for free transverse vibration of a simply supported, specially orthotropic plate that is subjected to in-plane loads per unit length N_x and N_y, as shown in figure 8.45.
21. For the plate described in problem 8.20, find the equations for the plate natural frequencies and determine the effects of positive (tensile) and negative (compressive) in-plane loads N_x and N_y on the natural frequencies.
22. If the plate described in problem 8.20 is clamped on all edges, investigate solutions of the form

$$W(x,y) = A_{mn}\left(1-\cos\left(\frac{2\pi x}{a}\right)\right)\left(1-\cos\left(\frac{2\pi y}{b}\right)\right)$$

Does this solution satisfy the boundary conditions? Can it be used to find the natural frequencies? Explain your answers.
23. The isochronous stress–strain curves for an epoxy material at different times are shown in figure 8.46. This material is used as the matrix in a unidirectional E-glass/epoxy composite having a fiber volume fraction of 0.6. Using micromechanics and the Elastic–Viscoelastic Correspondence Principle, determine the longitudinal relaxation modulus $E_1(t)$ for the composite at $t = 1$ hour and $t = 10{,}000$ hours. Note that the strain in figure 8.46 is given in percent strain (e.g., a percent strain value of 1.5 corresponds to a strain of 0.015). Elastic properties of fibers are given in table 1.1.
24. Part of the required input to the viscoelastic option in some finite element codes is a table showing the time-dependent, isotropic

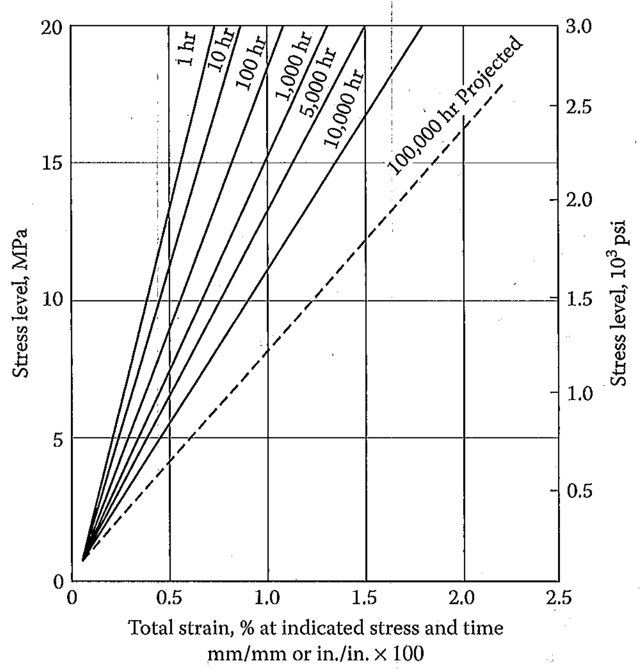

FIGURE 8.46
Isochronous stress-strain curves for epoxy matrix material in problem 8.23.

shear modulus $G(t)$ at different times t. Explain how you would generate such a table from tensile isochronous stress–strain curves such as the ones in figure 8.46. Include the key equations and a list of assumptions in your explanation.

25. For the Maxwell model shown in figure 8.8, it can be shown that the complex modulus is given by

$$E^*(\omega) = E'(\omega)[1 + i\eta(\omega)]$$

where the frequency-dependent storage modulus is given by

$$E'(\omega) = \frac{k\omega^2\lambda^2}{1+\omega^2\lambda^2}$$

and the frequency-dependent loss factor is given by

$$\eta(\omega) = \frac{1}{\omega\lambda}$$

where ω is the frequency and $\lambda = \mu/k$ is the relaxation time. Let us assume that the Maxwell model adequately describes the viscoelastic behavior of a particular material. Explain how you would use the Maxwell model and frequency-domain vibration test data to indirectly determine the numerical value of the relaxation modulus $C(t)$ for this material.

26. A thin-walled cylindrical pressure vessel has mean diameter d = 18 in. and wall thickness h = 0.25 in. The vessel is made of filament-wound unidirectional composite material with all fibers oriented in the circumferential, or hoop, direction. The internal pressure in the vessel can be assumed to be constant. From creep tests of specimens of the unidirectional composite material, it is found that the principal creep compliances can be described by the following power law expressions:

$$S_{11}(t) = 0.121 + 0.0003t^{0.19}$$

$$S_{12}(t) = -0.0315 + 0.004t^{0.19}$$

$$S_{22}(t) = 0.3115 + 0.0025t^{0.19}$$

$$S_{66}(t) = 0.839 + 0.003t^{0.19}$$

where t is the time in minutes and all compliances are given in units of ($\times 10^{-6}$ psi^{-1}). The ultimate failure strains for the material are found to be as follows:

$$e_L^{(+)} = 0.0194,\ e_T^{(+)} = 0.00125,\ e_{LT} = 0.010$$

(a) According to the Maximum Strain Criterion, what is the allowable internal pressure in the vessel, if it is to be designed to last for at least 20 years under constant pressure? (b) How would you change the design of the vessel so as to increase the allowable internal pressure, while maintaining the 20-year design life? Assume here that the composite material properties and vessel dimensions given above cannot be changed, but the material could be modified.

References

1. Schapery, R.A. 1974. Viscoelastic behavior and analysis of composite materials, in Sendeckyj, G.P. ed., *Composite Materials*, vol. 2, *Mechanics of Composite Materials*, pp. 85–168. Academic Press, New York.

2. Beckwith, S.W. 1984. Viscoelastic creep behavior of filament-wound case materials. *Journal of Spacecraft and Rockets*, 21(6), 546–552.
3. Fung, Y.C. 1979. *Foundations of Solid Mechanics*. Prentice-Hall, Inc., Englewood Cliffs, NJ.
4. Christensen, R.M. 1979. *Mechanics of Composite Materials*. John Wiley & Sons, New York.
5. Halpin, J.C. and Pagano, N.J. 1968. Observations on linear anisotropic viscoelasticity. *Journal of Composite Materials*, 2(1), 68–80.
6. Christensen, R.M. 1982. *Theory of Viscoelasticity: An Introduction*, 2nd ed. Academic Press, New York.
7. Sullivan, J.L. 1992. Polymer viscoelasticity. Unpublished notes, Ford Motor Co., Dearborn, MI.
8. McCrum, N.G., Buckley, C.P., and Bucknall, C.B. 1988. *Principles of Polymer Engineering*. Oxford University Press, Oxford, England.
9. Wen, Y.F., Gibson, R.F., and Sullivan, J.L. 1997. Prediction of momentary transverse creep behavior of thermoplastic polymer matrix composites using micromechanical models. *Journal of Composite Materials*, 31(21), 2124–2145.
10. Gibson, R.F. 1979. Measurement of creep in rotating viscoelastic disks. *Experimental Mechanics*, 19(10), 378–383.
11. Gibson, R.F., Baxi, J., Bettinger, D., Stoll, F., and Johnson, V. 1999. Simulation of assembly and operation of pre-stressed, heat-shrinkable structural composite connectors, *Proceedings of ASME Noise Control and Acoustics Division*, NCA Vol. 26. American Society of Mechanical Engineers, New York, pp. 319–332 .
12. Gibson, R.F., Younus, M., Kumar, P., Stoll, F., and Bettinger, D. 1998. Viscoelastic behavior of extended interval lubricator cartridges made from nylon and glass/nylon composites, *Proceedings of 43rd International SAMPE Symposium & Exhibition*. Society for the Advancement of Material and Process Engineering, Covina CA, pp. 2144–2157 .
13. Bracewell, R.N. 1978. *The Fourier Transform and Its Application*, 2nd ed. McGraw-Hill, Inc., New York.
14 Gibson, R.F., Hwang, S.J., and Sheppard, C.H. 1990. Characterization of creep in polymer composites by the use of frequency-time transformations. *Journal of Composite Materials*, 24, 441–453.
15. Lee, E.H. 1955. Stress analysis in viscoelastic bodies. *Quarterly of Applied Mathematics*, 13, 183–190.
16. Biot, M.A. 1958. Linear thermodynamics and the mechanics of solids, *Proceedings of the Third U.S. National Congress of Applied Mechanics*. The National Academies, Washington, D.C., pp. 1–18.
17. Schapery, R.A. 1967. Stress analysis of viscoelastic composite materials. *Journal of Composite Materials*, 1, 228–267.
18. Beckwith, S.W. 1974. Viscoelastic characterization of a nonlinear glass/epoxy composite including the effects of damage. Ph.D. Dissertation, Texas A&M University, College Station, TX.
19. Sims, D.F. and Halpin, J.C. 1974. Methods for determining the elastic and viscoelastic response of composite materials, *Composite Materials: Testing and Design (Third Conference)*, ASTM STP 546, pp. 46–66. American Society for Testing and Materials, Philadelphia, PA.

20. Hashin, Z. 1970. Complex moduli of viscoelastic composites. I: General theory and application to particulate composites. *International Journal of Solids and Structures*, 6, 539–552.
21. Hashin, Z. 1970. Complex moduli of viscoelastic composites ii: fiber reinforced materials. *International Journal of Solids and Structures*, 6, 797–807.
22. Suarez, S.A., Gibson, R.F., Sun, C.T., and Chaturvedi, S.K. 1986. The influence of fiber length and fiber orientation on damping and stiffness of polymer composite materials. *Experimental Mechanics*, 26(2), 175–184.
23. Sun, C.T., Wu, J.K., and Gibson, R.F. 1987. Prediction of material damping of laminated polymer matrix composites. *Journal of Materials Science*, 22, 1006–1012.
24. Findley, W.N., Lai, J.S., and Onaran, K. 1976. *Creep and Relaxation of Nonlinear Viscoelastic Materials*. Dover Publications, New York.
25. Ferry, J.D. 1970. *Viscoelastic Properties of Polymers*, 2d ed. John Wiley & Sons, New York.
26. Struik, L.C.E. 1977. Physical aging in plastics and other glassy materials. *Polymer Engineering and Science*, 17, 165–173.
27. Struik, L.C.E. 1978. *Physical Aging in Amorphous Polymers and Other Materials*. Elsevier, Amsterdam.
28. Janas, V.F. and McCullough, R.L. 1987. The effects of physical aging on the viscoelastic behavior of a thermoset polyester. *Composites Science and Technology*, 30, 99–118.
29. Ogale, A.A. and McCullough, R.L. 1987. Physical aging of polyether ether ketone. *Composites Science and Technology*, 30, 137–148.
30. Sullivan, J.L. 1990. Creep and physical aging of composites. *Composites Science and Technology*, 39, 207–232.
31. Scott, D.W., Lai, J.S., and Zureick, A.-H. 1995. Creep behavior of fiber-reinforced polymeric composites: A review of the technical literature. *Journal of Reinforced Plastics and Composites*, 14, 588–617.
32. Hearmon, R.F.S. 1961. *An Introduction to Applied Anisotropic Elasticity*. Oxford University Press, Oxford, England.
33. Achenbach, J.D. 1974. Waves and vibrations in directionally reinforced composites, in Sendeckyj, G.P. ed., *Composite Materials*, vol. 2, *Mechanics of Composite Materials*. Academic Press, New York.
34. Ross, C.A. and Sierakowski, R.L. 1975. Elastic waves in fiber reinforced materials. *The Shock and Vibration Digest*, 7(1), 1–12.
35. Moon, F.C. 1974. Wave propagation and impact in composite materials, in Chamis, C.C. ed., *Composite Materials*, vol. 7. Academic Press, New York.
36. Whitney, J.M. 1987. *Structural Analysis of Laminated Anisotropic Plates*. Technomic Publishing Co., Lancaster, PA.
37. Vinson, J.R. and Sierakowski, R.L. 1986. *The Behavior of Structures Composed of Composite Materials*. Martinus Nijhoff Publishers, Dordrecht, The Netherlands.
38. Sierakowski, R.L. and Chaturvedi, S.K. 1997. *Dynamic Loading and Characterization of Fiber-Reinforced Composites*. John Wiley & Sons, Inc., New York.
39. Meirovitch, L. 1986. *Elements of Vibration Analysis*, 2d ed. McGraw-Hill, Inc., New York.

40. Timoshenko, S.P., Young, D.H., and Weaver, W., Jr. 1974. *Vibration Problems in Engineering*. John Wiley & Sons, New York.
41. Dudek, T.J. 1970. Young's and shear moduli of unidirectional composites by a resonant beam method. *Journal of Composite Materials*, 4, 232–241.
42. Ni, R.G. and Adams, R.D. 1984. The damping and dynamic moduli of symmetric laminated beams — Theoretical and experimental results. *Journal of Composite Materials*, 18, 104–121.
43. Huang, T.C. and Huang, C.C. 1971. Free vibrations of viscoelastic Timoshenko beam. *Journal of Applied Mechanics*, 38, Series E(2), 515–521.
44. Nakao, T., Okano, T., and Asano, I. 1985. Theoretical and experimental analysis of flexural vibration of the viscoelastic Timoshenko beam. *Journal of Applied Mechanics*, 52(3), 728–731.
45. Jones, R.M. 1973. Buckling and vibration of unsymmetrically laminated cross-ply rectangular plates. *AIAA Journal*, 11(12), 1626–1632.
46. Gibson, R.F. 1992. Damping characteristics of composite materials and structures. *Journal of Engineering Materials and Performance*, 1(1), 11–20.
47. Gibson, R.F. 1987. Dynamic mechanical properties of advanced composite materials and structures: A review. *The Shock and Vibration Digest*, 19(7), 13–22.
48. Gibson, R.F. 1990. Dynamic mechanical properties of advanced composite materials and structures: A review of recent research. *The Shock and Vibration Digest*, 22(8), 3–12.
49. Bert, C.W. 1980. Composite materials: A survey of the damping capacity of fiber reinforced composites, in Torvik, P.J. ed., *Damping Applications for Vibration Control*, AMD vol. 38, pp. 53–63. American Society of Mechanical Engineers, New York.
50. Adams, R.D. 1987. Damping properties analysis of composites, in Reinhart, T.J. ed., *Engineered Materials Handbook*, vol. 1, *Composites*, pp. 206–217. ASM International Materials Park, OH.
51. Chaturvedi, S.K. 1989. Damping of polymer matrix composite materials, in Lee, S. ed., *Encyclopedia of Composites*. VCH Publishing Co., New York.
52. Kinra, V.K. and Wolfenden, A. eds. 1992. *M3D: Mechanics and Mechanisms of Material Damping*, ASTM/STP 1169. American Society for Testing and Materials, Philadelphia, PA.
53. Sun, C.T. and Lu, Y.P. 1995. *Vibration Damping of Structural Elements*. Prentice Hall, Englewood Cliffs, NJ.
54. Zener, C. 1948. *Elasticity and Anelasticity of Metals*. The University of Chicago Press, Chicago, IL.
55. Granato, A.V. and Lucke, K. 1956. Application of dislocation theory to internal friction phenomena at high frequencies. *Journal of Applied Physics*, 27(7), 789–805.
56. Sun, C.T., Chaturvedi, S.K., and Gibson, R.F. 1985. Internal material damping of polymer matrix composites under off-axis loading. *Journal of Materials Science*, 20, 2575–2585.
57. Sun, C.T., Wu, J.K., and Gibson, R.F. 1985. Prediction of material damping in randomly oriented short fiber polymer matrix composites. *Journal of Reinforced, Plastics and Composites*, 4, 262–272.

58. Pant, R.H. and Gibson, R.F. 1996. Analysis and testing of dynamic micromechanical behavior of composite materials at elevated temperatures. *Journal of Engineering Materials and Technology*, 118, 554–560.
59. Finegan, I.C. and Gibson, R.F. 2000. Analytical modeling of damping at micromechanical level in polymer composites reinforced with coated fibers. *Composites Science and Technology*, 60, 1077–1084.
60. Guan, H. and Gibson, R.F. 2001. Micromechanical models for damping in woven fabric-reinforced polymer matrix composites. *Journal of Composite Materials*, 35(16), 1417–1434.
61. Nashif, A.D., Jones, D.I.G., and Henderson, J.P. 1985. *Vibration Damping*. John Wiley & Sons, New York.
62. Ungar, E.E. and Kerwin, E.M., Jr. 1962. Loss factors of viscoelastic systems in terms of strain energy. *Journal of the Acoustical Society of America*, 34(2), 954–958.
63. Gibson, R.F., Chaturvedi, S.K., and Sun, C.T. 1982. Complex moduli of aligned discontinuous fiber reinforced polymer composites. *Journal of Materials Science*, 17, 3499–3509.
64. Johnson, C.D. and Kienholz, D.A. 1982. Finite element prediction of damping in structures with constrained viscoelastic layers. *AIAA Journal*, 20(9), 1284–1290.
65. Hwang, S.J. and Gibson, R.F. 1987. Micromechanical modeling of damping in discontinuous fiber composites using a strain energy/finite element approach. *Journal of Engineering Materials and Technology*, 109, 47–52.
66. Gibson, R.F., Hwang, S.J., and Kwak, H. 1991. Micromechanical modeling of damping in composites including interphase effects, in *How Concept Becomes Reality — Proceedings of 36th International SAMPE Symposium*, vol. 1, pp. 592–606. Society for the Advancement of Material and Process Engineering, Covina, CA.
67. Hwang, S.J. and Gibson, R.F. 1991. The effects of 3-D states of stress on damping of laminated composites. *Composites Science and Technology*, 41, 379–393.
68. Hwang, S.J. and Gibson, R.F. 1992. Contribution of interlaminar stresses to damping in thick laminated composites under uniaxial extension. *Composite Structures*, 20, 29–35.
69. Hwang, S.J., Gibson, R.F., and Singh, J. 1992. Decomposition of coupling effects on damping of laminated composites under flexural vibration. *Composites Science and Technology*, 43, 159–169.
70. Mantena, P.R., Gibson, R.F., and Hwang, S.J. 1991. Optimal constrained viscoelastic tape lengths for maximizing damping in laminated composites. *AIAA Journal*, 29(10), 1678–1685.
71. Hwang, S.J. and Gibson, R.F. 1992. The use of strain energy-based finite element techniques in the analysis of various aspects of damping of composite materials and structures. *Journal of Composite Materials*, 26(17), 2585–2605.
72. Chen, Y. and Gibson, R.F. 2003. Analytical and experimental studies of composite isogrid structures with integral passive damping. *Mechanics of Advanced Materials and Structures*, 10(2), 127–143.

73. Plagianakos, T.S. and Saravanos, D.S. 2003. Mechanics and finite elements for the damped dynamic characteristics of curvilinear laminates and composite shell structures. *Journal of Sound and Vibration*, 263(2), 399–414.
74. Li, Z. and Crocker, M.J. 2005. A review on vibration damping in sandwich composite structures. *International Journal of Acoustics and Vibration*, 10(4), 159–169.
75. Gibson, R.F., Ayorinde, E.O., and Wen, Y.F. 2007. Vibrations of carbon nanotubes and their composites: A review. *Composites Science and Technology*, 67(1), 1–28.

9

Analysis of Fracture

9.1 Introduction

Except for a brief discussion in section 7.8.2, the previous chapters of this book have not considered the analysis of the effects of notches, cracks, delaminations, or other discontinuities in composites. For example, the conventional strength analyses outlined in chapter 4 involved the use of gross "effective lamina strengths" in various semiempirical failure criteria without regard for specific micromechanical failure modes that are related to such discontinuities. While such procedures, along with the use of empirical "safety factors," may produce a satisfactory design for static loading, failures may still occur due to the growth of cracks or delaminations under dynamic loading. The purpose of this chapter is to give an introduction to the analysis of fracture of composites due to cracks, notches, and delaminations.

First, the prediction of the strength of composites with through-thickness cracks and notches is considered by using both fracture mechanics and stress fracture approaches. Next, the use of fracture mechanics in the analysis of interlaminar fracture will be discussed. Each of these topics is the subject of many publications. Thus, only brief introductions to the subjects are given here, along with key references where more detailed analyses may be found. Each of these topics is also the subject of considerable current research, and the reader is encouraged to consult technical journals for the results of the most recent research. Composites handbooks are a good place to find information on the basics of composite fracture [1]. The Special Technical Publication (STP) series by the American Society for Testing and Materials is a good source of recent research findings [2–7]. The application of fracture mechanics to composites is the subject of a book [8], as is delamination in composites [9].

9.2 Fracture Mechanics Analyses of Through-Thickness Cracks

Much of the early work on fracture in composites involved investigations of the applicability of linear elastic fracture mechanics, which had been originally developed for the analysis of through-thickness cracks in homogeneous, isotropic metals. The origin of fracture mechanics can be traced back to the seminal work of Griffith [10], who explained the discrepancy between the measured and predicted strength of glass by considering the stability of a small crack. The stability criterion was developed by using an energy balance on the crack.

Consider the through-thickness crack in the uniaxially loaded homogeneous, isotropic, linear elastic plate of infinite width shown in figure 9.1. Griffith reasoned that the strain energy of the cracked plate would be less than the corresponding strain energy of the uncracked plate, and from a stress analysis, he estimated that the strain energy released by the creation of the crack under plane stress conditions would be

$$U_r = \frac{\pi\sigma^2 a^2 t}{E} \tag{9.1}$$

where U_r = strain energy released
σ = applied stress
a = half-crack length
t = plate thickness
E = modulus of elasticity of the plate

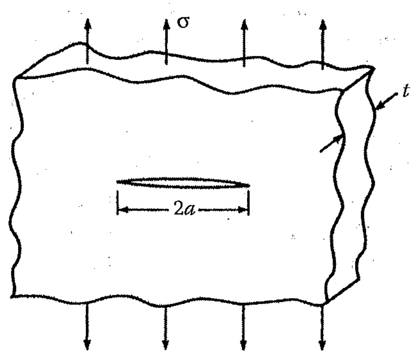

FIGURE 9.1
The Griffith crack: A through-thickness crack in a uniaxially stressed plate of infinite width.

The corresponding expression in Griffith's original paper was later found to be in error, and Eq. (9.1) is consistent with the corrected expression in more recent publications [9.11, 9.12]. In addition, Griffith's energy terms were given on a per unit thickness basis. Equation (9.1) is also consistent with the strain energy released by relaxation of an elliptical zone having major and minor axes of lengths $4a$ and $2a$, respectively, where the minor axis is coincident with the crack and the major axis is perpendicular to the crack. The volume of such an ellipse is
or

$$V = \pi(2a)(a)(t) = 2\pi a^2 t \tag{9.2}$$

Since the plate was assumed to be uniformly stressed before the introduction of the crack, the strain energy released due to relaxation of the elliptical volume around the crack is

$$U_r = \frac{1}{2}\frac{\sigma^2}{E}V = \frac{\pi\sigma^2 a^2 t}{E} \tag{9.3}$$

Griffith also assumed that the creation of new crack surfaces required the absorption of an amount of energy given by

$$U_s = 4at\gamma_s \tag{9.4}$$

where U_s = energy absorbed by creation of new crack surfaces
γ_s = surface energy per unit area

As the crack grows, if the rate at which energy is absorbed by creating new surfaces is greater than the rate at which strain energy is released, then

$$\frac{\partial U_s}{\partial a} > \frac{\partial U_r}{\partial a} \tag{9.5}$$

and crack growth is stable. If the strain energy is released at a greater rate than it can be absorbed, then

$$\frac{\partial U_r}{\partial a} > \frac{\partial U_s}{\partial a} \tag{9.6}$$

and crack growth is unstable. The threshold of stability, or the condition of neutral equilibrium, is therefore given by

$$\frac{\partial U_r}{\partial a} = \frac{\partial U_s}{\partial a} \tag{9.7}$$

or

$$\frac{\pi\sigma^2 a}{E} = 2\gamma_s \tag{9.8}$$

Thus, the critical stress, σ_c, for self-sustaining extension of the crack in plane stress is

$$\sigma_c = \sqrt{\frac{2E\gamma_s}{\pi a}} \tag{9.9}$$

Alternatively, the critical flaw size for plane stress at stress level σ is

$$a_c = \frac{2E\gamma_s}{\pi\sigma^2} \tag{9.10}$$

It is interesting to note that when we rearrange Eq. (9.8) as

$$\sigma\sqrt{\pi a} = \sqrt{2E\gamma_s} \tag{9.11}$$

the terms on the left-hand side depend only on loading and geometry, whereas the terms on the right-hand side depend only on material properties. Thus, when the stress reaches the critical fracture stress, σ_c, the left-hand side becomes $\sigma_c\sqrt{\pi a}$. The term $\sigma_c\sqrt{\pi a}$ is now referred to as the fracture toughness, K_c. This is a very important concept, which we will return to later.

The application of the Griffith-type analysis to composites presents some difficulties, but, fortunately, many of these problems have been solved over the years since Griffith's work. For example, for metals and many polymers the energy absorbed in crack extension is actually greater than the surface energy. Recognizing this, both Irwin [9.13] and Orowan [9.14] modified the Griffith analysis to include energy absorption due to plastic deformation at the crack tip. In this analysis the factor $2\gamma_s$ on the right-hand side of Eq. (9.8) and in all subsequent equations is replaced by the factor $2(\gamma_s + \gamma_p)$, where γ_p is the energy of plastic deformation. The solutions of several other problems encountered in the development of composite fracture mechanics have been made possible by the use of several different analytical techniques. Two of these techniques, now referred to as the "stress intensity factor" approach and the "strain energy release rate" approach, will be discussed in the following sections.

9.2.1 Stress Intensity Factor Approach

The Griffith analysis was originally developed for homogeneous, isotropic materials. Using effective modulus theory, we can replace the heterogeneous, anisotropic composite with an equivalent homogeneous, anisotropic material. It turns out that by considering the stress distribution around

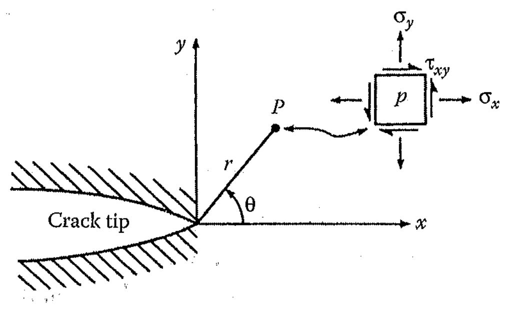

FIGURE 9.2
Stresses at the tip of a crack under plane stress.

the crack tip, we can develop another interpretation of the Griffith analysis which can be applied equally well to homogeneous isotropic or anisotropic materials and to states of stress other than the simple uniaxial stress that Griffith used. Referring to the plane stress condition in the vicinity of the uniaxially loaded crack in figure 9.2, Westergaard [15] used a complex stress function approach to show that the stresses for the isotropic case at a point P defined by polar coordinates r, θ can be expressed as

$$\sigma_x = \frac{K_I}{\sqrt{2\pi r}} f_1(\theta) \tag{9.12}$$

$$\sigma_y = \frac{K_I}{\sqrt{2\pi r}} f_2(\theta) \tag{9.13}$$

$$\tau_{xy} = \frac{K_I}{\sqrt{2\pi r}} f_3(\theta) \tag{9.14}$$

where K_I is the stress intensity factor for the crack opening mode, as defined by

$$K_I = \sigma\sqrt{\pi a} \tag{9.15}$$

and the $f_i(\theta)$ are trigonometric functions of the angle. Irwin [16] recognized that the term $\sigma\sqrt{\pi a}$ controls the magnitudes of the stresses at a point r, θ near the crack tip. Returning to the discussion following equation (9.11), we see that the critical value of the stress intensity factor, K_{Ic}, corresponding to the critical stress, σ_c, is the fracture toughness. That is,

$$K_{Ic} = \sigma_c\sqrt{\pi a} \tag{9.16}$$

The fracture toughness, K_{Ic}, is a material property that can be determined experimentally, as shown later. Thus, if the fracture toughness of the material is known, the fracture mechanics analysis can be used in two ways, depending on whether the applied stress or the crack size is known. If the applied stress, σ, is known, equations such as equation (9.15) can be used to find the critical crack size, a_c, which will lead to unstable and catastrophic crack growth. Knowing the critical crack size, we can specify inspection of the component in question to make sure that there are no cracks of that size. On the other hand, if the crack size, a, is known, then equations such as equation (9.15) can be used to find the critical stress, σ_c, which will lead to unstable and catastrophic crack growth. Loading on the component in question would then be specified so as not to exceed this stress.

The reader is cautioned that the stress intensity factor is defined as $k_1 = \sigma\sqrt{a}$ in some publications. This definition corresponds to the cancellation of $\sqrt{\pi}$ in both the numerator and denominator of equation (9.12) to equation (9.14), so that the denominator corresponding to k_1 would be $\sqrt{2r}$ instead of $\sqrt{2\pi r}$, and thus $K_I = k_1\sqrt{\pi}$.

Expressions for stress distributions for other types of loading and crack geometries in isotropic materials lead to expressions that are similar to equation (9.12) to equation (9.14), and the corresponding stress intensity factors can be found in the same way [17]. Other important results such as finite width correction factors (recall that the Griffith analysis is for a crack in an infinite width plate) have been tabulated in ref. [17]. The three basic modes of crack deformation are shown in figure 9.3. Thus, for the crack opening mode in the above example (mode I), we have the stress intensity factor K_I. For the in-plane shear mode (mode II) we have the stress intensity factor K_{II}, and for the antiplane shear mode (mode III) we have K_{III}. For example, for the cases of pure shear loading in modes II and III we have

$$K_{II} = \tau\sqrt{\pi a} \quad \text{and} \quad K_{III} = \tau\sqrt{\pi a} \tag{9.17}$$

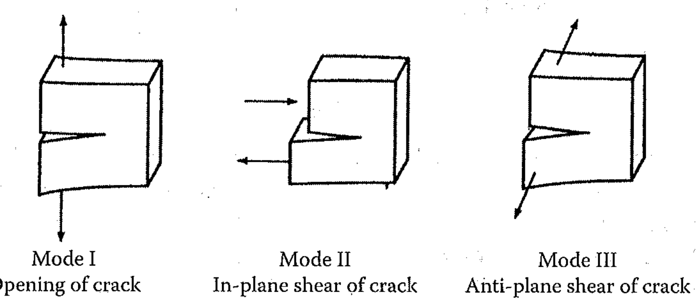

FIGURE 9.3
The three basic modes of crack deformation.

where the shear stress, τ, is different for modes II and III, as shown in figure 9.3.

Although the stress analyses for the corresponding anisotropic material cases are more difficult and the expressions are more complicated, the stress intensity factors for certain loading conditions and crack geometries are the same as those for the isotropic case. For example, Lekhnitskii [18] has used a stress function approach to show that if the crack shown in figure 9.1 and figure 9.2 lies in an anisotropic material for which the xy plane is a plane of material property symmetry, then the stresses are given by

$$\sigma_x = \frac{K_I}{\sqrt{2\pi r}} F_1(\theta, s_1, s_2) \tag{9.18}$$

$$\sigma_y = \frac{K_I}{\sqrt{2\pi r}} F_2(\theta, s_1, s_2) \tag{9.19}$$

and

$$\tau_{xy} = \frac{K_I}{\sqrt{2\pi r}} F_3(\theta, s_1, s_2) \tag{9.20}$$

where the functions $F_i(\theta, s_1, s_2)$ include not only trigonometric functions of the angle, θ, but also s_1 and s_2, which are complex roots of the characteristic equation corresponding to a differential equation in the stress function [18]. As pointed out by Wu [19], the magnitudes of the stresses at point r, θ in an isotropic material (eq. [9.12] to eq. (9.14]) are completely determined by the stress intensity factors, but in the anisotropic case (eq. [9.18] to eq. [9.20]), these magnitudes also depend on s_1 and s_2. Wu [19] has also shown, however, that if the crack lies along a principal material direction in the anisotropic material, then the stress intensity factors given by equation (9.15) and equation (9.17) are still valid for their respective loading conditions shown in figure 9.3.

Several experimental investigations have shown that the concept of a critical stress intensity factor can be used to describe the fracture behavior of through-thickness cracked unidirectional composites and laminates. Wu [19] reasoned that if the fracture toughness, K_{Ic}, is a material constant, then by considering the logarithm of equation (9.16), the slope of the log σ_c versus log a_c plot must be –0.5. Wu's experimental results for unidirectional E-glass/epoxy showed good agreement with this prediction. Konish et al. [20] showed that the critical stress intensity factors for 0°, 90°, 45° $[\pm 45°]_s$, and $[0°/\pm 45°/90°]_s$ graphite/epoxy laminates could be determined by using the same fracture toughness test method that had been developed for metals. Parhizgar et al. [21] showed both analytically and experimentally that the fracture toughness of unidirectional E-glass/epoxy composites is a constant material property that does not depend on crack length but that does depend on fiber orientation.

The fracture toughness, K_{Ic}, has been found to be an essentially constant material property for a variety of randomly oriented short-fiber composites, as shown in papers by Alexander et al. [22] and Sun and Sierakowski [23]. Although the random fiber orientation in such materials allows one to use the numerous tabulated solutions for stress intensity factors of isotropic materials [17], it appears that the simple crack growth assumed in the Griffith-type analysis does not always occur in these materials. As an alternative to crack growth, the concept of a damage zone ahead of the crack tip in short-fiber composites has been proposed by Gaggar and Broutman [24].

9.2.2 Strain Energy Release Rate Approach

One of the major drawbacks of the stress intensity factor approach is that a stress analysis of the crack tip region is required. While such analyses have been done for a variety of loading conditions and crack geometries for isotropic materials [17], the corresponding analyses for anisotropic materials have only been done for relatively few cases because of mathematical difficulties. A very useful alternative to the stress intensity factor approach is referred to as the "strain energy release rate" approach. The strain energy release rate has an easily understood physical interpretation that is equally valid for either isotropic or anisotropic materials, and it turns out that this rate is also related to the stress intensity factor. The strain energy release rate approach has proved to be a powerful tool in both experimental and computational studies of crack growth.

The derivation of the strain energy release rate presented here follows that of Irwin [25], as explained by Corten [26]. We first consider a through-thickness cracked linear elastic plate under a uniaxial load, as shown in figure 9.4(a). An increase in the load, P, from the unloaded condition causes a linearly proportional change in the displacement, u, at the point of application of the load, as shown in the load–displacement plot in figure 9.4(b). We now assume that once the load reaches the value P_1 and the corresponding displacement reaches u_1, the crack extends a small increment, Δa. The crack extension causes the load to drop by an amount ΔP and the displacement to increase by an amount Δu. Just before the crack extension occurs, the potential energy, U, stored in the plate is given by the triangular area OAC in figure 9.4(b). The potential energy, ΔU, released by the crack extension is given by the triangular area OAB. During the incremental displacement Δu, the increment of work done on the plate is ΔW or the

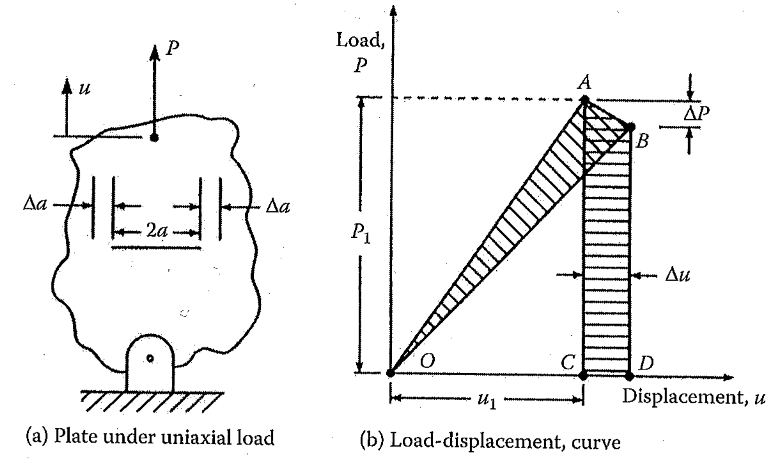

FIGURE 9.4
Loaded plate and corresponding load–displacement curve used for strain energy release rate analysis.

area ABDC. For this mode I crack deformation, the strain energy release rate, G_I (do not confuse with the shear modulus, G), or the rate of change of the strain energy with respect to the crack extension area, A, is defined by [26]

$$G_I = \lim_{\Delta A \to 0} \frac{\Delta W - \Delta U}{\Delta A} = \frac{dW}{dA} - \frac{dU}{dA} \tag{9.21}$$

The system compliance, s, is given by

$$s = \frac{u}{p} \tag{9.22}$$

(Note that this is the system compliance, s, not the material compliance, S, defined earlier as being a ratio of strain to stress.) Thus, the potential energy of the plate in figure 9.4(a) is

$$U = \frac{1}{2}Pu = \frac{1}{2}sP^2 \tag{9.23}$$

so that

$$\frac{dU}{dA} = sP\frac{\partial P}{\partial A} + \frac{1}{2}P^2\frac{\partial s}{\partial A} \tag{9.24}$$

The incremental work done during the crack extension is approximately

$$\Delta W = P(\Delta u) \tag{9.25}$$

so that

$$\begin{aligned}\frac{\mathrm{d}W}{\mathrm{d}A} &= \lim_{\Delta A \to 0} \frac{\Delta W}{\Delta A} = \lim_{\Delta A \to 0} P \frac{\Delta u}{\Delta A} = P \frac{\mathrm{d}u}{\mathrm{d}A} = P \frac{\mathrm{d}}{\mathrm{d}A}(sP) \\ &= Ps \frac{\partial P}{\partial A} + P^2 \frac{\partial s}{\partial A}\end{aligned} \tag{9.26}$$

Substitution of equation (9.24) and equation (9.26) in equation (9.21) gives

$$G_{\mathrm{I}} = \frac{P^2}{2} \frac{\partial s}{\partial A} \tag{9.27}$$

For a plate of constant thickness, t, $\partial A = t\,\partial a$ and

$$G_{\mathrm{I}} = \frac{P^2}{2t} \frac{\partial s}{\partial a} \tag{9.28}$$

Thus, we can determine G_{I}, by plotting the compliance as a function of crack length and finding the slope of the curve, $\mathrm{d}s/\mathrm{d}a$, corresponding to the value of the load, P. The critical strain energy release rate, G_{Ic}, for this mode I crack deformation corresponds to the values P_{c} and $(\mathrm{d}s/\mathrm{d}a)_{\mathrm{c}}$ at fracture. That is,

$$G_{\mathrm{Ic}} = \frac{P_{\mathrm{c}}^2}{2t} \left(\frac{\partial s}{\partial a} \right)_{\mathrm{c}} \tag{9.29}$$

From the point of view of the experimentalist, the obvious advantage of equation (9.29) is that knowledge of material properties or crack stress distributions is not needed since all the parameters can be determined from measurements on a test specimen. Note also that the method applies to either isotropic or anisotropic materials. As shown later in section 9.4, equation (9.21) has been used extensively for both measurement and calculation of the strain energy release rate for mode I delamination in

laminates. Measurements of the strain energy release rate based on these equations will be discussed in chapter 10.

Another major advantage of the strain energy release rate is that it is related to the stress intensity factor. As shown by Irwin [13], for mode I crack deformation in isotropic materials under plane stress,

$$K_{\mathrm{I}}^2 = G_{\mathrm{I}} E \tag{9.30}$$

so that the critical stress intensity factor or fracture toughness, K_{Ic}, is related to the critical strain energy release rate, G_{Ic}, by

$$K_{\mathrm{Ic}}^2 = G_{\mathrm{Ic}} E \tag{9.31}$$

This relationship has used to determine the K_{Ic} of composites from measurements of the G_{Ic} [23] and to find G_{Ic} from measurements of K_{Ic} [20].

Cruse [27] has shown that for a through-thickness mode I crack in an orthotropic laminate having N angle-ply components and having strain compatibility among the plies ahead of the crack the critical strain energy release rate, G_{Ic}, for the laminate is related to the corresponding lamina properties by a simple rule of mixtures of the form

$$G_{\mathrm{Ic}} = \frac{\sum_{i=1}^{N} G_{\mathrm{Ic}i} t_i}{t} \tag{9.32}$$

where G_{Ic} = critical strain energy release rate for the laminate
$G_{\mathrm{Ic}i}$ = critical strain energy release rate for the ith angle-ply component
t = total laminate thickness
t_i = thickness of the ith angle-ply component

The predictions from this equation were found to show good agreement with experimental results for graphite/epoxy laminates [27].

The strain energy release rate has also proved to be useful in the characterization of the crack growth rate under cyclic loading. Interest in the possible relationship between fatigue crack growth rate and the strain energy release rate was prompted by the previous work of Paris and Erdogan [28], which showed that the mode I crack growth rate, $\mathrm{d}a/\mathrm{d}N$, in many metals and polymers can be characterized by the equation

$$\frac{\mathrm{d}a}{\mathrm{d}N} = B(\Delta K)^m \tag{9.33}$$

where N = number of cycles of repetitive loading

ΔK = stress intensity factor range = $K_{Imax} - K_{Imin} = (\sigma_{max} - \sigma_{min})\sqrt{\pi a}$ for mode I crack growth

σ_{max} = maximum stress

σ_{min} = minimum stress

B, m = experimentally determined empirical factors for a given material, loading conditions, and environment

Equation (9.33) has also found limited use in composites. For example, Kunz and Beaumont [29] observed that transverse crack growth in unidirectional graphite/epoxy composites under cyclic compressive loading could be described by such an equation. Fatigue damage in composites cannot always be described in terms of self-similar crack growth, however. More often than not, fatigue damage is a very complex condition involving mixed modes of failure, and the analytical determination of the stress intensity factor for such a condition may be nearly impossible. Thus, the strain energy release rate range, ΔG, may be a more convenient parameter to use than the stress intensity factor range, ΔK. For example, Spearing et al. [30] have modeled fatigue damage growth in notched graphite/epoxy laminates by using an equation formed by combining equation (9.30) and equation (9.33):

$$\frac{da}{dN} = C(\Delta G)^{m/2} \tag{9.34}$$

where $C = BE^{m/2}$

EXAMPLE 9.1

A quasi-isotropic graphite/epoxy laminate has a fracture toughness K_{Ic} = 30 MPa $m^{1/2}$ and a tensile strength of 500 MPa. As shown in figure 9.5, a 25-mm-wide structural element made from this material has an edge crack of length a = 3 mm. If the element is subjected to a uniaxial stress, σ, determine the critical value of the stress that would cause unstable propagation of the crack. Compare this stress with the tensile strength of the material, which does not take cracks into account.

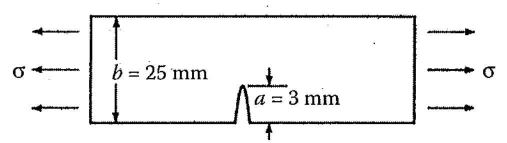

FIGURE 9.5
Single-edge crack in a plate under uniaxial stress for example 9.1.

Solution. From tabulated solutions [17], the stress intensity factor for the single-edge crack in figure 9.5 is

$$K_I = \sigma\sqrt{\pi a}\, f(a/b)$$

where the function $f(a/b)$ is given by the empirical formula [17] $f(a/b) = 1.12 - 0.231(a/b) + 10.55(a/b)^2 - 21.72(a/b)^3 + 30.39(a/b)^4$ which is said to be accurate within 0.5% when $a/b \le 0.6$. For this case, $a/b = 3/25 = 0.12$ and $f(a/b) = 1.213$. The critical stress is then

$$\sigma_c = \frac{K_{Ic}}{\sqrt{\pi a}\, f(a/b)} = \frac{30}{\sqrt{\pi(0.003)}(1.213)} = 255\text{MPa}$$

Comparing this stress with the tensile strength of 500 MPa, we see that in this case the cracked element can sustain only about 50 percent of the stress that an uncracked element could withstand.

9.2.3 Virtual Crack Closure Technique

The so-called Virtual Crack Closure Technique (VCCT) has its origins in the seminal work of Irwin [25], was first implemented in finite element form by Rybicki and Kanninen [31], and has since evolved as a popular finite element computational tool for calculating the strain energy release rate and stress intensity factors. A recent review article by Krueger [32] summarizes the history, approach, and applications of the VCCT to composites, particularly to the case of delamination cracks.

Irwin [25] originally proposed that, when the crack tip shown schematically in figure 9.2 has been extended by the amount Δa, the energy released during crack extension is equal to the energy required to close the crack to its original length. For the 2-D state of stress in figure 9.2, where the origin of the polar coordinates (r,θ) is located at the extended crack tip, Irwin suggested that the energy release rate G for a crack extension Δa is given by the crack closure integral [31]

$$G = \lim_{\Delta a \to 0} \frac{1}{2\Delta a}\int_0^{\Delta a} \sigma_y(\Delta a - r, 0)v(r,\pi)dr + \lim_{\Delta a \to 0} \frac{1}{2\Delta a}\int_0^{\Delta a} \tau_{xy}(\Delta a - r, 0)u(r,\pi)dr \tag{9.35}$$

where u and v are the relative sliding (x direction) and opening (y direction) displacements between points on the crack faces. The first and second integrals in equation (9.35) are recognized to be G_I and G_{II} and the Mode I and Mode II energy release rates, respectively. Rybicki and

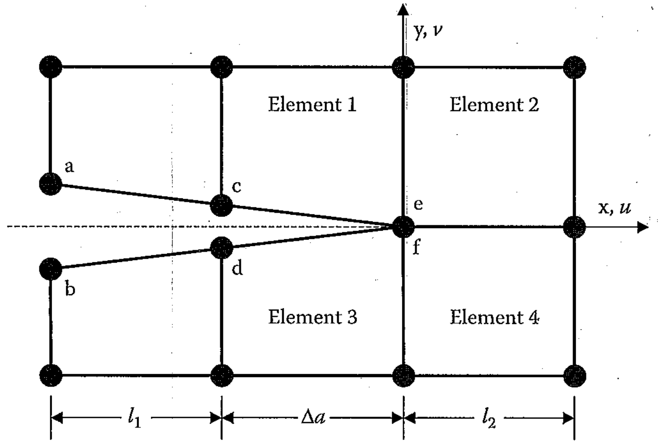

FIGURE 9.6
Finite element nodes near the crack tip for the VCCT. (From Rybicki, E.F. and Kanninen, M.F. 1997. *Engineering Fracture Mechanics*, 9, 931–938. With permission.)

Kanninen [31] later proposed that for the arrangement of four-noded 2-D finite elements in figure 9.6, Irwin's crack closure integrals could be approximated by

$$G_{I} = \lim_{\Delta a \to 0} \frac{1}{2\Delta a} F_{cy}(v_c - v_d) \tag{9.36}$$

and

$$G_{II} = \lim_{\Delta a \to 0} \frac{1}{2\Delta a} F_{cx}(u_c - u_d) \tag{9.37}$$

where Δa is the element length along the x direction, F_{cx} and F_{cy} are the forces along x and y directions, respectively, that are required to hold nodes c and d together during crack closure, (u_c, v_c) are the x and y displacements, respectively, of point c, and (u_d, v_d) are the x and y displacements, respectively, of point d during crack closure. Since the publication of the paper by Rybicki and Kanninen [31], there have been numerous publications by others reporting on various improvements and applications of the VCCT to cracks in composites, particularly delamination cracks. Among the reported improvements are the use of eight-noded 2-D finite elements, 20-noded 3-D brick elements, plate or shell elements, and nonlinear finite elements, as well as the use of the VCCT to analyze fractures at bimaterial interfaces such as those in composites [32]. As noted in section 9.4, many

of the publications regarding the VCCT involve applications to composite delamination. One potential problem with the VCCT is the existence of the $1/\sqrt{r}$ singularities in the stresses as $r \to 0$ at the crack tip, as seen in equation (9.12) to equation (9.14) and equation (9.18) to equation (9.20). Special crack tip singularity elements have been shown to be effective in accurately approximating these singularities, but apparently these special elements are not readily available in many commonly used finite element codes [32].

9.3 Stress Fracture Criteria for Through-Thickness Notches

Although fracture mechanics concepts have been successfully used in some cases to analyze the effects of through-thickness cracks and notches in composite laminates, Whitney and Nuismer [33,34] questioned the need for such an approach and then proceeded to develop a simpler approach that is perhaps more useful to designers. As pointed out previously, the use of fracture mechanics in such applications has always been in question because the self-similar crack growth that occurs in metals does not always occur in composite laminates. Additional motivation for the work of Whitney and Nuismer was provided by the need to understand better experimental results that showed larger holes in laminates under tension cause greater strength reductions than do smaller holes. In a previous attempt to explain this effect, Waddoups et al. [35] had employed a fracture mechanics analysis of a hole in an isotropic plate with two symmetrically placed cracks extending from either side of the hole, as shown in figure 9.7.

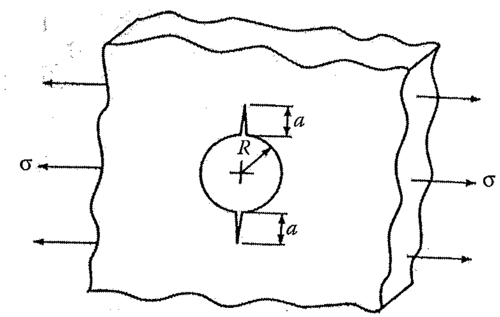

FIGURE 9.7
Uniaxially stressed plate with an edge-cracked hole.

The stress intensity factor for a mode I crack having this geometry was derived using the previous solution of Bowie [36] as

$$K_I = \sigma\sqrt{\pi a}\, f(a/R) \tag{9.38}$$

While the function $f(a/R)$ has been tabulated for the isotropic case [17], it has not been determined for the anisotropic case. Thus, although the analysis of Waddoups et al. [35] predicted the experimentally observed trends regarding the effect of hole size, the effects of anisotropy were obviously not considered. In addition, no physical interpretation was given for the cracks at the edge of the hole (i.e., such cracks were used in the analysis but were not necessarily present in the experiments that showed the hole size effect).

Whitney and Nuismer [33,34] reasoned that the hole size effect could also be explained by observing the differences in the stress distributions near the hole for large and small holes. For example, the theory of elasticity solutions [37] for the normal stress distribution, σ_y, along the x axis near a hole in an infinite isotropic plate under uniform tensile stress are shown in figure 9.8 for small ($R = 0.1$ in.) and large ($R = 1.0$ in.) holes. The stress distribution for the smaller hole obviously has a sharper concentration near the hole than does the stress distribution for the larger hole. Whitney and Nuismer observed that since the plate with the smaller hole would be more capable of redistributing high stresses near the hole than would the plate with the larger hole, the plate with the smaller hole would be stronger. This observation led to the development of two failure criteria that were based on solutions for the normal stress, σ_y, along the x axis near circular holes (fig. 9.8) and center cracks (fig. 9.9) in infinite orthotropic plates. The Whitney–Nuismer criteria [33,34] are now summarized.

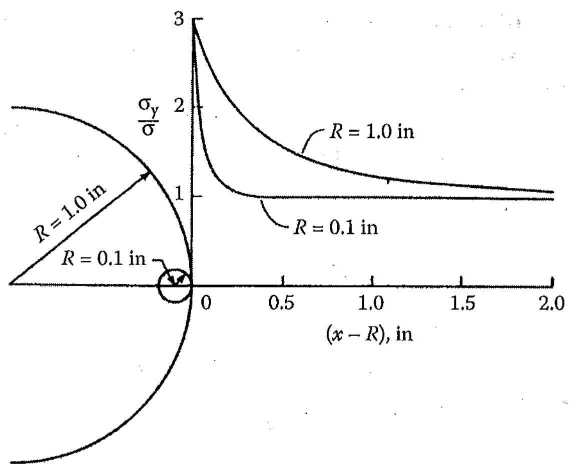

FIGURE 9.8
Normal stress distribution for a circular hole in an infinite isotropic plate. (From Nuismer, R.J. and Whitney, J.M. 1975. *Fracture Mechanics of Composites*, ASTM STP 593, pp. 117–142. American Society for Testing and Materials, Philadelphia, PA. Copyright ASTM. Reprinted with permission.)

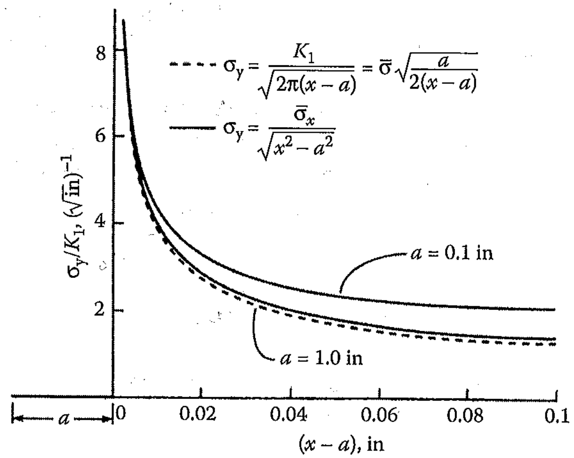

FIGURE 9.9
Normal stress distribution for a center crack in an infinite anisotropic plate. (From Nuismer, R.J. and Whitney, J.M. 1975. *Fracture Mechanics of Composites*, ASTM STP 593, pp. 117–142. American Society for Testing and Materials, Philadelphia, PA. Copyright ASTM. Reprinted with permission.)

The hole of radius R in figure 9.8 is assumed to be in an infinite orthotropic plate that is under uniform stress, σ, at infinity. The normal stress, $\sigma_y(x, 0)$, along the x axis near the hole is approximately

$$\sigma_y(x,0) = \frac{\sigma}{2}\left\{2 + \left(\frac{R}{x}\right)^2 + 3\left(\frac{R}{x}\right)^4 - \left(K_T^\infty - 3\right)\left[5\left(\frac{R}{x}\right)^6 - 7\left(\frac{R}{x}\right)^8\right]\right\} \tag{9.39}$$

where $x > R$ and the orthotropic stress concentration factor, K_T^∞, for an infinite width plate is given by Lekhnitskii [38] as

$$K_T^\infty = 1 + \sqrt{\frac{2}{A_{22}}\left(\sqrt{A_{11}A_{22}} - A_{12} + \frac{A_{11}A_{22} - A_{12}^2}{2A_{66}}\right)} \tag{9.40}$$

where the A_{ij} are the laminate extensional stiffnesses from the Classical Lamination Theory and the subscript 1 denotes the direction parallel to the applied stress, σ.

The first failure criterion proposed by Whitney and Nuismer, referred to as the "point stress criterion," is based on the assumption that failure occurs when the stress σ_y at some fixed distance, d_0, away from the edge of the hole reaches the unnotched tensile strength of the material, σ_0. This criterion is given by

$$\sigma_y(R+d_0,0)=\sigma_0 \tag{9.41}$$

By combining equation (9.39) and equation (9.41), we find that the ratio of notched to unnotched strength is

$$\frac{\sigma_N^\infty}{\sigma_0}=\frac{2}{2+\xi_1^2+3\xi_1^4-\left(K_T^\infty-3\right)\left(5\xi_1^6-7\xi_1^8\right)} \tag{9.42}$$

where

$$\xi_1=\frac{R}{R+d_0}$$

and the notched tensile strength, σ_N^∞, of the infinite width laminate is equal to the applied stress, σ, at failure. Whitney and Nuismer noted that for very large holes $\xi_1\to 1$, and the classical stress concentration result, $\sigma_N^\infty/\sigma_0=1/K_T^\infty$, is recovered. As $\xi_1\to 0$, however, $\sigma_N^\infty/\sigma_0\to 1$, as expected.

The second failure, criterion proposed by Whitney and Nuismer, referred to as the "average stress criterion," is based on the assumption that failure occurs when the average value of σ_y over some fixed distance, a_0, from the edge of the hole reaches the unnotched tensile strength of the material, σ_0. This criterion is given by

$$\frac{1}{a_0}\int_R^{R+a_0}\sigma_y(x,0)dx=\sigma_0 \tag{9.43}$$

By combining equation (9.39) and equation (9.43), we find that the ratio of notched to unnotched strength is

$$\frac{\sigma_N^\infty}{\sigma_0}=\frac{2(1-\xi_2)}{2-\xi_2^2-\xi_2^4+\left(K_T^\infty-3\right)\left(\xi_2^6-\xi_2^8\right)} \tag{9.44}$$

where

$$\xi_2=\frac{R}{R+a_0}$$

and σ_N^∞ is again the notched tensile strength of the infinite width laminate. As in the point stress criterion, the expected limits are recovered for the cases when $\xi_2\to 1$ and $\xi_2\to 0$.

Whitney and Nuismer also applied the point stress criterion and the average stress criterion to the case of the center crack of length $2a$ in an infinite anisotropic plate under uniform tensile stress, σ, as shown in figure 9.9. They used Lekhnitskii's [38] exact elasticity solution for the normal stress, σ_y, along the x axis near the edge of the crack, which is given by

$$\sigma_y(x,0)=\frac{\sigma x}{\sqrt{x^2-a^2}}=\frac{K_I x}{\sqrt{\pi a(x^2-a^2)}} \tag{9.45}$$

where $x>a$ and $K_I=\sigma\sqrt{\pi a}$ is the mode I stress intensity factor. Substitution of this stress distribution in the point stress failure criterion given by equation (9.41) leads to the expression

$$\frac{\sigma_N^\infty}{\sigma_0}=\sqrt{1-\xi_3^2} \tag{9.46}$$

where

$$\xi_3=\frac{a}{a+d_0}$$

Substitution of the stress distribution from equation (9.45) in the average stress criterion given by equation (9.43) yields

$$\frac{\sigma_N^\infty}{\sigma_0}=\sqrt{\frac{1-\xi_4}{1+\xi_4}} \tag{9.47}$$

where

$$\xi_4=\frac{a}{a+a_0}$$

Whitney and Nuismer then reasoned that the effect of crack size on the measured fracture toughness of the notched laminate could be better understood by defining a parameter

$$K_Q = \sigma_N^\infty \sqrt{\pi a} \tag{9.48}$$

which is the fracture toughness corresponding to the notched tensile strength of the infinite width laminate. Substitution of equation (9.46) in equation (9.48) yields

$$K_Q = \sigma_0 \sqrt{\pi a \left(1 - \xi_3^2\right)} \tag{9.49}$$

for the point stress criterion. Similarly, substitution of equation (9.47) in equation (9.48) yields

$$K_Q = \sigma_0 \sqrt{\frac{\pi a (1 - \xi_4)}{1 + \xi_4}} \tag{9.50}$$

for the average stress criterion. For vanishly small crack lengths, a, the numerical values of both equation (9.49) and equation (9.50) approach the limit $K_Q = 0$. For large crack lengths K_Q asymptotically approaches

$$K_Q = \sigma_0 \sqrt{2\pi d_0} \tag{9.51}$$

for the point stress criterion and

$$K_Q = \sigma_0 \sqrt{\pi a_0 / 2} \tag{9.52}$$

for the average stress criterion.

In order to use these stress fracture criteria, it is necessary to do enough experiments to establish values of d_0 or a_0 that give acceptable predicted values of σ_N^∞. Whitney and Nuismer observed that the applicability of these criteria in design depends to a great extent on whether the distance d_0 or a_0 is constant for all hole or crack sizes in at least a particular laminate of a particular material system. If d_0 or a_0 was constant for all laminates of all material systems, the criteria would be even more useful.

Whitney and Nuismer showed that fixed values of d_0 and a_0 in the criteria gave reasonably good agreement with experimental results for graphite/epoxy and glass/epoxy laminates in two different laminate configurations [34]. For example, figure 9.10 shows a comparison of the predictions from the point stress criterion for circular holes (eq. [9.42]) and the average stress criterion for circular holes (eq. [9.44]) with experimental data for $[0/\pm 45/90]_{2s}$ graphite/epoxy laminates. Similarly, figure 9.11

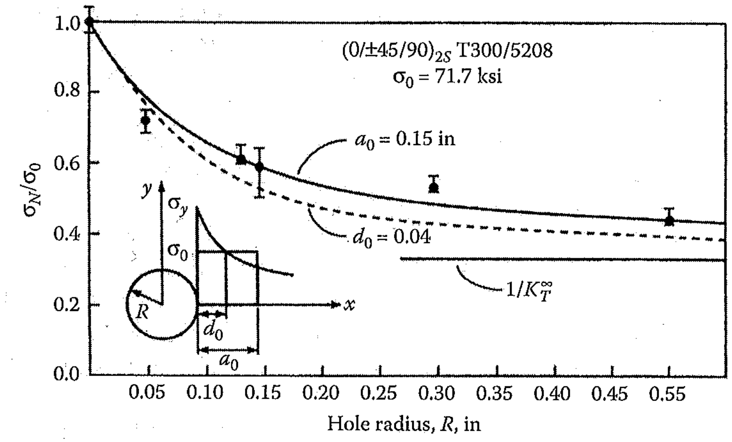

FIGURE 9.10
Comparison of predicted and measured failure stresses for circular holes in $[0/\pm 45/90]_{2s}$ T300/5208 graphite/epoxy. (From Nuismer, R.J. and Whitney, J.M. 1975. *Fracture Mechanics of Composites*, ASTM STP 593, pp. 117–142. American Society for Testing and Materials, Philadelphia, PA. Copyright ASTM. Reprinted with permission.)

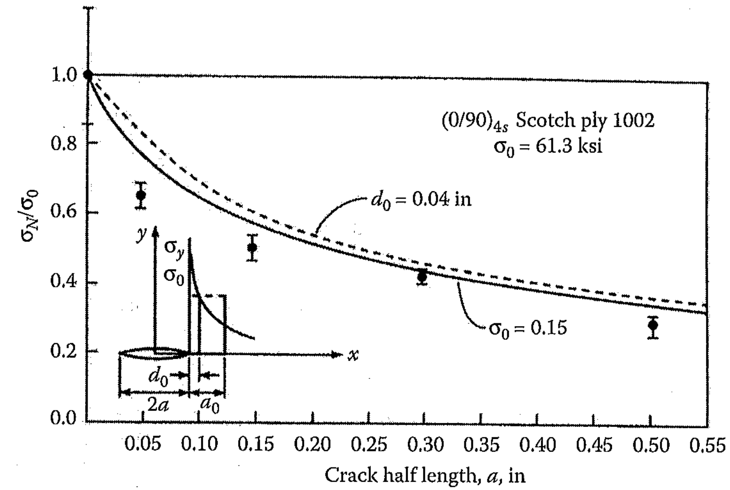

FIGURE 9.11
Comparison of predicted and measured failure stresses for center cracks in $[0/90]_{4S}$ Scotchply 1002 E-glass/epoxy. (From Nuismer, R.J. and Whitney, J.M. 1975. *Fracture Mechanics of Composites*, ASTM STP 593, pp. 117–142. American Society for Testing and Materials, Philadelphia, PA. Copyright ASTM. Reprinted with permission.)

shows a comparison of the predictions from the point stress criterion for center cracks [eq. (9.46)] and the average stress criterion for center cracks [eq. (9.47)] with experimental data for $[0/90]_{4s}$ glass/epoxy laminates. Note that the same values of d_0 and a_0 were used for both material systems and laminate configurations, and that both criteria correctly predict the effect of the hole size or crack size on the notched strength. The results for graphite/epoxy are not quite so good as those for glass/epoxy, however. Even though it could not be concluded from this work that d_0 and a_0 are universal constants, the equations can be used with confidence for a particular material system under uniaxial loading. It should also be remembered that these criteria can be used for any through-thickness discontinuity for which the theoretical stress distribution can be found, not just for circular holes or straight cracks. Thus, given the relative simplicity of the equations, the Whitney–Nuismer criteria appear to be of considerable value to designers.

EXAMPLE 9.2

A large plate made from the quasi-isotropic graphite/epoxy laminate in example 9.1 has a center crack of length $2a = 6$ mm and is subjected to a uniform uniaxial stress. Compare the predicted fracture strengths of the plate according to the fracture mechanics criterion, the point stress criterion, and the average stress criterion. Use the Whitney–Nuismer values of d_0 and a_0 from figure 9.10 and figure 9.11.

Solution. For the fracture mechanics approach we rearrange equation (9.16) as

$$\sigma_c = \frac{K_{1c}}{\sqrt{\pi a}} = \frac{30}{\sqrt{\pi(0.003)}} = 309\,\text{MPa}$$

For the point stress criterion we use $d_0 = 0.04$ in. = 1.016 mm and $a = 3$ mm in equation (9.46) as

$$\sigma_N^{\infty} = \sigma_0\sqrt{1-\xi_3^2} = (500)\sqrt{1-[3.0/(3.0+1.016)]^2} = 332\,\text{MPa}$$

For the average stress criterion we use $a_0 = 0.15$ in = 3.81 mm and $a = 3$ mm in equation (9.47) as

$$\sigma_N^{\infty} = \sigma_0\sqrt{\frac{1-\xi_4}{1+\xi_4}} = (500)\sqrt{\frac{1-(3.0/(3.0+3.81))}{1+(3.0/(3.0+3.81))}} = 312\,\text{MPa}$$

The results from all three analyses are reasonably close, and the fracture mechanics criterion is slightly more conservative than the point stress criterion and the average stress criterion in this case. Clearly, the predicted fracture strengths in all three cases are considerably lower than the unnotched tensile strength of 500 MPa, and we see that the effects of such cracks should not be ignored in design.

9.4 Interlaminar Fracture

Delamination or interlaminar fracture is a very important failure mode in composite laminates, and research activity regarding the onset and growth of delaminations has continued at a high level for the past several decades or so. The mechanics of interlaminar stresses and several mechanics of materials approaches to the prediction of the onset of delamination were discussed previously in chapter 7. In this section, we will discuss the use of fracture mechanics approaches, particularly those involving the use of the strain energy release rate, for the prediction of delamination growth and failure.

Delamination provides one of the few examples of self-similar crack growth in composite laminates. A delamination is in effect a crack separating adjacent laminae, and the plane of the crack lies in the plane of the interface between laminae. Like a crack in a metallic material, a delamination grows in a stable manner until it reaches a critical size, whereupon further growth occurs in an unstable manner. These characteristics make interlaminar fracture a prime candidate for the application of fracture mechanics analysis. On the other hand, as pointed out in chapter 7, interlaminar stresses are part of a complex 3-D state of stress that leads to delamination. While such a complex state of stress at the crack tip inhibits the effective use of the stress intensity factor approach, it makes the problem ideally suited for the strain energy release rate approach.

One of the first reports on the use of the strain energy release rate approach in the analysis of delamination was apparently that of Roderick et al. [39], who correlated strain energy release rates with the rates of cyclic debonding between metal panels and composite reinforcement using an equation similar to equation (9.34). Shortly thereafter, in a critical review of the applications of fracture mechanics in composites, Kanninen et al. [40] noted that the strain energy release rate had seen little application to composites. This observation led to the use of the strain energy release rate by Rybicki et al. [41] in an analytical and experimental study of free-edge delamination in boron/epoxy laminates. Rather than using equation (9.21) to calculate the strain energy release rate, Rybicki et al. [41] employed a finite element implementation of the crack closure technique

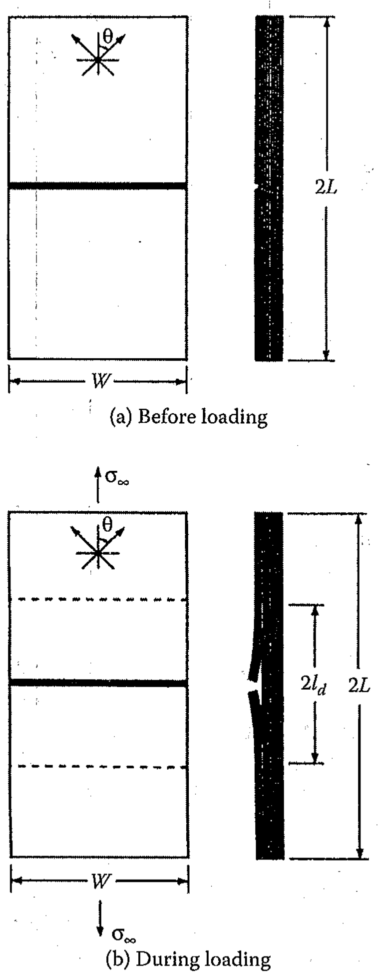

FIGURE 9.12
Specimen for delamination crack growth study ($2L = 152.4$ mm, $W = 25.4$ mm). (From Wang, S.S. 1979. In Tsai, S.W. ed., *Composite Materials: Testing and Design*, ASTM STP pp. 674, 642–663. American Society for Testing and Materials, Philadelphia, PA. Copyright ASTM. Reprinted with permission.)

described as the VCCT in section 9.2.3. This appears to be the first application of the VCCT to the analysis of delamination cracks, but since that time there have been numerous reports in the literature regarding the application of the VCCT to delamination cracks [32].

Wang [42] conducted experimental and analytical studies of delamination growth in unidirectional glass/epoxy composite specimens. As shown in figure 9.12, delamination crack initiators were introduced in the

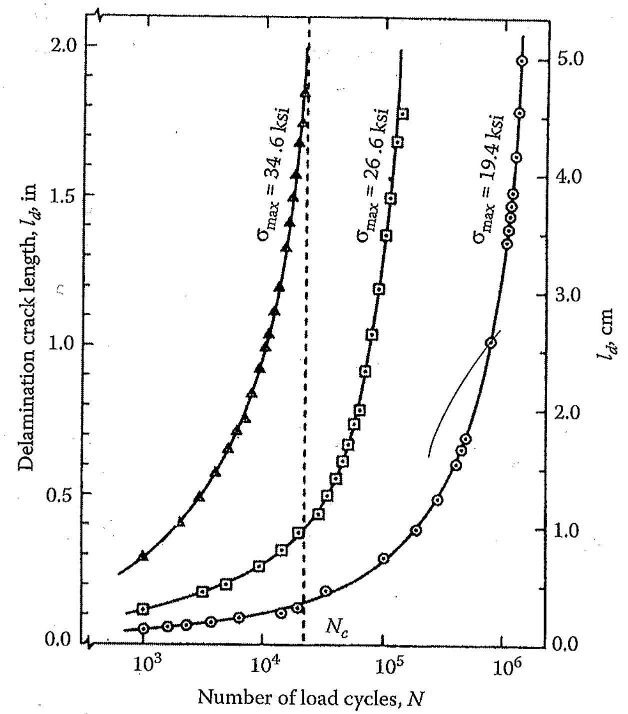

FIGURE 9.13
Delamination crack growth during fatigue in unidirectional glass/epoxy. (From Wang, S.S. 1979. In Tsai, S.W. ed., *Composite Materials: Testing and Design*, ASTM STP pp. 674, 642–663. American Society for Testing and Materials, Philadelphia, PA. Copyright ASTM. Reprinted with permission.)

specimens by cutting across several surface plies with a razor blade. The specimens were then subjected to cyclic tension–tension fatigue loading while the length of the delamination, l_d, was measured. Figure 9.13 shows typical data on delamination crack length versus the number of load cycles, N, at different stress levels. The delamination growth rate, dl_d/dN, at any number N is the tangent of the curve at that value of N. It is particularly important to note in figure 9.13 that at a critical number of loading cycles, N_c, corresponding to a critical delamination size for a given stress level, the delamination growth becomes unstable and rapid crack propagation occurs. Such experiments provided further proof of the similarity between crack growth in metals and delamination growth in composite laminates and justified the use of the principles of fracture mechanics in the analysis of delamination.

Wang [42] used a hybrid stress finite element method to determine the stress intensity factors K_I and K_{II} for the mixed mode crack growth, which were then correlated with the delamination growth rate by equations similar to equation (9.33). In this case, due to the mixed mode delamination, the relationships for the two crack deformation modes are

$$\frac{dl_d}{dN} \sim (\Delta K_I)^a \tag{9.53}$$

for mode I crack opening and

$$\frac{dl_d}{dN} \sim (\Delta K_{II})^b \tag{9.54}$$

for mode II crack shearing, where a and b are empirically determined exponents. Equation (9.53) and equation (9.54), when plotted on a log–log plot, should form a straight line. The validity of these equations is confirmed by plotting the experimental data on a 3-D log–log plot, as shown in figure 9.14.

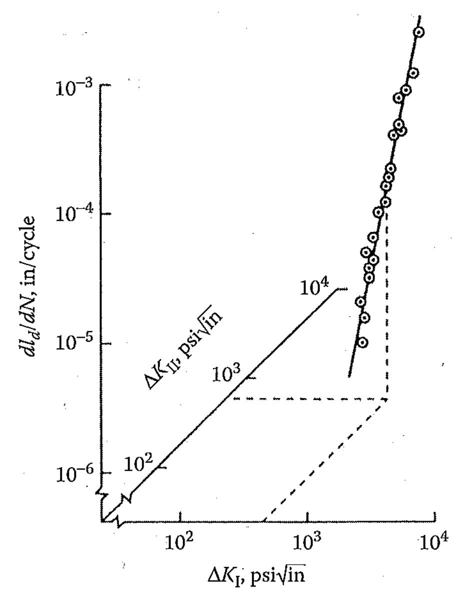

FIGURE 9.14
Fatigue delamination crack growth rate, dl_d/dN, as a function of mixed mode stress intensity factor ranges ΔK_I, and ΔK_{II} for unidirectional glass/epoxy. (From Wang, S.S. 1979. In Tsai, S.W. ed., *Composite Materials: Testing and Design*, ASTM STP pp. 674, 642–663. American Society for Testing and Materials, Philadelphia, PA. Copyright ASTM. Reprinted with permission.)

The data in figure 9.14 were found to follow a general relationship of the form

$$\frac{\log(dl_a/dN)}{\alpha_1} = \frac{\log(\Delta K_I)+C_1}{\alpha_2} = \frac{\log(\Delta K_{II})+C_2}{\alpha_3} \tag{9.55}$$

where the $\alpha_i (i=1,2,3)$ are the directional cosines of the line $dl_d/dN = f(\Delta K_I, \Delta K_{II})$ with respect to the three axes, respectively, and C_1 and C_2 are constants associated with the opening and shearing modes, respectively.

Both mechanics of materials and fracture mechanics analyses were used by O'Brien [43] to study the onset and growth of edge delaminations (see previous fig. 7.36) in graphite/epoxy laminates. O'Brien's mechanics of materials approach was discussed previously in chapter 7. A laminate-stacking sequence of $[\pm 30/\pm 30/90/\overline{90}]_s$ was selected so that edge delamination growth in tensile specimens would readily occur under cyclic loading, and delamination growth was monitored nondestructively. The strain energy release rate, G, associated with delamination growth was determined from two different analyses, only one of which will be discussed here. One method involved the use of the general equation for the strain energy release rate, equation (9.21). The work done during crack extension, W, was ignored, so that

$$G = -\frac{dU}{dA} \tag{9.56}$$

The subscript I on G has been dropped here because the edge delamination growth is of the mixed mode type and the strain energy release rate may have components due to G_I, G_{II}, and G_{III}. Superposition of the strain energy release rates for different modes will be discussed later. Expressing the strain energy in terms of the strain energy density, $E\varepsilon^2/2$, and the volume, V, equation (9.56) becomes

$$G = -V\frac{\varepsilon^2}{2}\frac{dE}{dA} \tag{9.57}$$

where ε = nominal longitudinal strain
E = longitudinal Young's modulus of a laminate partially delaminated along one or more interfaces

In this case $dA = 2Lda$ and $V = 2bLt$, where a, b, and t were defined previously in figure 7.36 and L is the length of the laminate. Substituting these definitions in equation (9.57), along with the definition of E from equation (7.115), O'Brien found that

$$G = \frac{\varepsilon^2 t}{2}(E_x - E_{td}) \tag{9.58}$$

where E_x and E_{td} were defined previously along with equation (7.115). Thus, the strain energy release rate is independent of delamination size and depends only on E_x and E_{td} (which are determined by the laminate lay-up and the location of the delaminated interfaces), the strain, ε, and the thickness, t. The critical strain, ε_c, at the onset of delamination was measured for the $[\pm 30/\pm 30/90/\overline{90}]_s$ laminates and used in equation (9.58) to determine the corresponding critical strain energy release rate, G_c. This value of G_c was then used to predict the critical value, ε_c, at the onset of delamination in $[+45_n/-45_n/0_n/90_n]_s$ laminates. A comparison of measured and predicted values of ε_c for different numbers of plies, n, is shown in figure 9.15, and the agreement is seen to be very good.

As previously mentioned, the edge delamination test used by O'Brien [43] involved mixed mode crack deformations. He used a finite element implementation of a crack closure technique developed by Rybicki et al. [41] to find the components G_I, G_{II}, and G_{III}. The total G was then found from the superposition relationship

$$G = G_I + G_{II} + G_{III} \tag{9.59}$$

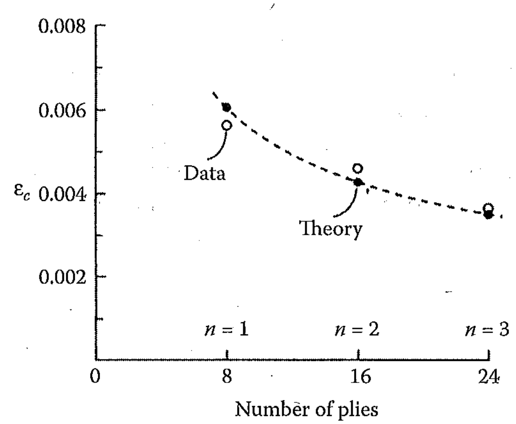

FIGURE 9.15
Edge delamination onset prediction compared with experimental data for $[+45_n/45_n/0_n/90_n]_s$ graphite/epoxy, where $n = 1, 2, 3$. (From O'Brien, T.K. 1982. In Reifsnider, K.L. ed., *Damage in Composite Materials*, ASTM STP 775, pp. 140–167. American Society for Testing and Materials, Philadelphia, PA. Copyright ASTM. Reprinted with permission.)

In this case G_{III} turned out to be negligible. Equation (9.59) is valid when the plane of the crack and the plane of crack extension coincide with a principal axis of material property symmetry [26].

O'Brien also found excellent correlation between delamination growth rate, da/dN, and the maximum strain energy release rate, G_{max}, by using an equation of the form

$$\frac{da}{dN} = cG_{max}^{\beta} \tag{9.60}$$

where c and β are empirically determined constants. Figure 9.16 shows a comparison of predictions from this equation with experimental data, and the agreement is excellent.

As described above, the experiments of Wang [42] and O'Brien [43] involved mixed mode delamination, and the different components of the stress intensity factor or the strain energy release rate corresponding to modes I, II, and III had to be determined separately by using finite element techniques. In order to understand delamination better and, consequently, the best ways to improve interlaminar fracture toughness, there is an obvious need for delamination experiments which make it possible to isolate a single mode of crack growth. In the following paragraphs the most widely used experiments for single-mode measurement of interlaminar strain energy release rates will be briefly discussed, but details of the techniques will be left for chapter 10 on mechanical testing of composites.

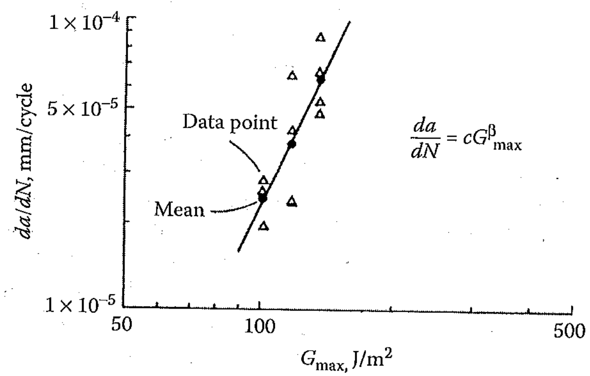

FIGURE 9.16
Power law curve fit for da/dN as a function of G_{max} for $[\pm 30/30/90/\overline{90}]_s$, graphite/epoxy. (From O'Brien, T.K. 1982. In Reifsnider, K.L. ed., *Damage in Composite Materials*, ASTM STP 775, pp. 140–167. American Society for Testing and Materials, Philadelphia, PA. Copyright ASTM. Reprinted with permission.)

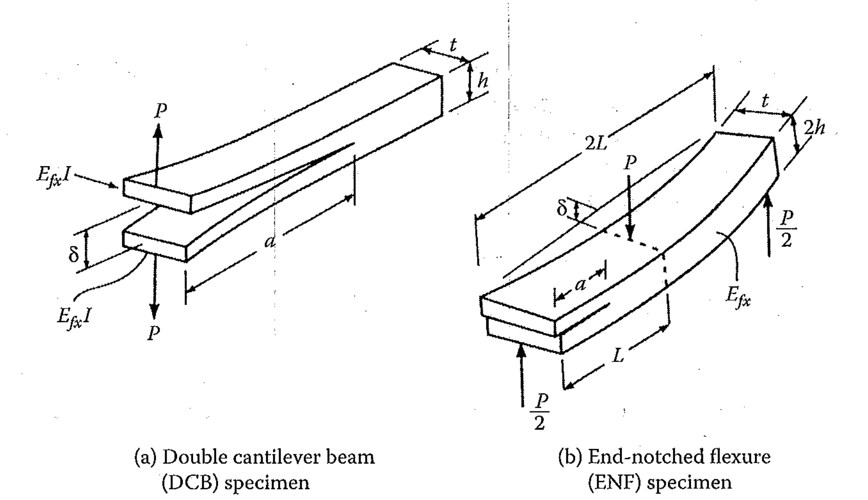

FIGURE 9.17
DCB and ENF specimens.

Mode I delamination has always been of interest because of the obvious weakness of the interlaminar region in through-thickness tension. Perhaps the most widely used mode I interlaminar fracture test method is the double cantilever beam (DCB) test, which was originally developed for studying fracture of adhesively bonded joints and then later adapted for interlaminar fracture of composite laminates [44–51]. A DCB specimen is shown in figure 9.17(a). In the DCB test the specimen is loaded transversely as shown in figure 9.17(a), so that mode I crack opening delamination occurs along the middle plane. The required test data are taken and the delamination G_{Ic} is calculated by using one of several different forms of equation (9.21) or equation (9.27), as described later in chapter 10. Typical values of delamination G_{Ic} for several advanced composites, as determined by DCB tests, are tabulated in table 9.1. The results of some of the attempts to improve the interlaminar fracture toughness are seen in table 9.1, and these methods will be discussed in more detail later in this section.

Although mode I delamination has received considerable attention in the literature, there is increased interest in mode II delamination because of its apparent relationship to impact damage tolerance of laminates [52]. As mentioned in section 7.8.2, transverse impact can cause internal cracks and delaminations that may be difficult to detect. If the laminate is subsequently subjected to in-plane compressive loading, such cracks and delaminations can lead to buckling and reductions of in-plane compressive strength (fig. 7.39). There is evidence that the so-called compression after impact strength is improved by increasing the mode II critical interlaminar strain energy release rate, G_{IIc} [52]. One of the most popular tests for

TABLE 9.1

Critical Interlaminar Strain Energy Release Rates, G_{Ic}, for Several Advanced Composites, as Determined by DCB Tests

Fiber/Matrix Combination	Lay-up	G_{Ic} J/m^2 (in-lb/in²)	Source
T-300/5208 Graphite/epoxy	$[0]_{24}$	87.6(0.50)	(1)
AS-1/3502 Graphite/epoxy	$[0]_{24}$	140.1(0.80)	(2)
AS-4/3502 Graphite/epoxy	$[0]_{24}$	161.1(0.92)	(2)
T-300/V387A Graphite/bismaleimide	$[0]_{24}$	71.8(0.41)	(2)
AS-1/polysulfone Graphite/polysulfone	$[0]_{12}$	585.0(3.34)	(2)
T-300/976 Graphite/epoxy bidirectional cloth	Woven, fabric, 10 plies	282.0(1.61)	(2)
AS-4/3501-6 Graphite/epoxy	$[0]_{24}$	198–254(1.31–1.45)[a]	(3)
T-300/F-185 Graphite/epoxy	$[0]_{24}$	1880–1500(10.7–8.6)[b]	(4)
AS-4/PEEK Graphite/ polyetheretherketone	$[0]_{40}$	2890–2410(16.5–13.8)[c]	(5)

[a] Range of G_{Ic} is given for crack velocities of 0.05–49.0 mm/s, respectively. Thus, G_{Ic} increases with increasing strain rate for this material. The matrix is Hercules 3501-6, a standard prepreg-type epoxy resin [47].

[b] Range of G_{Ic} is given for crack velocities of 0.01–21.0 mm/sec, respectively. Thus, G_{Ic} decreases with increasing strain rate for this material. The matrix is Hexcel F-185, which is an elastomer-modified and toughened epoxy [48].

[c] Range of G_{Ic} is given for stable and unstable crack growth, respectively [49].

Source: (1) Wilkins, D.J., Eisenmann, J.R., Camin, R.A., Margolis, W.S., and Benson, R.A. 1982. In Reifsnider, K.L. ed., *Damage in Composite Materials.* ASTM STP 775, pp. 168–183, American Society for Testing and Materials, Philadelphia, PA. (2) Whitney, J.M., Browning, C.E., and Hoogsteden, W. 1982. *Journal of Reinforced Plastics and Composites,* 1, 297–313. (3) Aliyu, A.A. and Daniel, I.M. 1985. In Johnson, W.S., ed., *Delamination and Debonding of Materials.* ASTM STP 876, pp. 336–348, American Society for Testing and Materials, Philadelphia, PA. (4) Daniel, I.M., Shareef, I., and Aliyu, A.A. 1987. In Johnston, N.J. ed., *Toughened Composites.* ASTM STP 937, pp. 260–274, American Society for Testing and Materials, Philadelphia, PA. (5) Leach, D.C., Curtis, D.C., and Tamblin, D.R. 1987. In Johnson, N.J., ed., *Toughened Composites.* ASTM STP 937, pp. 358–380, American Society for Testing and Materials, Philadelphia, PA.

measurement of the critical strain energy release rate for mode II delamination is the end-notched flexure (ENF) test. An ENF specimen is shown in figure 9.17(b). The strain energy release rate analysis of the ENF specimen, which has been improved and used by several investigators [52–57], will be discussed in more detail in the review of test methods in chapter 10.

Once the capability to measure G_{Ic} and G_{IIc} separately had been developed, it became possible to evaluate various interactive criteria for mixed mode delamination growth. Although there is no universal agreement on which mixed mode delamination growth criterion is the most accurate, one of the simplest and most widely used of these criteria is given by the equation

$$\left(\frac{G_I}{G_{Ic}}\right)^m + \left(\frac{G_{II}}{G_{IIc}}\right)^n = 1 \tag{9.61}$$

where G_I, G_{II} = strain energy release rates for delamination growth in modes I and II, respectively.

G_{Ic}, G_{IIc} = critical strain energy release rates for delamination growth in modes I and II, respectively

m, n = empirically determined exponents.

Good agreement between the predictions from this equation and experimental data has been reported by O'Brien et al. [58] and Johnson and Mangalgiri [59] when $m = n = 1$. O'Brien et al. [58] investigated the use of equation (9.61) for graphite/epoxy laminates having various lay-ups, and predictions are compared with experimental data from the edge delamination test [43] in figure 9.18. Some previous data from Murri and

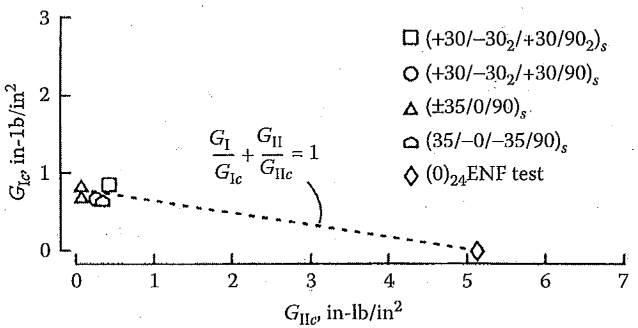

FIGURE 9.18
Comparison of predictions from equation (9.61) with mixed mode fracture data for T300/5208 graphite/epoxy laminates. (From O'Brien, T.K., Johnston, N.J., Raju, I.S., Morris, D.H., and Simonds, R.A. 1987. In Johnston, N.J. ed., *Toughened Composites*, ASTM STP 937, pp. 199–221. American Society for Testing and Materials, Philadelphia, PA. Copyright ASTM. Reprinted with permission.)

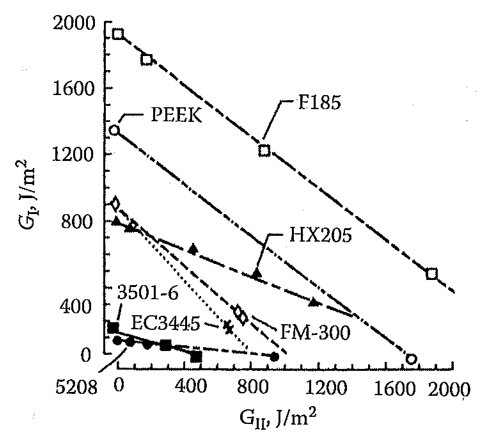

FIGURE 9.19
Comparison of predictions from equation (9.61) with mixed mode fracture data for several matrix resins. (From Johnson, W.S. and Mangalgiri, P.D. 1987. In Johnston, N.J. ed., *Toughened Composites*, ASTM STP 937, pp. 295–315. American Society for Testing and Materials, Philadelphia, PA. Copyright ASTM. Reprinted with permission.)

O'Brien [60] are included in figure 9.18. Johnson and Mangalgiri tested various matrix resins using the DCB, ENF, and several other methods, and comparisons of the predictions of equation (9.61) with experimental data are shown in figure 9.19. On the other hand, Ramkumar and Whitcomb [61] have concluded that equation (9.61) is not a reliable delamination growth criterion for graphite/epoxy.

The measurement of mixed mode interlaminar fracture toughness (in particular, mixed Mode I and Mode II) has been the subject of numerous publications, and many methods have been proposed. One method, known as the mixed mode-bending test, was originally developed by Reeder and Crews [62] and later evolved as an ASTM standard [63]. This method will be discussed in more detail in chapter 10.

In recent years much research has gone into the improvement of interlaminar fracture toughness of composites, and the results of some of this research can be seen in the G_{Ic} data of table 9.1. For example, since the interlaminar region consists primarily of matrix material, there has been considerable interest in the use of tough matrix materials. Significant improvements in the composite G_{Ic} have been obtained by using tough matrix materials such as polysulfone [46], elastomer-modified epoxy [48], and polyetheretherketone [49]. It is not clear, however, that additional increases in resin matrix toughness will necessarily be translated into correspondingly higher composite toughness [50,51]. Figure 9.20 from Hunston et al. [51] shows that for resin G_{Ic} values less than about 0.4 kJ/m^2

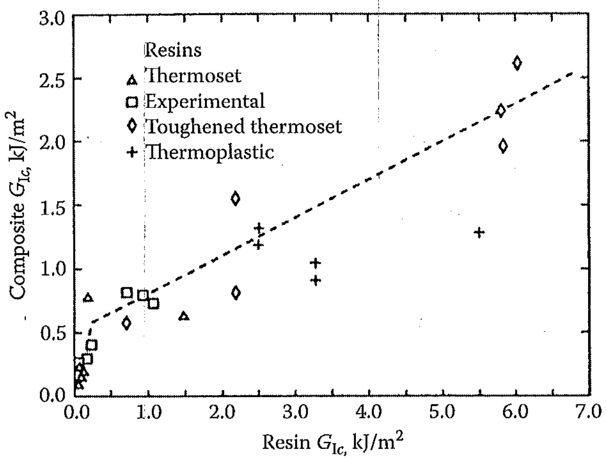

FIGURE 9.20
Mode I interlaminar strain energy release rates for steady crack growth in graphite fiber composites as a function of the neat resin strain energy release rates for several matrix resins. (From Hunston, D.L., Moulton, R.J., Johnston, N.J., and Bascom, W. 1987. In Johnston, N.J. ed., *Toughened Composites*, ASTM STP 937, pp. 74–94. American Society for Testing and Materials, Philadelphia, PA. Copyright ASTM. Reprinted with permission.)

substantial gains in the corresponding graphite fiber composite, G_{Ic} are obtained by increasing the resin G_{Ic}. For resin G_{Ic} values greater than about 0.4 kJ/m^2, however, the gains in the composite G_{Ic} from additional increases in resin G_{Ic} are not nearly as great. Scanning electron microscope studies of delamination fracture surfaces have shown that increased toughness of the matrix causes an increase in the delamination fracture toughness by increasing the size of the plastic zone ahead of the crack tip [50,51]. Further increases in the size of this plastic zone are apparently prevented by the constraint of the fibers in the adjacent plies, however [50,51].

A variety of other methods for increasing interlaminar fracture toughness of laminates have been investigated. For example, thin films or "interleaves" made of a tough polymer resin can be embedded between the fiber-reinforced resin laminae [64–68]. Coating the fibers with a thin, tough polymer film [69–70], hybridization of different fiber types [71–72], and stitching of adjacent laminae [73] have also been investigated. A critical review of methods for improving fracture toughness of composites through interface control has also been published [74]. The so-called Z-pinning approach for improving delamination resistance involves the insertion of metal or composite pins through the thickness (i.e, in the z direction) of the laminate in the same way that a nail would be driven into wooden boards to hold them together [75–77]. Three-dimensional

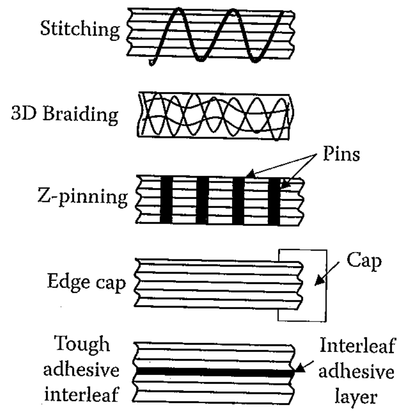

FIGURE 9.21
Illustration of some mechanical means of improving interlaminar fracture toughness.

braiding essentially eliminates delamination as a failure mode, since there are no distinct plies to separate [78,79]. However, the in-plane strength and stiffness of the braided composite will not be as great as the corresponding properties of a laminate constructed of unidirectional plies. These and other mechanical means of improving delamination resistance are illustrated schematically in figure 9.21. Of particular relevance here is a special issue of a well-known composites journal that has been devoted to papers on advances in statics and dynamics of delamination [80]. Unfortunately, improvements in interlaminar toughness often come at the expense of degradation in other properties such as hot/wet strength and stiffness or viscoelastic creep response. Although significant progress has been made in understanding delamination, much is still to be learned. The study of delamination continues to be a very active research topic, and the reader is encouraged to consult recent journal publications and conference proceedings for the latest findings.

9.5 Problems

1. The thin-walled tubular shaft shown in figure 9.22 is made of randomly oriented, short-fiber-reinforced metal matrix composite. The shaft has a longitudinal through-thickness crack of length $2a$ and is subjected to a torque $T = 1$ KN-m. If the mode II fracture toughness of the composite is $K_{IIc} = 40$ MPa-m$^{1/2}$, determine the critical crack size for self-sustaining crack growth.

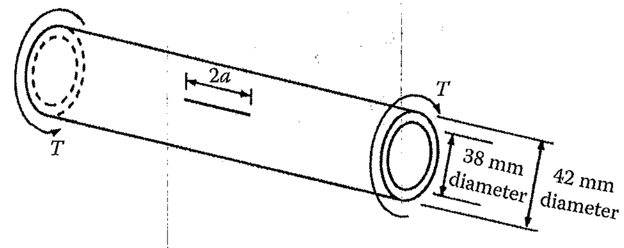

FIGURE 9.22
Thin-walled tubular composite shaft with longitudinal crack.

2. (a) Determine the allowable torque, T, if the crack length for the shaft in figure 9.22 is $2a = 10$ mm. Use the same dimensions and fracture toughness values that were given in problem 1.
   (b) If the uniaxial yield stress for the shaft material is $Y = 1200$ MPa, and the crack is ignored, compare the answer from part (a) with the allowable torque based on the Maximum Shear Stress criterion for yielding.
3. The tube shown in figure 9.22 is subjected to an internal pressure, $p = 5$ MPa, instead of a torque. Neglecting the stress along the longitudinal axis of the tube, and assuming that the mode I fracture toughness is $K_{Ic} = 10$ MPa-m$^{1/2}$, determine the critical crack size.
4. As in problem 3, assume that the tube in figure 9.22 is subjected only to an internal pressure and neglect the longitudinal stress.
   (a) Determine the allowable internal pressure, p, if the crack length in figure 9.22 is $2a = 10$ mm. Use the same dimensions and fracture toughness values that were given in problem 3.
   (b) Using the yield stress from problem 2 and ignoring the crack, compare the answer from part (a) of this problem with the allowable internal pressure based on the Maximum Shear Stress criterion for yielding.
5. Use the Whitney–Nuismer average stress criterion to estimate the allowable internal pressure for problem 4 if the unnotched tensile strength of the material is $\sigma_0 = 1500$ MPa and the parameter $a_0 = 3$ mm.
6. Repeat problem 5 using the Whitney–Nuismer point stress criterion and the parameter $d_0 = 1$ mm.
7. The 920-mm diameter, 1.6-mm-thick spherical pressure vessel in figure 9.23 is a filament wound quasi-isotropic composite laminate with a single 50-mm diameter entrance hole. The vessel

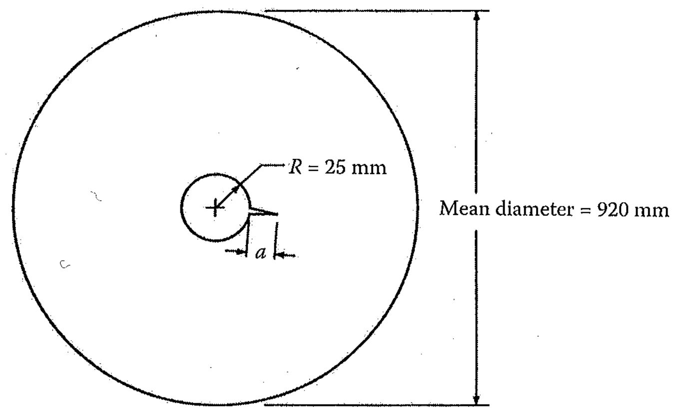

FIGURE 9.23
Spherical composite pressure vessel with single crack at the edge of entrance hole.

material has a mode I fracture toughness of $K_{Ic} = 25$ MPa-m$^{1/2}$. If the vessel is to contain gas at a pressure of 0.69 MPa, what is the critical length, a_c, of a single crack emanating from the edge of the hole? The Bowie equation (eq. [9.38]) may be used for this problem, and the function $f(a/R)$ for a biaxial stress field and a single crack of length, a, at the edge of a hole of radius, R, is tabulated below for several values of a/R.

a/R	f(a/R)	a/R	f(a/R)
0.1	1.98	0.8	1.32
0.2	1.82	1.0	1.22
0.3	1.67	1.5	1.06
0.4	1.58	2.0	1.01
0.5	1.49	3.0	0.93
0.6	1.42	5.0	0.81

8. If the quasi-isotropic graphite/epoxy laminate in example 7.5 has a centrally located 25-mm-diameter hole, determine the ratio of notched to unnotched uniaxial strength for the laminate using the Whitney–Nuismer average stress criterion. The parameter $a_0 = 4$ mm.
9. A 3-mm thick composite specimen is tested as shown in figure 9.4(a), and the compliance, $s = u/P$, as a function of the half-crack length, a, is shown in figure 9.24. In a separate test the critical load for self-sustaining crack propagation, P_c, is measured for different crack lengths, and the critical load corresponding to

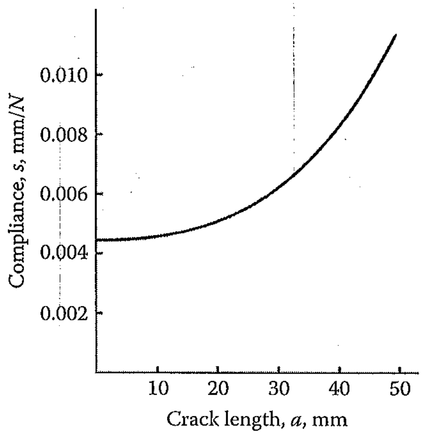

FIGURE 9.24
Variation of specimen compliance with crack length for problem 9.

a crack length 2a = 50 mm is found to be 100 N. Determine the critical mode I strain energy release rate, G_{Ic}.

10. A laminated plate consisting of the $[90/0/90]_s$ AS/3501 laminate described in example 7.10 has a central hole as shown in figure 9.25. The plate is loaded uniaxially along the 0° direction as shown. Using the Whitney–Nuismer average stress criterion for stress fracture with an unnotched laminate tensile strength of $\sigma_0 = 500$ MPa, and an averaging distance $a_0 = 10$ mm, plot the notched tensile strength σ_N^∞ as a function of hole radius R. What are the maximum and minimum theoretical values of the notched tensile strength, and under what conditions do they occur?

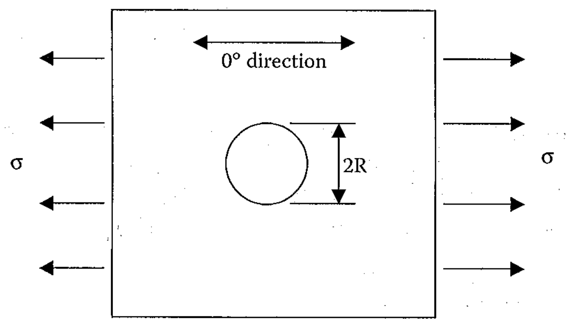

FIGURE 9.25
Uniaxially loaded laminated plate with central hole for problem 10.

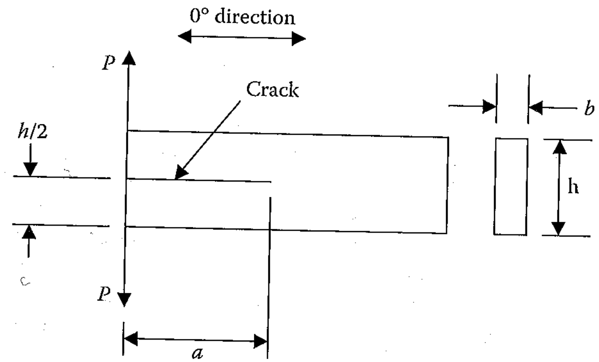

FIGURE 9.26
Cracked laminate subjected to bending for problem 11.

11. A unidirectional [0] composite beam of longitudinal modulus E_1, thickness b, and depth h has a crack of length a and is loaded by the equal and opposite forces P as shown in figure 9.26. Determine G_I, the Mode I strain energy release rate for this crack. Your answer should be expressed in terms of the given parameters.

References

1. Chan, W.F. 1997. Fracture and damage mechanics in laminated composites, in Mallick, P.K. ed., *Composites Engineering Handbook*, chap. 7. Marcel Dekker, Inc., New York.
2. Sendeckyj, G.P. ed. 1975. *Fracture Mechanics of Composites*, ASTM STP 593. American Society for Testing and Materials, Philadelphia, PA.
3. Reifsnider, K.L. ed., 1982. *Damage in Composite Materials*, ASTM STP 775. American Society for Testing and Materials, Philadelphia, PA.
4. Johnson, W.S. ed., 1985. *Delamination and Debonding of Materials*, ASTM STP 876. American Society for Testing and Materials, Philadelphia, PA.
5. Hahn, H.T. ed. 1986. *Composite Materials: Fatigue and Fracture*, ASTM STP 907. American Society for Testing and Materials, Philadelphia, PA.
6. Lagace, P.A. ed., 1989. *Composite Materials: Fatigue and Fracture*, ASTM STP 1012. American Society for Testing and Materials, Philadelphia, PA.
7. O'Brien, T.K. ed., 1991. *Composite Materials: Fatigue and Fracture*, ASTM STP 1110. American Society for Testing and Materials, Philadelphia, PA.
8. Friedrich, K. ed. 1989. Application of fracture mechanics to composite materials, in Pipes, R.B. ed. *Composite Material Series*, vol. 6 (Series ed.). Elsevier Science Publisher, Amsterdam, The Netherlands.

9. Newaz, G.M. ed 1991. *Delamination in Advanced Composites*. Technomic Publishing Co., Lancaster, PA.
10. Griffith, A.A. 1920. The phenomena of rupture and flow in solids. *Philosophical Transactions of the Royal Society*, 221A, 163–198.
11. Gilman, J.J. 1968. *Transactions of the American Society for Metals*, 61, 861–906 [Reprint of "Griffith, A.A. 1920. The phenomena of rupture and flow in solids. *Philosophical Transactions of the Royal Society*, 221A, 163–198." with corrections and commentary].
12. Sih, G.C. and Liebowitz, H. 1968. Mathematical theories of brittle fracture, in Liebowitz, H. ed., *Fracture — An Advanced Treatise*, vol. II, *Mathematical Fundamentals*, pp. 67–190. Academic Press, New York.
13. Irwin, G.R. 1949. *Fracturing of Metals*, pp. 147–166. American Society of Metals, Cleveland, OH.
14. Orowan, E. 1950. *Fatigue and Fracture of Metals*. MIT Press, Cambridge, MA.
15. Westergaard, H.M. 1939. Bearing pressures and cracks. *Transactions of the ASME, Series E, Journal of Applied Mechanics*, 61, A49–A53.
16. Irwin, G.R. 1957. Analysis of stresses and strains near the end of a crack traversing a plate. *Transactions of the ASME, Journal of Applied Mechanics*, 24, 361–364.
17. Tada, H., Paris, P.C., and Irwin, G.R. 1973. *The Stress Analysis of Cracks Handbook*. Del Research Corporation, Hellertown, PA.
18. Lekhnitskii, S.G. 1963. *Theory of Elasticity of an Anisotropic Elastic Body*. Holden-Day, Inc., San Francisco, CA.
19. Wu, E.M. 1968. Fracture mechanics of anisotropic plates, in Tsai, S.W., Halpin, J.C., and Pagano N.J. eds., *Composite Materials Workshop*, pp. 20–43. Technomic Publishing Co., Lancaster, PA.
20. Konish, H.J., Swedlow, J.L., and Cruse, T.A. 1972. Experimental investigation of fracture in an advanced composite. *Journal of Composite Materials*, 6, 114–124.
21. Parhizgar, S., Zachary, L.W., and Sun, C.T. 1982. Application of the principles of linear fracture mechanics to the composite materials. *International Journal of Fracture*, 20, 3–15.
22. Alexander, R.M., Schapery, R.A., Jerina, K.L., and Sanders, B.A. 1982. Fracture characterization of a random fiber composite material, in Sanders B.A. ed., *Short Fiber Reinforced Composite Materials*, ASTM STP 772, pp. 208–224. American Society for Testing and Materials, Philadelphia, PA.
23. Sun, C.T. and Sierakowski, R.L. 1980. Fracture characterization of composites with chopped fiberglass reinforcement. *SAMPE Quarterly*, 11(4), 15–21.
24. Gaggar, S.K. and Broutman, L.J. 1974. The development of a damage zone at the tip of a crack in a glass fiber reinforced polyester resin. *International Journal of Fracture*, 10, 606–608.
25. Irwin, G.R. 1958. Fracture, in Flugge, S. ed., *Handbuch der Physik*, vol. 6, pp. 551–590. Springer, Berlin.
26. Corten, H.T. 1972. Fracture mechanics of composites, in Liebowitz, H. ed., *Fracture — An Advanced Treatise*, vol. VII, *Fracture of Nonmetals and Composites*, pp. 675–769. Academic Press, New York.
27. Cruse, T.A. 1973. Tensile strength of notched composites. *Journal of Composite Materials*, 7, 218–229.

28. Paris, P.C. and Erdogan, F. 1963. A critical analysis of crack propagation laws. *Transactions of ASME, Journal of Basic Engineering*, 85, 528–534.
29. Kunz, S.C. and Beaumont, P.W.R. 1975. Microcrack growth in graphite fiber-epoxy resin systems during compressive fatigue, in Hancock J.R. ed., *Fatigue of Composite Materials*, ASTM STP 569, pp. 71–91. American Society for Testing and Materials, Philadelphia, PA.
30. Spearing, M., Beaumont, P.W.R., and Ashby, M.F. 1991. Fatigue damage mechanics of notched graphite-epoxy laminates, in O'Brien, T.K. ed., *Composite Materials: Fatigue and Fracture*, vol. 3, ASTM STP 1110, pp. 617–637. American Society for Testing and Materials, Philadelphia, PA.
31. Rybicki, E.F. and Kanninen, M.F. 1997. A finite element calculation of stress intensity factors by a modified crack closure integral. *Engineering Fracture Mechanics*, 9, 931–938.
32. Krueger, R. 2004. Virtual crack closure technique: history, approach and applications. *Applied Mechanics Reviews*, 57(2), 109–143.
33. Whitney, J.M. and Nuismer, R.J. 1974. Stress fracture criteria for laminated composites containing stress concentrations. *Journal of Composite Materials*, 8, 253–265.
34. Nuismer, R.J. and Whitney, J.M. 1975. Uniaxial failure of composite laminates containing stress concentrations, in *Fracture Mechanics of Composites*, ASTM STP 593, pp. 117–142. American Society for Testing and Materials, Philadelphia, PA.
35. Waddoups, M.E., Eisenmann, J.R., and Kaminski, B.E., 1971. Macroscopic fracture mechanics of advanced composite materials. *Journal of Composite Materials*, 5(4), 446–454.
36. Bowie, O.L., 1956. An analysis of an infinite plate containing radial cracks originating from the boundary of an internal circular hole. *Journal of Mathematics and Physics*, 35, 60–71.
37. Timoshenko, S.P. and Goodier, J.N. 1951. *Theory of Elasticity*, 2nd ed. McGraw-Hill, Inc., New York.
38. Lekhnitskii, S.G. 1968. *Anisotropic Plates* (Translated from 2d Russian ed. by Tsai, S.W. and Cheron, T.). Gordon and Breath Science Publishers, New York.
39. Roderick, G.L., Everett, R.A., and Crews, J.H. 1975. Debond propagation in composite-reinforced metals, in *Fatigue of Composite Materials*, ASTM STP 569, pp. 295–306. American Society for Testing and Materials, Philadelphia, PA.
40. Kanninen, M.F., Rybicki, E.F., and Brinson, H.F. 1977. A critical look at current applications of fracture mechanics to the failure of fiber reinforced composites. *Composites*, 8, 17–22.
41. Rybicki, E.F., Schmueser, D.W., and Fox, J. 1977. An energy release rate approach for stable crack growth in the free-edge delamination problem. *Journal of Composite Materials*, 11, 470–487.
42. Wang, S.S. 1979. Delamination crack growth in unidirectional fiber-reinforced composite under static and cyclic loading, in Tsai, S.W. ed., *Composite Materials: Testing and Design*, ASTM STP, pp. 674, 642–663. American Society for Testing and Materials, Philadelphia, PA.
43. O'Brien, T.K. 1982. Characterization of delamination onset and growth in a composite laminate, in Reifsnider, K.L. ed., *Damage in Composite Materials*

ASTM STP 775, pp. 140–167. American Society for Testing and Materials, Philadelphia, PA.
44. Devitt, D.F., Schapery, R.A., and Bradley, W.L. 1980. A method for determining the mode I delamination fracture toughness of elastic and viscoelastic composite materials. *Journal of Composite Materials*, 14, 270–285.
45. Wilkins, D.J., Eisenmann, J.R., Camin, R.A., Margolis, W.S., and Benson, R.A. 1982. Characterizing delamination growth in graphite-epoxy, in Reifsnider, K.L. ed., *Damage in Composite Materials*, ASTM STP 775, pp. 168–183. American Society for Testing and Materials, Philadelphia, PA.
46. Whitney, J.M., Browning, C.E., and Hoogsteden, W. 1982. A double cantilever beam test for characterizing mode I delamination of composite materials. *Journal of Reinforced Plastics and Composites*, 1, 297–313.
47. Aliyu, A.A. and Daniel, I.M. 1985. Effects of strain rate on delamination fracture toughness of graphite/epoxy, in Johnson, W.S., ed., *Delamination and Debonding of Materials*, ASTM STP 876, pp. 336–348. American Society for Testing and Materials, Philadelphia, PA.
48. Daniel, I.M., Shareef, I., and Aliyu, A.A. 1987. Rate effects on delamination of a toughened graphite/epoxy, in Johnston, N.J. ed., *Toughened Composites*, ASTM STP 937, pp. 260–274. American Society for Testing and Materials, Philadelphia, PA.
49. Leach, D.C., Curtis, D.C., and Tamblin, D.R. 1987. Delamination behavior of carbon fiber/poly(etheretherketone) (PEEK) composites, in Johnson, N.J. ed., *Toughened Composites*, ASTM STP 937, pp. 358–380. American Society for Testing and Materials, Philadelphia, PA.
50. Bradley, W.L. 1989. Relationship of matrix toughness to interlaminar fracture toughness, in Friedrich, K. ed., *Application of Fracture Mechanics of Composite Materials*, chap. 5, vol. 6, *Composite Material Series*, Pipes, R.B. (Series ed.). Elsevier Science Publishers, Amsterdam, The Netherlands.
51. Hunston, D.L., Moulton, R.J., Johnston, N.J., and Bascom, W. 1987. Matrix resin effects in composite delamination: mode I fracture aspects, in Johnston, N.J. ed., *Toughened Composites*, ASTM STP 937, pp. 74–94. American Society for Testing and Materials, Philadelphia, PA.
52. Carlsson, L.A. and Gillispie, J.W. 1989. Mode II interlaminar fracture of composites, in Friedrich, K. ed., *Application of Fracture Mechanics to Composite Materials*, chap. 4, vol. 6, *Composite Material Series*, Pipes, R.B. (Series ed.). Elsevier Science Publishers, Amsterdam, The Netherlands.
53. Russell, A.J. and Street, K.N. 1985. Moisture and temperature effects on the mixed mode delamination fracture of unidirectional graphite/epoxy, in Johnson, W.S. ed., *Delamination and Debonding of Materials*, ASTM STP pp. 876, 349–370. American Society for Testing and Materials, Philadelphia, PA.
54. Carlsson, L.A., Gillispie, J.W., Jr., and Pipes, R.B. 1986. On the analysis and design of the end notched flexure (ENF) specimen for mode II testing. *Journal of Composite Materials*, 20, 594–604.
55. Carlsson, L.A. and Pipes, R.B. 1987. *Experimental Characterization of Advanced Composite Materials*. Prentice-Hall, Inc., Englewood Cliffs, NJ.
56. Kageyama, K., Kikuchi, M., and Yanagisawa, N. 1991. Stabilized end notched flexure test: characterization of mode II interlaminar crack growth, in O'Brien, T.K. ed., *Composite Materials: Fatigue and Fracture*, vol. 3, ASTM

STP 1110, pp. 210–225. American Society for Testing and Materials, Philadelphia, PA.
57. Russell, A.J. 1991. Initiation and growth of Mode II delamination in toughened composites, in O'Brien, T.K. ed., *Composite Materials: Fatigue and Fracture*, vol. 3, ASTM STP 1110, pp. 226–242. American Society for Testing and Materials, Philadelphia, PA.
58. O'Brien, T.K., Johnston, N.J., Raju, I.S., Morris, D.H., and Simonds, R.A. 1987. Comparisons of various configurations of the edge delamination test for interlaminar fracture toughness, in Johnston, N.J. ed., *Toughened Composites*, ASTM STP 937, pp. 199–221. American Society for Testing and Materials, Philadelphia, PA.
59. Johnson, W.S. and Mangalgiri, P.D. 1987. Influence of the resin on interlaminar mixed-mode fracture, in Johnston, N.J. ed., *Toughened Composites*, ASTM STP 937, pp. 295–315. American Society for Testing and Materials, Philadelphia, PA.
60. Murri, G.B. and O'Brien, T.K. 1985. Interlaminar G_{IIc} evaluation of toughened resin matrix composites using the end notched flexure test, in *Proceedings of the 26th AIAA/ASME/ASCE/AHS Structures, Structural Dynamics and Materials Conference*, pp. 197–202. American Institute for Aeronautics and Astronautics, New York.
61. Ramkumar, R.L. and Whitcomb, J.D. 1985. Characterization of mode I and mixed mode delamination growth in T300/5208 graphite/epoxy, in Johnson, W.S. ed., *Delamination and Debonding of Materials*, ASTM STP 876, pp. 315–335. American Society for Testing and Materials, Philadelphia, PA.
62. Reeder, J.R. and Crews, J.H. Jr. 1990. Mixed mode bending method for delamination testing. *AIAA Journal*, 28(7), 1270–1276.
63. D 6671/D 6771-M-04. 2005. Standard test method for mixed Mode I – Mode II interlaminar fracture toughness of unidirectional fiber reinforced polymer matrix composites, *Space Simulation; Aerospace and Aircraft; Composite Materials*, vol. 15.03. ASTM International, West Conshohocken, PA.
64. Chan, W.S., Rogers, C., and Aker, S. 1986. Improvement of edge delamination strength of composite laminates using adhesive layers, in Whitney, J.M. ed., *Composite Materials: Testing and Design (Seventh Conference)*, ASTM STP 893, pp. 266–285. American Society for Testing and Materials, Philadelphia, PA.
65. Evans, R.E. and Masters, J.E. 1987. A new generation of epoxy composites for primary structural applications: materials and mechanics, in Johnston, N.J. ed., *Toughened Composites*, ASTM STP 937, pp. 413–436. American Society for Testing Materials, Philadelphia, PA.
66. Ishai, O., Rosenthal, H., Sela, N., and Drukker, E. 1988. Effect of selective adhesive interleaving on interlaminar fracture toughness of graphite/epoxy composite laminates. *Composites*, 19(1), 49–54.
67. Sela, N., Ishai, O., and Banks-Sills, L. 1989. The effect of adhesive thickness on interlaminar fracture toughness of interleaved CFRP specimens. *Composites*, 20(3), 257–264.
68. Lagace, P.A. and Bhat, N.V. 1992. Efficient use of film adhesive interlayers to suppress delamination, in Grimes, G.C. ed., *Composite Materials: Testing and Design*, vol. 10, ASTM STP 1120, pp. 384–396. American Society for Testing and Materials, Philadelphia, PA.

69. Broutman, L.J. and Agarwal, B.D. 1974. A theoretical study of the effect of an interfacial layer on the properties of composites. *Polymer Engineering and Science*, 14(8), 581–588.
70. Schwartz, H.S. and Hartness, T. 1987. Effect of fiber coatings on interlaminar fracture toughness of composites, in Johnston, N.J. ed., *Toughened Composites*, ASTM STP 937, pp. 150–178. American Society for Testing and Materials, Philadelphia, PA.
71. Browning, C.E. and Schwartz, H.S. 1986. Delamination resistant composite concepts, in Whitney, J.M. ed., *Composite Materials: Testing and Design (Seventh Conference)*, ASTM STP 893, pp. 256–265. American Society for Testing and Materials, Philadelphia, PA.
72. Mignery, L.A., Tan, T.M., and Sun, C.T. 1985. The use of stitching to suppress delamination in laminated composites, in Johnson, W.S. ed., *Delamination and Debonding of Materials*, ASTM STP 876, pp. 371–385. American Society for Testing and Materials, Philadelphia, PA.
73. Garcia, R., Evans, R.E., and Palmer, R.J. 1987. Structural property improvements through hybridized composites, in Johnston, N.J. ed., *Toughened Composites*, ASTM STP 937, pp. 397–412. American Society for Testing and Materials, Philadelphia PA.
74. Kim, J.K. and Mai, Y.W. 1991. High stretch, high fracture toughness fibre composites with interface control — a review. *Composites Science and Technology*, 41, 333–378.
75. Yan, W., Liu, H.-Y., and Mai, Y.-W. 2003. Numerical study on the Mode I delamination toughness of z-pinned laminates. *Composites Science and Technology*, 63(10), 1481–1493.
76. Byrd, L.W. and Birman, V. 2006. Effectiveness of z-pins in preventing delamination of co-cured composite joints on the example of a double cantilever test. *Composites Part B Engineering*, 37(4–5), 365–378.
77. Cartie, D.D.R., Troulis, M., and Partridge, I.K. 2006. Delamination of z-pinned carbon fibre reinforced laminates. *Composites Science and Technology*, 66(6), 855–861.
78. Mouritz, A.P., Baini, C., and Herszberg, I. 1999. Mode I interlaminar fracture toughness properties of advanced textile fiberglass composites. *Composites Part A Applied Science and Manufacturing*, 30A(7), 859–870.
79. Yau, S.-S., Chou, T.-W., and Ko, F.K. 1986. Flexural and axial compressive failures of three-dimensionally braided composite I-beams. *Composites*, 17(3), 227–232.
80. Allix, O. and Johnson, A. eds. 2006. Advances in statics and dynamics of delamination. *Composites Science and Technology* (special issue), 66(6), 695–862.

10

Mechanical Testing of Composites and Their Constituents

10.1 Introduction

The purpose of this chapter is to review briefly the most widely used methods for mechanical testing of composite materials and their constituents. In previous chapters, the emphasis has been on the development of analytical models for mechanical behavior of composite materials. The usefulness of such models depends heavily on the availability of measured intrinsic mechanical property data to use as input. In addition, some aspects of mechanical behavior of composites are so complex that the feasibility of proper analytical modeling is questionable, and the experimental approach may be the only acceptable solution. Much of our knowledge about the special nature of composite behavior has been derived from experimental observations. The measurement of mechanical properties is also an important element of the quality control and quality assurance processes associated with the manufacture of composite materials and structures.

Due to the special characteristics of composites, such as anisotropy, coupling effects, and the variety of possible failure modes, it has been found that the mechanical test methods that are used for conventional metallic materials are usually not applicable to composites. Thus, the development and evaluation of new test methods for composites have been, and continues to be, a major challenge for the experimental mechanics community. The technology associated with composite test methods and test equipment has become just as sophisticated as that associated with the corresponding analytical methods. Many of these test methods have evolved into standards that have been adopted by ASTM International, formerly the American Society for Testing and Materials. The ASTM standards for testing of polymer matrix and metal matrix composites and their constituents are compiled mainly in ASTM Volume 15.03 [1], while the standards for testing ceramic matrix composites are compiled mainly in ASTM Volume 15.01 [2]. The emphasis in this chapter will